2022

Radiative Conductivity Estimation Using Direct Approach For Fibrous Materials

Mohammad Khaleel

University of Kentucky, mokhaleel@outlook.com
Author ORCID Identifier:
 https://orcid.org/0000-0003-0375-7298
Digital Object Identifier: https://doi.org/10.13023/etd.2022.187

Right click to open a feedback form in a new tab to let us know how this document benefits you.

STUDENT AGREEMENT:

I represent that my thesis or dissertation and abstract are my original work. Proper attribution has been given to all outside sources. I understand that I am solely responsible for obtaining any needed copyright permissions. I have obtained needed written permission statement(s) from the owner(s) of each third-party copyrighted matter to be included in my work, allowing electronic distribution (if such use is not permitted by the fair use doctrine) which will be submitted to UKnowledge as Additional File.

I hereby grant to The University of Kentucky and its agents the irrevocable, non-exclusive, and royalty-free license to archive and make accessible my work in whole or in part in all forms of media, now or hereafter known. I agree that the document mentioned above may be made available immediately for worldwide access unless an embargo applies.

I retain all other ownership rights to the copyright of my work. I also retain the right to use in future works (such as articles or books) all or part of my work. I understand that I am free to register the copyright to my work.

REVIEW, APPROVAL AND ACCEPTANCE

The document mentioned above has been reviewed and accepted by the student's advisor, on behalf of the advisory committee, and by the Director of Graduate Studies (DGS), on behalf of the program; we verify that this is the final, approved version of the student's thesis including all changes required by the advisory committee. The undersigned agree to abide by the statements above.

Mohammad Khaleel, Student

Dr. Alexandre Martin, Major Professor

Dr. Jesse Hoagg, Director of Graduate Studies

Radiative Conductivity Estimation Using Direct Approach For Fibrous
Materials

_____

THESIS

_____

A thesis submitted in partial fulfillment of the
requirements for the degree of Master of Science
in Mechanical Engineering in the College of Engineering
at the University of Kentucky

By

Mohammad Rabeh Khaleel

Lexington, Kentucky

Director: Dr. Alexandre Martin, Professor of Mechanical Engineering

Lexington, Kentucky

2022

ABSTRACT OF THESIS

Radiative Conductivity Estimation Using Direct Approach For Fibrous Materials

During planetary entry, space vehicles encounter high loads of thermal energy which requires a thermal protection system. Ablative thermal protection systems are usually made out of fibrous materials that exhibit internal radiation. In order to model the internal radiation response of a thermal protection system one should obtain proper radiative properties as well as thermal properties. The objective of this work is to provide a method that solves for the solid/gas thermal conductivity. Which can be used in coupled detailed radiative analysis.

Keywords: radiative conductivity, fibrous materials, radiative transfer, thermal protection system, P1 approximation, Finite Volume method.

Mohammad Khaleel

04/18/2022

Radiative Conductivity Estimation Using Direct Approach For Fibrous Materials

By
Mohammad Khaleel

Dr. Alexandre Martin
Director of Thesis

Dr. Jesse Hoagg
Director of Graduate Studies

04/18/2022
Date

Dedicated to Dad, Mom, Grandfather, and My Brother.

ACKNOWLEDGMENTS

TABLE OF CONTENTS

LIST OF TABLES

LIST OF FIGURES

Chapter 1

1.1 Introduction

Space vehicles approaching a planetary body travel at extremely high velocities, which creates a challenge for the entering phase of the mission. Some of the challenges constraining the design of such vehicles include deceleration, heating, and accuracy of landing.

Heating is one of the main challenges that a space vehicle encounter during planetary entry. According to NASA [3] a shuttle with an approximate mass of 100,000 kg moves at an estimated speed of 7900 m/s. The kinetic energy of the shuttle is therefore in the vicinity of 312 MJ, equivalent to the electric energy consumption of nearly 300 thousand households in one day. For the space shuttle to come to a complete halt, its kinetic energy must become zero. Since energy is conserved a large portion of it is transferred into thermal energy.

Even though most of the energy is converted away some of it reaches the structure of the vehicle, therefore a thermal protection system is needed.

There are multiple types of thermal protection systems such as passive, active, and semi-passive thermal protection systems.

Figure 1.1: Artistic visualization of Orion spacecraft re-entry from Ref. [60]

Passive thermal protection systems are ones that do not involve any moving components, and whose temperature is controlled using their own material properties. Passive thermal protection systems include heat sinks made of metal structures with a high heat capacitance [4, 5], hot structures reradiating heat once the surface temperature exceeds a certain value [4, 6], and insulated structures made of an outer layer reradiating most of the incident energy, as well as a lower insulating material slowing down heat transfer towards the surface [7].

Active thermal protection systems implies a working mechanisms that mitigate heat. For instance, convective cooling can be used by pumping a coolant fluid underneath the thermal protection surface [8]. Film cooling can also be used for hypersonic vehicles, by injecting the coolant at specific locations across the vehicle's surface [9-13]. Finally,

transpiration cooling can be used for extremely high temperatures, by passing a coolant through the porous structure to cool it down.

Semi-passive protection methods include heat pipes, to manage heat through phase change processes, in addition to ablative thermal protection systems [4]. The latter will be discussed in the following paragraphs.

Ablative thermal protection systems are a non-reusable type of thermal protection systems. During reentry, the system sacrifices its material through phase change, oxidation, spallation, and erosion processes. By sacrificing its material, the system prevents energy from reaching the surface since it is ejected along with the removed mass.

Ablative materials can be generally subdivided into two main categories: charring and non-charring ablators. Charring ablators, also known as decomposing ablators, undergo surface reactions, as well as in depth decomposition. Non-charring ablators do not decompose internally, and only change phase at the exposed surface. Carbon-carbon, silica, and Teflon are all examples of non-charring ablators [4].

The decomposing ablator consists of a phenolic resin, combined with a binder material such as carbon or silica. When the ablator's internal temperature reaches a certain value, the resin pyrolyze and creates a porous charred layer [14].

1.2 Motivation

Hypersonic entry is associated with elevated temperatures, creating a chemically

reacting flow, which can be composed of molecules, atoms, free electrons, and ions.

Each one of the previously mentioned components could contribute to the absorption

and emission of an electromagnetic wave, causing variation within the incident heat

flux.

For velocities higher than 10 km/s, radiation becomes important and can be larger

than convective heating, especially in the wake region of the capsule [16]. This was

previously neglected, as Fire II and Apollo measured negligible values [17]. When

radiation was considered, one of the following assumptions was made: a Boltzmann

distribution of electronic state [18-20], or negligence of vacuum ultraviolet radiation

[21]. In contradiction with the latter assumption, [16] showed that the contribution of

vacuum ultraviolet radiation could be seven times the non-vacuum ultraviolet radiation.

Hassan et al [22] showed that the tangent slab method, a commonly used method for

solving the radiative transfer equation, does not always predict the accurate radiation

results. This was particularly true in the flow field's wake region. They also showed that

better results can be obtained at the same flow region, by using a method based on the

spherical harmonics method. This will be further discussed in upcoming sections of this

paper.

It is clear from the previously mentioned, that for radiation to be examined, multiple

factors should be accounted for. On one hand, the variation of radiation intensity, as

well as changing radiative transfer properties with wavelength, should be considered. On the other hand, an adequate method should be used to accurately predict the radiative heat flux. Predicting accurate heat flux levels experienced by a vehicles shield, will enable optimizing the vehicle's size, preventing oversizing. This is return will eventually increase the payload capabilities of the vehicle.

1.3 Background

Heat transfer is the transfer of energy due to the presence of temperature gradients which happens either by conduction or radiation. In solids, conduction occurs through atomic lattice vibrational waves. In gases and liquids however, conduction occurs due to intermolecular collisions. Molecules at higher temperatures possess a higher energy content. When these molecules collide with lower energy molecules, energy is transferred. Conduction is predominant in solids and in stationary fluids not exhibiting any bulk fluid movement. Conduction transfers energy within the medium in a diffusive manner.

The transfer of energy via electromagnetic waves is known as radiation. Unlike conduction, radiation does not require a medium to transfer energy, as it can travel through vacuum. In addition, radiation does not require a continuous temperature gradient between the source and the recipient. A source at a hot temperature can transfer radiation to a recipient, without heating the medium in-between. For example, solar radiation is transferred from the hot sun to Earth through the cold space.

All materials at a temperature above absolute zero emit and absorb radiation by adjusting their molecular energy content. The strength and wavelength of emission depends mainly on the temperature of the source. Temperature affects radiation to a great extent, as radiation is proportional to fourth power of temperature gradient unlike conduction which is linearly proportional to the temperature gradient. Radiation's dependance on temperature gives it dominance over other modes of heat transfer, particularly in applications involving very elevated temperatures.

Radiation is not only fundamentally different in the way heat is transferred, but also in the way it is analyzed. Conduction occur between molecules close to each other. The short distance between molecules enables an energy balance on an infinitesimal volume, where the volume is small enough compared to the medium, but large enough when compared to the mean free path. The same approach cannot be used with radiation, as the mean free path of photons can either be very small, such as in metal absorption, or very large as is the case with solar radiation. Hence, energy conservation cannot be computed within an infinitesimal volume, but rather needs to be applied over the entire volume.

Applying energy conservation over the entire volume leads to an integral equation with six different variables: three variables in the spatial directions, two variables in the angular directions, and the wavelength as the sixth variable. Solving such an equation is not a simple task, and may not be possible in some cases, unless further simplifications are assumed. Moreover, obtaining radiation dependent properties is a major problem complicating matters even further.

Before proceeding with the radiative heat transfer equation, an overview of the

nature of radiation, as well as some useful definitions will be provided in the following

section.

1.3.1 Nature of radiation

Thermal radiation can either be considered as an emission of electromagnetic waves,

or as an emission of photons. Waves propagate at the speed of light, but the speed of

light depends on the medium in which it propagates through. The speed of light in any

medium can be calculated relative to the speed of light in vacuum as follows:

$$C = \frac{C_o}{n} \qquad (1.1)$$

where $C_o = 2.998 \times 10^8$ m/s and n is the refractive index of the medium.

Electromagnetic waves contain different amounts of energy depending on their

wavelength. Energy and frequency are related through the following equation, where

the Planck constant, $h = 6.625 \times 10^{-34}$ j/s and v is the frequency of the wave:

$$\epsilon = h\,v \qquad (1.2)$$

Because different waves carry different amounts of energy, waves behave differently.

Figure 1.2 represents the electromagnetic spectrum, which shows the different

categories of electromagnetic waves.
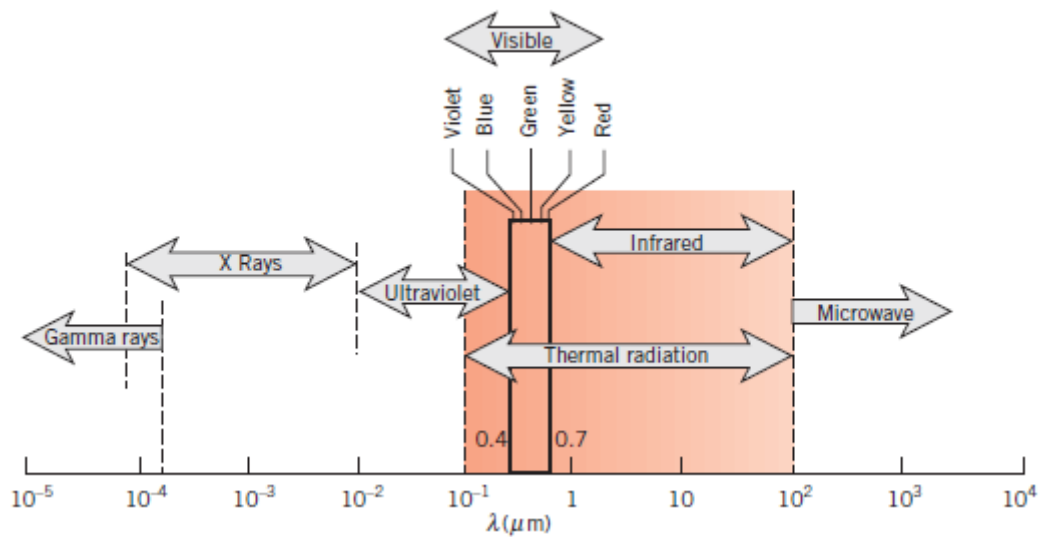
Figure 1.2: radiation spectrum from Ref. [47]

The portion of the electromagnetic spectrum that is of interest for thermal radiation falls between wavelengths of 0.1 and 100 micrometers. This part of the spectrum contains parts of the ultraviolet, visible, and infrared radiations.

1.3.2 Solid angle

The solid angle is an important parameter in radiative heat transfer, used to define other parameters such as radiative heat flux, and radiative intensity. Since both latter parameters will be used in subsequent sections of this paper, the solid angle must be defined.

Despite the sun being significantly larger than the human hand, a hand can be used as a shield from the sun. This is possible because the sun is substantially further away from the hand, and hence the sun subtends a smaller angle. This is a simplified example of what a solid angle is.

8

The solid angle in Fig. 1.3 is defined as the projection of surface dA_j, as observed from point P, onto a plane normal to the direction between point P and the surface, divided by the square of the distance [15].

The total solid angle is defined as the total hemispherical area above point P, as shown in Fig. 1.3. The total solid angle can be expressed in terms of the polar angle θ, where $0 < \theta < \pi/2$, and the azimuthal angle ψ, where $0 < \psi < 2\pi$
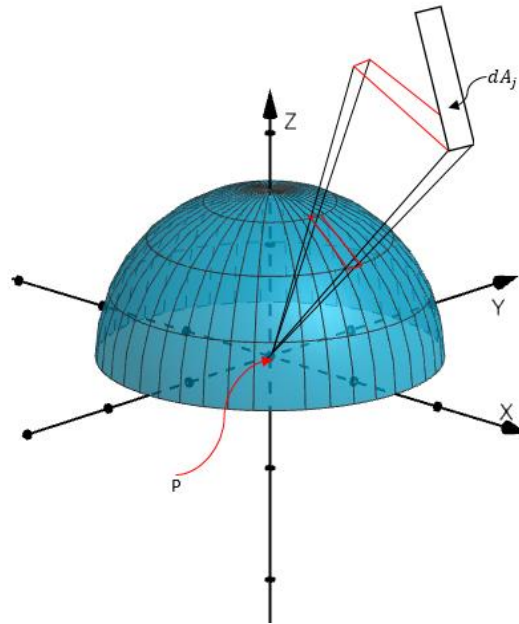
Figure 1.3: solid angle

If the hemisphere is a unit hemisphere, the solid angle is equal to:

$$d\Omega = \frac{dA_{jp}}{S^2} = \frac{cos\theta_j\, dA_j}{S^2} = dA_j'' \qquad (1.3)$$

Thus, the infinitesimal solid angle can be expressed as

$$d\Omega = dA_j'' = sin\theta\, d\psi\, d\theta \qquad (1.4)$$

9

Integrating Eq. 1.4 over all directions, results in the following relation:

$$\int_{\psi=0}^{2\pi} \int_{\theta=0}^{\pi/2} \sin\theta \ d\psi \ d\theta = 2\pi \qquad (1.5)$$

1.3.3 Intensity ,Emission, Incident radiation

All matter at a temperature above absolute zero, emit radiation in all directions. With the directional dependence of radiation, there is a need to describe the radiative heat flux as a function of direction. Radiative intensity is defined as the energy flow per unit area normal to the direction of propagation, per solid angle.

$$I(\theta,\psi) = \frac{dQ}{dA \ \cos\theta \ d\Omega} = \frac{dQ}{dA \ \cos\theta \ \sin\theta \ d\theta \ d\psi} \qquad (1.6)$$

Unlike intensity, emitted radiation is only a function of the area. Emitted radiation can be defined as the rate at which energy is emitted per unit area, and it is related to the intensity as follows:

$$dE = \frac{dQ}{dA} = I(\theta,\psi) \times \cos\theta \ \sin\theta \ d\theta \ d\psi \qquad (1.7)$$

Integrating the previous equation over the entire hemisphere yields the following:

$$E = \int dE = \int_{\psi=0}^{2\pi} \int_{\theta=0}^{\frac{\pi}{2}} I(\theta,\psi) \cos\theta \ \sin\theta \ d\theta \ d\psi \qquad (1.8)$$

Some surfaces can be approximated as diffusive surfaces, where the intensity $I(\theta,\psi)$ is a constant, and the previous equation can be reduced into:

$$E = \pi \ I(r,\hat{s}) \qquad (1.9)$$

10

Since blackbodies are diffusive emitters; the black body emission, $E_b = \sigma T^4$, can be

expressed in terms of intensity:

$$E_b = \pi \, I_b \qquad (1.10)$$

And the blackbody intensity as a function of the absolute temperature becomes:

$$I_b = \frac{\sigma T^4}{\pi} \qquad (1.11)$$

Incident radiation is another term used in radiative heat transfer. Incident radiation

can be defined as the rate of radiation energy incident on a surface, per unit area, per

solid angle. Incident radiation flux on a surface from all solid angle directions is known

as irradiation, and can be described as:

$$G = \int dG = \int_{\psi=0}^{2\pi} \int_{\theta=0}^{\frac{\pi}{2}} I_i(\theta, \psi) \, sin\theta \, cos\theta \, d\theta \, d\psi \qquad (1.12)$$

where G has SI units of w/m²

In most applications, the total quantities discussed earlier are sufficient. However, for

this work, there is a need to consider the spectral quantities, which depend on the

wavelength as well as the direction.

Spectral intensity is the emitted radiation, per unit area, per unit solid angle, at a

specific wavelength. Spectral intensity can be expressed as:

$$I(\lambda, \theta, \psi) = \frac{dQ}{dA \, cos\theta \, d\Omega \, d\lambda} \qquad (1.13)$$

The spectral emissive power can be expressed as:

$$E_\lambda = \int_{\psi=0}^{2\pi} \int_{\theta=0}^{\pi/2} I(\lambda, \theta, \psi) \, cos\theta \, sin\theta \, d\theta \, d\psi \qquad (1.14)$$

It is possible to relate the total and spectral quantities through an integration over the entire wavelength spectrum. For example, total and spectral intensities are related through the following equation:

$$I(r, \hat{s}) = \int_0^\infty I(\lambda, r, \hat{s}) \, d\lambda \qquad (1.15)$$

Max Planck provided the spectral intensity of emitted radiation by a blackbody as a function of absolute temperature and wavelength:

$$I_{b\lambda}(\lambda, T) = \frac{2hc^2}{\lambda^5 \left(\exp\left[\frac{hc}{\lambda \, \sigma \, T}\right] - 1\right)} \qquad (1.16)$$

where h is the Planck constant which is equal to 6.6256×10^{-34} J.s, σ is the Boltzmann constant equal which is equal to 1.38065×10^{-23} J/K, and c is the speed of light which is equal to 2.9979×10^8 m/s.

1.3.4 Radiative heat flux

Heat flux is usually defined as the amount of energy passing through a surface. For radiative heat transfer, the radiative heat flux can be related to the intensity as follows:

$$dQ = I_\lambda \, d\Omega \, dA = I_\lambda \, d\Omega \, dA \, cos\theta \qquad (1.17)$$

the angle θ in Eq. 1.17 represents the angle between the direction of propagation, and the direction normal to the surface. The previous equation can be presented after integrating over the solid angles as:

$$q_\lambda = \int_{4\pi} I_\lambda(\hat{s})\,\hat{n}.\hat{s}\ d\Omega \qquad\qquad (1.18)$$

And the total radiative heat flux can be obtained by integrating over the wavelength

spectrum:

$$q.n = \int_0^\infty \int_{4\pi} I_\lambda(\hat{s})\,\hat{n}.\hat{s}\ d\Omega\ d\lambda \qquad\qquad (1.19)$$

1.3.5 Radiative properties

Depending on the wavelength of radiation, materials exhibit different behaviors. For

example, visible radiation can penetrate through water, while infrared radiation cannot,

making water a transparent medium in visible radiation, and an opaque medium in

infrared radiation. This wavelength dependence is extremely important especially in this

study.

1.3.5.1 Emissivity

Emissivity is a property that compares the emitted radiation from a surface to the

blackbody emission at the same temperature. The value if emissivity, ϵ, varies between

zero and one, where a value of one represents the blackbody emission.

The value of emissivity depends on the direction, wavelength, and temperature. The

dependence of emissivity on such variables could vary its value within a surface. This

variance must be considered if spectral radiation is of interest.

Spectral emissivity can be defined as the ratio of emitted radiation in a specified direction and wavelength, to the blackbody emission at the same temperature and wavelength:

$$\epsilon_\lambda(\lambda, \theta, \psi. T) = \frac{I_\lambda(\lambda, \ \theta, \psi, T)}{I_{b\lambda} \ (\lambda, T)} \qquad (1.20)$$

The total emissivity is defined as the emitted radiation in a specified direction, to the total blackbody emissive radiation:

$$\epsilon \ (\theta, \psi, T) = \frac{I(\theta, \ \psi, T)}{I_b(T)} \qquad (1.21)$$

Sometimes it is more convenient to use properties averaged over all directions (hemispherical properties). Knowing that the integration of emitted intensity over all directions is defined as the emissive power, the hemispherical emissivity is defined as:

$$\epsilon = \frac{E(\lambda, T)}{E_b(\lambda, T)} \qquad (1.22)$$

With all the complexities associated with radiation, sometimes it is useful to use certain approximations to simplify calculations. For instance, gray and diffuse approximations can be used. A gray surface is one with properties that are wavelength independent. A diffuse surface is one with directional independent properties. For instance, the emissivity of a gray diffuse surface is equivalent to the total hemispherical emissivity.

1.3.5.2 Absorptivity, reflectivity, Transmissivity

When there is an interaction between radiation and a material, part of the radiation gets reflected, another part gets absorbed within the medium, and the remaining part is transmitted. Absorptivity is defined as the fraction of absorbed radiation to the total incident radiation, and can be expressed as:

$$\alpha = \frac{G_{absorbed}}{G} \qquad (1.23)$$

where the value of absorptivity α is between zero and one. An absorptivity of one indicates that the entire incident radiation is absorbed.

Reflectivity is another fraction relating the reflected wave potion to the incident total radiation, and can be expressed as:

$$\rho = \frac{G_{reflected}}{G} \qquad (1.24)$$

The value of reflectivity, ρ, is between zero and one; where one indicates that the entire incident radiation is reflected

Lastly, transmissivity relates the transmitted radiation to the total incident radiation, and can be expressed as:

$$\tau = \frac{G_{transmitted}}{G} \qquad (1.25)$$

Like reflectivity and absorptivity, the value of transmissivity, τ, falls between zero and one. A value of one indicates that the entire incident radiation was transmitted and passed through the surface.
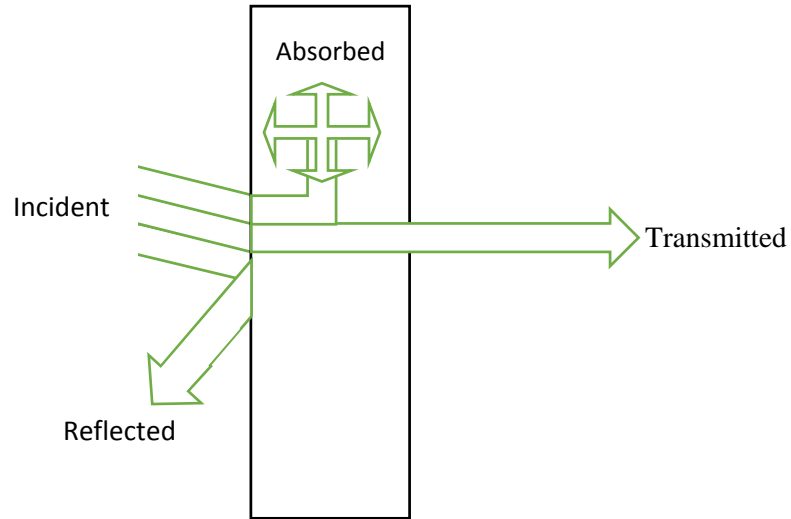
Figure 1.4 incident radiation

The sum of the three portions; absorbed, reflected, and transmitted radiations, must be equal to the total incident radiation.

$$G_{absorbed} + G_{reflected} + G_{transmitted} = G \qquad (1.26)$$

The following can be obtained by dividing Eq. 1.26 by the incident radiation, G:

$$\alpha + \rho + \tau = 1 \qquad (1.27)$$

The previously discussed properties are the total hemispherical properties, which means that, they are directional and wavelength independent.

Spectral directional absorptivity is defined as the fraction of absorbed directional intensity at a specific wavelength, to the total incident directional intensity at a specific wavelength. Spectral directional absorptivity can be expressed as:

$$\alpha_{\lambda,\theta}(\lambda, \theta, \psi) = \frac{I_{\lambda,absorbed}(\lambda, \theta, \psi)}{I_\lambda(\lambda. \theta, \psi)} \qquad (1.28)$$

Spectral directional reflectivity is defined in a similar manner; it is considered as the

fraction of reflected directional intensity, to the total incident directional intensity, and

is expressed as:

$$\rho_{\lambda,\theta}\ (\lambda,\theta,\psi) = \frac{I_{\lambda,reflected}\ (\lambda,\theta,\psi)}{I_{\lambda}(\lambda.\,\theta,\psi)} \tag{1.29}$$

Unlike other properties, reflectivity depends on both the incident radiation as well as

the reflected radiation. As shown in Fig. 1.5 (A), the reflected rays from a real surface

form an irregular shape, which complicates the analysis. To overcome this issue, two

assumptions are usually made. Firstly, the surface is assumed to be diffuse, as shown in

Fig. 1.5 (B), which means that the reflected radiation is assumed equal in all directions.

Secondly, the surface is assumed specular, as shown in Fig. 1.5 (C), and hence the angle

of incidence is assumed equivalent to the angle of reflection.
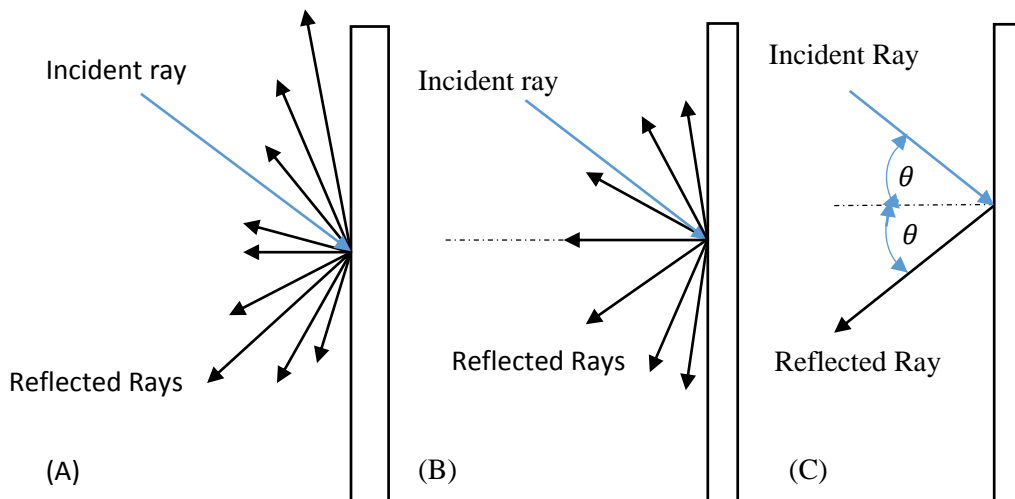
Figure 1.5 reflected rays (A) Real, (B) diffuse, and (C) specular surface

Chapter 2

2.1 Modeling radiation transport

As discussed previously, radiative heat transfer differs from the other heat transfer mechanisms in the way it is modeled. The behavior of radiative heat transfer within an absorbing, emitting, and scattering medium is governed by the radiative transfer equation. The radiative transfer equation describes the radiative intensity field as a function of location, spectral properties, and direction.

To obtain the radiative heat flux, all contributions from all directions and wavelengths should be accounted for. Integrating the equation over all directions and wavelengths leads to the conservation of radiative energy over an infinitesimal volume. Once combined with conduction, the overall conservation of energy is obtained.

The radiative transfer equation describes the change occurring for a radiative intensity beam when a participating medium is penetrated. Those changes could be categorized into two categories: attenuation and augmentation.

2.1.1 Attenuation

Attenuation describes the decrease in radiative intensity as radiation moves through a medium. This occurs due absorption within the medium, as well as out-scattering, as shown schematically in Fig. 2.1.
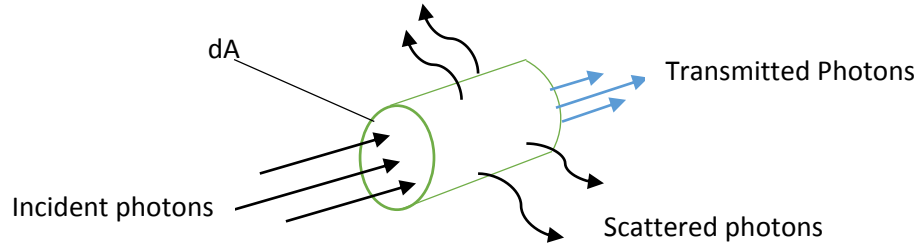
Figure 2.1 attenuation due to scattering

2.1.1.1 Attenuation due to absorption

As the intensity ray travels through a participating medium, part of it gets absorbed and transformed into internal energy. Absorption is proportional to the magnitude of incident energy, as well as distance traveled by an intensity beam through a medium. This is described mathematically as follows:

$$dI = -\kappa_\eta I_\eta ds \qquad (2.1)$$

where κ_η is the absorption coefficient, and ds is the distance traveled by the intensity beam within the medium. Integrating Eq. 2.1 over distance yields:

$$I_\eta(S) = I_\eta(0)\ e^{-\tau} \qquad (2.2)$$

where $I_\eta(0)$ is the intensity entering the medium, $I_\eta(S)$ is the intensity leaving the medium, and τ is the absorption optical thickness expressed as:

$$\tau = \int_0^S \kappa_\eta\ ds \qquad (2.3)$$

2.1.1.2 Attenuation by scattering

Attenuation by scattering describes the portion removed from the intensity beam due to out-scattering. Out-scattering is considered to redirect energy from one direction

to another, making it appear as augmentation. The attenuation due to out-scattering can be expressed as:

$$dI_\eta = -\sigma_\eta \, I_\eta \, ds \qquad\qquad (2.4)$$

where σ_η is the scattering coefficient, and is a property of the medium. It is also possible to define an optical thickness based on scattering, by integrating the previous equation, similar to before:

$$I_\eta(S) = I_\eta(0) \; e^{-\tau} \qquad\qquad (2.5)$$

$$\tau = \int_0^S \sigma_\eta \, ds \qquad\qquad (2.6)$$

2.1.1.3 Total attenuation

As discussed previously, attenuation is due to both out-scattering, as well as absorption. It is more convenient to deal with properties that account for both. The total attenuation that occurs for radiative intensity is called extinction. The extinction coefficient is defined as:

$$\beta_\eta = \kappa_\eta + \sigma_\eta \qquad\qquad (2.7)$$

and the optical thickness based on the extinction coefficient is defined as:

$$\tau \; = \; \int_0^S \beta \, ds \qquad\qquad (2.8)$$

2.1.2 Augmentation

Augmentation accounts for energy added to the intensity pencil ray as it travels through a medium. Augmentation occurs mainly because of emission, as well as in-

scattering, which accounts for the scattered radiation from directions other than that of traveling.

2.1.2.1 Emission

Emission accounts for the energy gain from a small element and is proportional to the element's volume. Recalling the definition of emitted intensity as the emitted energy per unit area; one can conclude that the emission is proportional to the distance traveled by intensity within the medium. The energy gain due to emission can be expressed as follows:

$$dI_\eta = \kappa_\eta \, I_\eta \, ds \qquad\qquad (2.9)$$

where κ_η is the emission constant. The emission constant is equivalent to the absorption coefficient. If the emission and absorption equations are taken into account, the transfer equation describing the change in intensity within an absorbing-emitting, but non scattering medium, can be obtained as follows:

$$\frac{dI_\eta}{ds} = \kappa_\eta \left(I_{b\eta} - I_\eta \right) \qquad\qquad (2.10)$$

the first term on the right side of Eq.2.10 accounts for augmentation due to emission, and the second term accounts for the attenuation due to absorption.

2.1.2.2 Augmentation due to scattering

Augmentation due to scattering is the addition of energy to an intensity ray traveling

in one direction, from the other directions.
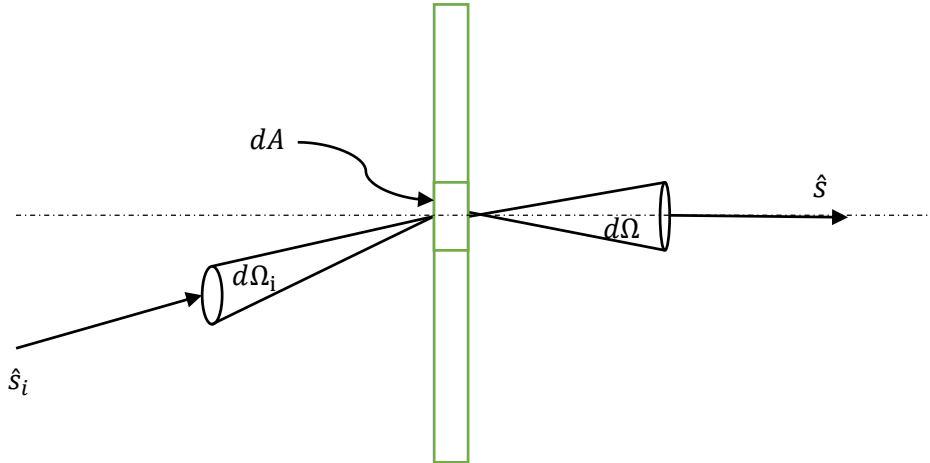
Figure 2.2 scattered intensity from direction $\hat{s}_i$ into direction $\hat{s}$

Recalling the definition of intensity as the radiative flux per unit area normal to the

ray, per unit wavelength, and per unit solid angle. It is possible to calculate the radiative

heat flux striking a volume element, as shown in Fig. 2.2, from direction $\hat{s}_i$, using the

following formula:

$$I_\eta(\hat{s}_i) \, dA \, \hat{s}_i . s \; d\Omega \, d\eta \qquad\qquad (2.11)$$

The distance the flux travels within the control volume dV is $\frac{ds}{\hat{s}_i.\hat{s}}$, and the total

energy scattered from direction $\hat{s}_i$ is:

$$\sigma_\eta \left(I_\eta(\hat{s}_i) \, dA \, \hat{s}_i . s \; d\Omega \, d\eta \right) \left(\frac{ds}{\hat{s}_i.\hat{s}} \right) = \sigma_\eta \, I_\eta(\hat{s}_i) \, dA \, d\Omega \, d\eta \, ds \qquad\qquad (2.12)$$

Only a fraction of that scattered energy will be added to direction $\hat{s}$, this fraction can be described using the scattering phase function Φ_η, known as the probability that the intensity from direction $\hat{s}_\iota$ will be scattered into direction $\hat{s}$

$$\sigma_\eta \, I_\eta(\hat{s}_\iota) \, dA \, d\Omega_i \, d\eta \, ds \, \frac{\Phi_\eta(\hat{s}_\iota \cdot \hat{s})}{4\pi} \, d\Omega \qquad (2.13)$$

the fraction $\Phi_\eta (\hat{s}_\iota \cdot \hat{s}) d\Omega/4\pi$ represents the fraction that is scattered into the solid angle in direction $\hat{s}$. Integrating Eq. 2.13 over all solid angle directions provides the total in-scattering term:

$$dI_\eta(\hat{s}) \, dA \, d\Omega \, d\eta \; = \; \int_{4\pi} \sigma_\eta \, I_\eta(\hat{s}_\iota) \, dA \, d\Omega \, d\eta \, ds \, \Phi \, (\hat{s}_\iota \cdot \hat{s}) \frac{d\Omega}{4\pi} \qquad (2.14)$$

or

$$dI_\eta(\hat{s}) \; = \sigma_\eta \frac{ds}{4\pi} \int_{4\pi} I_\eta(\hat{s}_\iota) \, \Phi \, (\hat{s}_\iota \cdot \hat{s}) d\Omega \qquad (2.15)$$

for isotropic scattering, the term $\frac{1}{4\pi} \int_{4\pi} \Phi(\hat{s}_\iota \cdot \hat{s}) \, d\Omega$ is equal to one. It indicates that scattering is equal in all directions.

2.2 Radiative transfer equation

The radiative transfer equation provides an energy balance, combining all four contributions discussed earlier. The equation describes the change occurring to an intensity ray as it travels through a participating medium, as shown in Fig. 2.3.
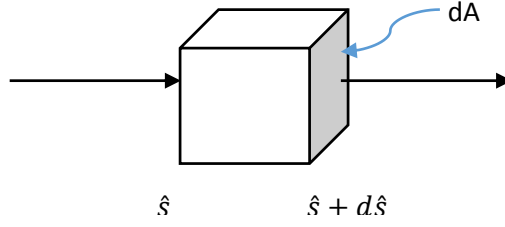
Figure 2.3 Intensity propagation within participating medium

Summing all the equation's components discussed earlier, the following results:

$$I_\eta(s + ds, \hat{s}, t + dt) - I_\eta(s, \hat{s}, t)$$

$$= \kappa I_B(s, t) \, ds - \kappa I_\eta(s, \hat{s}, t) ds - \sigma_\eta \, I(s, \hat{s}, t) \, ds$$

$$+ \frac{\sigma}{4\pi} \int_{4\pi} I_\eta(s_i) \Phi(\hat{s}_i, \hat{s}) d\Omega \, ds \qquad (2.16)$$

Since the ray travels at the speed of light, it is possible to relate the speed of light and distance traveled, using $ds = c \, dt$. Doing so yields the following equation:

$$\frac{1}{c}\left(\frac{\partial I_\eta}{\partial t}\right) + \frac{\partial I_\eta}{\partial s} = \kappa \, I_b - \kappa \, I_\eta - \sigma \, I_\eta + \frac{\sigma}{4\pi} \int_{4\pi} I_\eta(s_i) \, \Phi(s_i.s) \, d\Omega \qquad (2.17)$$

For most engineering applications, the speed of light is extremely large compared to the time scales of the application. Hence, the first term in the previous equation can be dropped out, leading to the following equation:

$$\frac{\partial I_\eta}{\partial s} = \hat{s}. \nabla \, I_\eta = \kappa \, I_b - \beta \, I_\eta + \frac{\sigma}{4\pi} \int_{4\pi} I_\eta(s_i) \, \Phi(s_i.s) \, d\Omega \qquad (2.18)$$

where β is the extinction coefficient $\beta = \sigma + \kappa$.

The radiative transfer equation is often expressed in terms of the scattering albedo defined as:

$$\omega = \frac{\sigma}{\kappa + \sigma} = \frac{\sigma}{\beta} \qquad\qquad (2.19)$$

which leads to:

$$\frac{\partial I_\eta}{\partial s} = (1 - \omega)I_b - I_\eta + \frac{\omega}{4\pi} \int_{4\pi} I_\eta(s_i) \, \Phi(s_i.s) \, d\Omega \qquad\qquad (2.20)$$

The radiative transfer equation described, is an integro-differential equation, with six variables: three in space, two directional, and the last variable being the wavelength. This multivariable equation is a complicated equation. It cannot be solved except for very special and simplified cases. Most of the simplified cases do not fulfill practical needs, yet, solving the equation is needed for practical applications. Many approximating numerical solutions are used to solve the equation; some of them will be discussed in the following section.

2.3 Solution methods to the RTE
2.3.1 The flux method

This method was proposed by Schuster [38] and Schwarzchild [39] to solve one dimensional problems. The main idea behind this method is dividing the entire solid angle into two solid angles as shown in Fig. 2.5. The magnitude in each solid angle direction is assumed to be uniform but different. Radiative energy is allowed to travel in all directions.
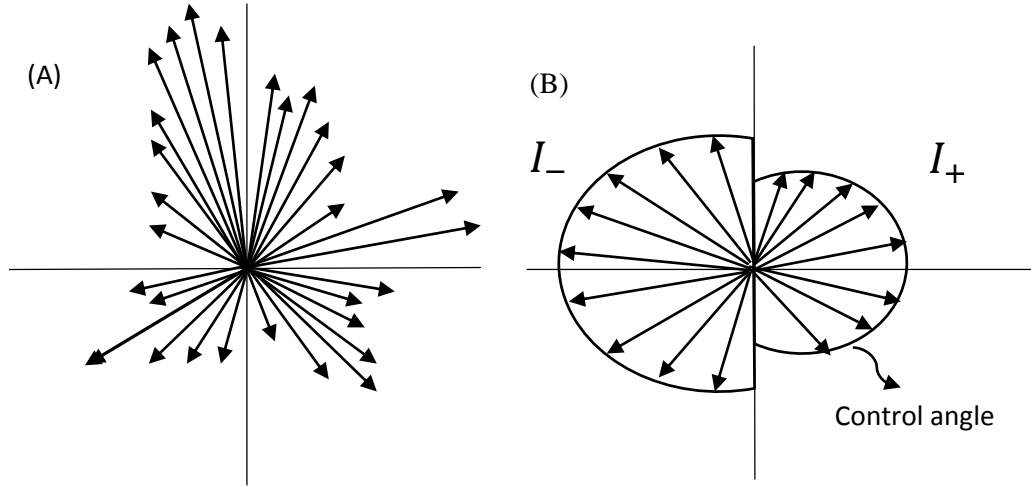
Figure 2.4   Intensity distribution A- real infinite directions   b- Two flux method

By assuming there are only two directions for radiation propagation, the radiative transfer equation is reduced into two partial differential equations, one equation for each direction.

$$I = I^+ \quad n.\hat{s} > 0 \quad (positive\ direction)$$

$$I = I^- \quad n.\hat{s} < 0 \quad (negative\ dirction)$$

Using $\phi = 1$ (isotropic scattering), the radiative transfer equation can be defined as

$$\frac{dI^+}{dx} = -\beta\ I^+ + \kappa\ I_b + \frac{\sigma}{4\pi}\ (I^+ + I^-) \qquad (2.21)$$

Integrating Eq. 2.30 over the positive solid angle yields:

$$\frac{dI^+}{dx} \int_{n.s>0} n.s\ d\omega = \left[-\beta\ I^+ + \kappa\ I_b + \frac{\sigma}{2}(I^+ + I^-) \right] \int_{n.s>0} d\Omega \qquad (2.22)$$

or

$$\frac{1}{2}\frac{dI^+}{dx} = -\beta\ I^+ + \kappa\ I_b + \frac{\sigma}{2}(I^+ + I^-) \qquad (2.23)$$

26

By repeating the previous step for the other direction, and integrating afterwards, a similar formula is obtained for the negative direction.

$$\frac{1}{2}\frac{dI^-}{dx} = -\beta\,I^- + \kappa\,I_b + \frac{\sigma}{2}(I^+ + I^-) \qquad (2.24)$$

2.3.2 Discrete Ordinates Method

The discrete ordinates method is one of the methods used to solve the radiative transfer equation discussed in the previous section. It was first introduced by Chandrasekar [24] in his stellar and atmospheric radiation work. The method was applied to problems in neutron transport theory by Lee [25] and Lathrop [26, 27]. Early attempts were done by Love [28, 29] and Hottel [30] to use the method with one dimensional planer thermal radiation problems. Lately this method has been applied and optimized for radiative transfer applications by Fiveland [31-33] and Truelove [35-37]

(A)   (B)
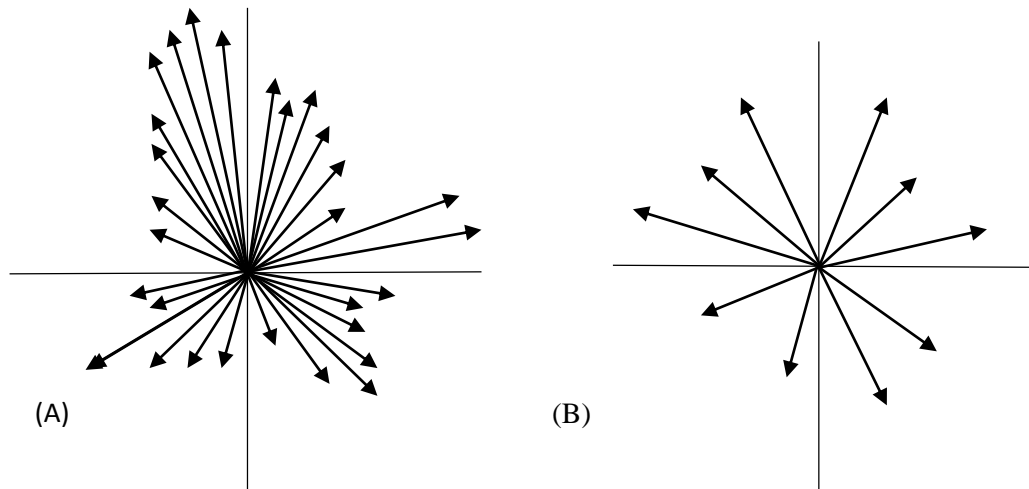
Figure 2.5 Intensity distribution A- real infinite directions   B- finite discrete directions

The discrete ordinates method divides angular space into a finite number of control angles (directions shown in Fig 2.4 A), enabling the transformation of the radiative transfer equation into a set of linear equations. Each one of the equations is associated with a direction. In addition, the evaluation of integrals is done using numerical quadrature schemes.

The general radiative transfer equation for an emitting, absorbing, and scattering medium is:

$$\frac{\partial I_\eta}{\partial s} = \hat{s}.\nabla I_\eta = \kappa I_b - \beta I_\eta + \frac{\sigma}{4\pi} \int_{4\pi} I_\eta(s_i) \, \Phi(s_i.s) \, d\Omega \qquad (2.25)$$

The equation is subject to diffusive emitting reflecting boundary conditions:

$$I(r,\hat{s}) = \epsilon I_b + \frac{\rho}{\pi} \int_{n.s<0} I(r,\hat{s}) \, |n.\hat{s}| \, d\Omega \qquad (2.26)$$

where ϵ is the wall emissivity, ρ is the wall reflectivity equal to $\rho = 1 - \epsilon$, $\hat{n}$ is the normal to the surface, and $\hat{s}$ is the direction of intensity propagation. The discrete ordinates formulation of the radiative transfer equation is as follows:

$$\hat{s}_i.\nabla I(r,\hat{s}_i) = \kappa(r)I_b(r) - \beta(r)I(r,\hat{s}_i) + \frac{\sigma}{4\pi} \sum_j^n \omega_j \, I(r,s_j) \, \Phi(r,s_i,s_j) \qquad (2.27)$$

subject to the boundary condition:

$$I(r,\hat{s}) = \epsilon(r) I_b + \frac{\rho}{\pi} \sum_{n.s<0} \omega_j \, I(r,\hat{s}_j) \, |n.\hat{s}| \qquad (2.28)$$

For one dimentional problems Eq. 2.23 can be reduced to the following:

28

$$\mu \frac{dI}{dx} = -\beta\, I + \kappa\, I_b + \frac{\sigma}{4\pi} \sum_{l=1}^{L} I\, \phi^{l'l}\, w \qquad (2.29)$$

where μ is the directional cosine, and ω is the quadrature weight.

Choosing a quadrature scheme is arbitrary, but restrictions must be applied and must satisfy the following relations:

$$\int_{4\pi} d\Omega = 4\pi = \sum_{i}^{n} w_i \qquad (2.30)$$

$$\int_{4\pi} \hat{s}\, d\Omega = 0 = \sum_{i}^{n} w_i \hat{s} \qquad (2.31)$$

$$\int_{4\pi} \hat{s}.\hat{s}\, d\Omega = \frac{4\pi}{3} \delta = \sum_{i}^{n} w_i\, \hat{s}.\hat{s} \qquad (2.32)$$

The following half moment equation has to be satisfied as well;

$$\int_{n.s<0} |n.\hat{s}|\, d\Omega = \int_{n.\hat{s}>0} n.\hat{s}\, d\Omega = \pi = \sum_{n.\hat{s}>0} w_i\, n.\hat{s} \qquad (2.33)$$

The discrete ordinates method suffers multiple drawbacks, such as false scattering occuring due to spatial discretization, and ray effect occuring as a result of angular discretization. Both of the drawbacks produce negative intensities, which are nonphysical. The major drawback for the discrete ordinates method is that it does not ensure energy conservation, as a result of using the Gaussian quadrature for angular discretization.

2.3.3 Spherical harmonics

Spherical harmonics is a method transforming the radiative transfer equation into a set of partial differential equations. The method was first introduced by Jeans [40], further explanation can be found as done by Kourganoff [41], Davidson [42], and Murray [43]. The full derivation of this method can be found by Modest [15].

The intensity field at a location, *r*, can be described using spherical harmonics. Spherical harmonics are considered as special functions defined on a spherical surface, and can be expressed in terms of a Fourier series as

$$I(r,\hat{s}) = \sum_{l=0}^{\infty} \sum_{m=-1}^{l} I_l^m(r) \, Y_l^m(\hat{s}) \qquad (2.34)$$

where I_l^N are coefficients that depends on the position, and Y_l^N is the spherical harmonics function expressed as

$$Y_l^m(\hat{s}) = (-1)^{\frac{m+|m|}{2}} \left[\frac{(l-|m|)!}{(l+|m|)!} \right]^{1/2} e^{im\psi} \, P_l^{|m|} \cos(\theta) \qquad (2.35)$$

where θ is the polar angle, ψ is the azimuthal angle, and P_w^N are the associated Legendre polynomials.
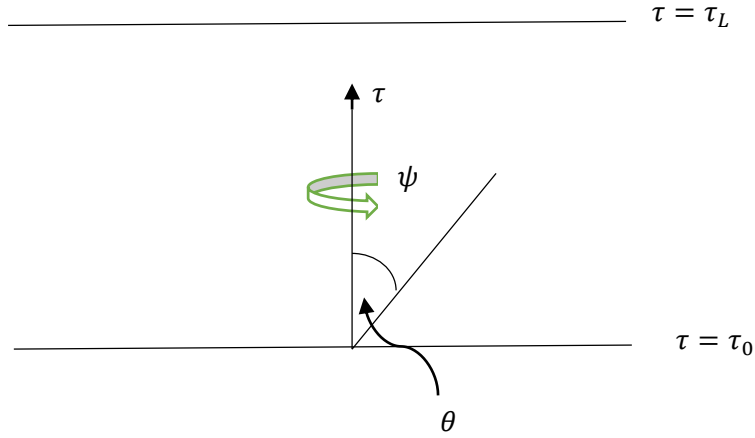
Figure 2.6 one dimensional coordinates for parallel plane medium

For a plane medium, the intensity does not depend on the azimuthal angle ψ. θ is assumed measured similar to what is shown in Fig. 2.6. Equation 2.35 can be simplified into

$$I(\tau,\mu) = \sum_{l=0}^{N} I_l(\tau)\, P_l(\mu) \qquad (2.36)$$

the phase function can be expressed as

$$\Phi(\mu,\mu') = \sum_{m=0}^{M} A_m\, P_m(\mu')\, P_m(\mu) \qquad (2.37)$$

$$\int_{-1}^{1} \Phi(\mu,\mu')\, I(\tau,\mu')\, d\mu' = \sum_{l=0}^{N} I_l(\tau) \sum_{m=0}^{M} A_m\, P_m(\mu) \int_{-1}^{1} P_l(\mu') P_m(\mu') d\mu' \qquad (2.38)$$

Utilizing the orthogonally for the Legendre polynomials

$$\int_{-1}^{1} P_l(\mu)\, P_m(\mu)\ d\mu = \frac{2\delta}{2m+1} = \left\{ \frac{2}{2m+1} \text{ for } m = 1; 0 \text{ for } m \neq 1 \right\} \qquad (2.39)$$

31

Employing this orthogonal relation in Eq. 2.38 gives

$$\int_{-1}^{1} \Phi(\mu,\mu') \, I(\tau,\mu') \, d\mu' = \sum_{i=0}^{N} \frac{2A_i}{2i+1} \, I_i(\tau) P_i(\mu) \qquad (2.40)$$

For a one-dimensional parallel plane, the radiative transfer equation is presented as:

$$\mu \frac{dI}{ds} + I(\tau) = (1 - \omega)I_b(\tau) + \frac{\omega}{2} \int_{-1}^{1} \Phi(\mu,\mu')I(\mu,\mu')d\mu' \qquad (2.41)$$

or

$$\sum_{i=0}^{N} \left[\frac{dI_i}{d\tau} \mu \, P_l(\mu) + I_l(\tau)P_l(\mu) \right] = (1 - \omega)I_b(\tau) + \omega \sum_{i}^{N} \frac{A_l I_l(\tau)}{2l+1} \, P_l(\mu) \qquad (2.42)$$

Marshak proposed a boundary condition for the spherical harmonics, describing the intensity for a diffusive emitting reflecting wall:

$$\int_{0}^{1} I(0,\mu) \, P_{2l-1}(\mu)d\mu = \int_{0}^{1} I_{w1}(\mu)P_{2i-1}(\mu) \, d\mu \qquad i = 1,2,\ldots \frac{1}{2}(N+1) \qquad (2.43)$$

$$\int_{-1}^{0} I(0,\mu) \, P_{2l-1}(\mu)d\mu = \int_{-1}^{0} I_{w2}(\mu)P_{2i-1}(\mu) \, d\mu \qquad i = 1,2,\ldots \frac{1}{2}(N+1) \qquad (2.44)$$

2.3.3.1 P1 approximation

The P1 approximation is considered as the lowest order of the spherical-harmonics method described earlier. The approximation can be obtained by truncating Eq. 2.34 after $l = 1$, resulting in the following equation:

$$I(r,\hat{s}) = I_0^0 Y_0^0 + I_1^{-1} Y_1^{-1} + I_1^0 Y_1^0 + I_1^1 Y_1^1 \qquad (2.45)$$

Using the associate Legendre polynomials by MacRobert [44], it is possible to describe the intensity field as follows:

$$I(r,\theta,\psi) = I_0^0 + I_1^0 \cos(\theta) - \frac{1}{\sqrt{2}} \left(I_1^1 e^{i\psi} - I_1^{-1} e^{-i\psi} \right) \sin(\theta)$$

$$= I_0^0 + I_1^0 \cos(\theta) + \frac{1}{\sqrt{2}} (I_1^{-1} - I_1^1) \sin(\theta) \cos(\psi)$$

$$- \frac{1}{\sqrt{2}} (I_1^{-1} - I_1^1) \sin(\theta) \sin(\psi) \qquad (2.46)$$

the first term in the previous equation is directionally independent, the second term is proportional to the *z* component of the direction vector, the third term is proportional to the *x* component of the direction, and the last term is proportional to the *y* component of the direction.

A compact form of the previous relation can be presented as follows:

$$I(r,\hat{s}) = a(r) + b(r).\hat{s} \qquad (2.47)$$

Substituting Eq. 2.47 in the definition of the incident radiation will produce the following:

$$G(r) = \int_{4\pi} I(r,\hat{s}) \, d\Omega = a(r) \int_{4\pi} d\Omega + b(r) . \int_{4\pi} \hat{s} \, d\Omega = 4\pi \, a(r) \qquad (2.48)$$

By substituting the intensity, defined in Eq. 2.47, in the radiative heat flux equation, the following can be obtained

$$q(r) = \int_{4\pi} I(r,\hat{s}) \, \hat{s} d\Omega = a(r) \int_{4\pi} d\Omega + b(r) . \int_{4\pi} \hat{s}.\hat{s} \, d\Omega = \frac{4\pi}{3} b(r) \qquad 2.49$$

33

Using both, the incident radiation and the radiative heat flux, the equation can be

written as

$$I(r,\hat{s}) = \frac{1}{4\pi}\,[G(r) + 3\,q(r).\hat{s}]\qquad\qquad(2.50)$$

The linear anisotropic relation is described by:

$$\Phi(\hat{s}.\hat{s}') = 1 + A_1\,\hat{s}.\hat{s}'\qquad\qquad(2.51)$$

By substituting Eq. 6.30 and Eq. 6.31 into the radiative transfer equation, the following

can be obtained

$$\int_{4\pi} I(\hat{s}')\,\Phi(\hat{s}.\hat{s}')\,d\Omega = \frac{1}{4\pi}\int_{4\pi}(G + 3\,q.\hat{s}\,)(\,1 + A_1\,\hat{s}.\hat{s}')\,d\Omega'$$

$$= \frac{G}{4\pi}\left[\int_{4\pi} d\Omega' + A_1\,\hat{s}\,.\int_{4\pi}\hat{s}'\,d\Omega'\,\right] + \frac{3q}{4\pi}\left[\int_{4\pi}\hat{s}'d\Omega' + A_1\,(\int_{4\pi}\hat{s}\,\hat{s}\,d\Omega')\,.\hat{s}\right]$$

$$= G + A_1\,q.\hat{s}\qquad\qquad(2.52)$$

After multiple manipulations, as can be found in Modest [15], it is possible to obtain

two relations: one gives an expression for the radiative heat flux as a function of the

incident radiation, and the other gives an expression for the incident radiation as a

function of the radiative heat flux, more specifically

$$\nabla.q = (1 - \omega)(\,4\pi I_b - G)\qquad\qquad(2.53)$$

$$\nabla G = (-3 - A_1\,\omega\,)\,q\qquad\qquad(2.54)$$

The previous two equations forms the P1 approximation, representing a set of

equations solved for the unknown incident radiation and radiative heat flux. The

numerical solution for these equations will be described in later sections.

2.3.4 Finite volume method

The finite volume method approximates the radiative transfer equation by double

integrating it directly over control angles, as well as control volumes. The finite volume

method divides angular space into several control angles, where the intensity is

considered constant, as shown in Fig. 2.7. By doing so, a set of equations is produced.

Each equation represents a direction and can be solved with proper boundary

conditions.
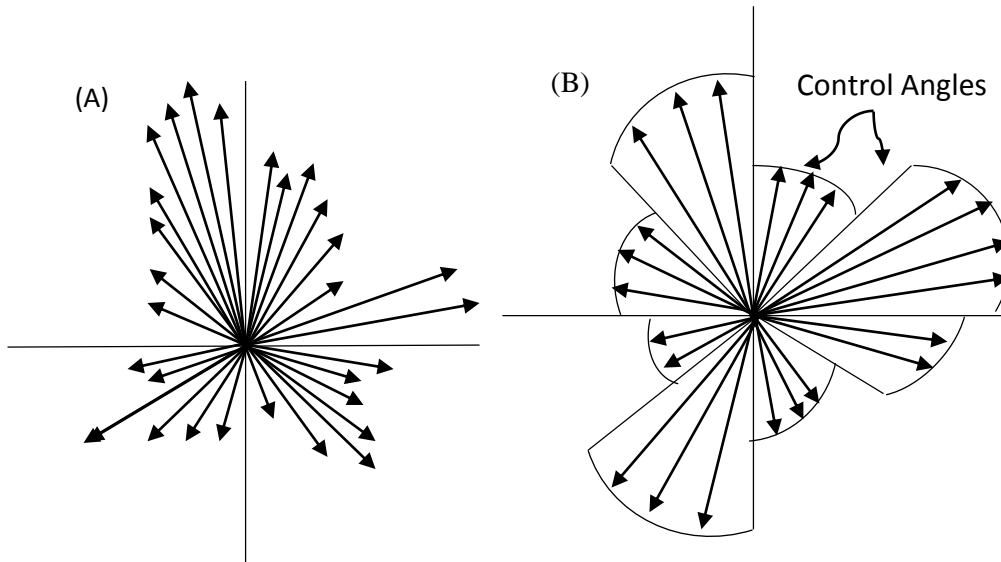
Figure 2.7   Intensity distribution A- real infinite directions   b- finite volume method

Both, the finite volume method, and the discrete ordinate method, divide the angular

space into a finite number of control angles. Nevertheless, both methods are

fundamentally different, in which unlike the finite volume method, the discrete ordinate method does not ensure energy conservation. This is a result of the finite differencing scheme.

The discrete ordinates method suffers from multiple drawbacks. For instance, the ray effect produced because due to angular discretization, and false scattering resulting due to spatial discretization. The finite volume method tries to address these problems.

The finite volume method starts by integrating the radiative heat transfer equation over a control volume and a control angle:

$$\int_v \int_\omega \frac{\partial I_\eta}{\partial s} \, dV \, d\omega = \int_v \int_w \left[\kappa_\eta I_b - \beta \, I_\eta + \frac{\sigma}{4\pi} \int_{4\pi} I_\eta(s_i) \, \Phi(\hat{s}_i.s) \, d\Omega \right] dV \, d\omega \qquad (2.55)$$

using the divergence theorem for the left-hand side:

$$\int_\omega \int_A I(s.n) \, dA d\omega = \int_v \int_w \left[\kappa_\eta I_b - \beta \, I_\eta + \frac{\sigma}{4\pi} \int_{4\pi} I_\eta(s_i) \, \Phi(\hat{s}_i.s) \, d\Omega \right] dV \, d\omega \qquad (2.56)$$

where A is the surface area of the control volume, V is the volume of a control volume, and ω is the solid angle associated with the direction of interest.

Chapter 3

3.1 Numerical algorithm

This chapter will provide the numerical solution for both, the P1 approximation, as well as the finite volume method, described in the preceding chapter. A solution for the energy equation will be provided as well.

3.1.1 P1 method

As concluded in the preceding chapter, the P1 approximation results in a coupled set of differential equations. The first equation describes the divergence of incident radiation in terms of radiative heat flux. The second equation describes the divergence of radiative heat flux in terms of incident radiation more specifically

$$\nabla . q = (1 - \omega)(4\pi I_b - G) \qquad (3.1)$$

$$\nabla G = (-3 - A_1 \, \omega \,) \, q \qquad (3.2)$$

which can also be written as

$$\nabla . q = \kappa_\lambda \, (4\pi I_{b\lambda} - G_\lambda) \qquad (3.3)$$

$$\nabla G_\lambda = -3 \, \beta_I \, q_\lambda \qquad (3.4)$$

where β_I is the anisotropic extinction coefficient expressed as

$$\beta_I = \beta - \frac{\sigma A_i}{3} \qquad (3.5)$$

and $I_{b\lambda}$ is the Planck function described previously as

$$I_{b\lambda}(\lambda, T) = \frac{2hc^2}{\lambda^5 \, (\exp\left[\frac{hc}{\lambda \, \sigma \, T}\right] - 1)} \qquad (3.6)$$

As obtained from Eq. 3.4, it is possible to substitute the value of $\frac{-1}{3\,\beta_I}\nabla\,G_\lambda$ for the heat

flux term (q_λ), in Eq. 3.3. The combined result provides an equation for the unknown

incident radiation, (G_λ), as follows

$$\nabla\cdot\frac{-1}{3\,\beta_I}\nabla\,G_\lambda \;=\; \kappa_\lambda\,(4\pi I_{b\lambda}-G_\lambda) \qquad (3.7)$$

Integrating Eq. 3.7 over a control volume, the following can be obtained

$$-\oint\frac{-1}{3\,\beta_I}\nabla\,G_\lambda.n\;dA \;=\; \int_V \kappa_\lambda\,(4\pi I_{b\lambda}-G_\lambda) \qquad (3.8)$$

A cell centered finite volume discretization is used to solve the previous equation.

For a one-dimensional geometry in Cartesian plane this result in

$$\left[\frac{1}{3\beta_I}\left(\frac{\partial G_\lambda}{\partial x}\right)_r A_r\right] - \left[\frac{1}{3\beta_I}\left(\frac{\partial G_\lambda}{\partial x}\right)_L A_L\right] = -\kappa_\lambda\,(4\pi I_{b\lambda}-G_\lambda)\,\Delta V \qquad (3.9)$$

where the first term represents the flux from the right-hand side surface, the second

term represents the flux from the left-hand side surface, and ΔV is the volume of the

control element. It is possible to represent Eq. 3.9 in a discrete format for the i_{th} cell as

$$\left(G_{\lambda,i+1}-G_{\lambda,i}\right)F_+ - \left(G_{\lambda,i}-G_{\lambda,i-1}\right)F_- = -3\kappa_{\lambda,i}\left(4\pi I_{b\lambda,i}-G_{\lambda,i}\right)\Delta V_i \qquad (3.10)$$

where

$$F_- = \frac{2\,A_{i-\frac{1}{2}}}{\beta_{I\lambda-}\,(\Delta x_i + \Delta x_{i-1})}$$

$$F_+ = \frac{2\,A_{i+\frac{1}{2}}}{\beta_{I\lambda+}\,(\Delta x_{i+1} + \Delta x_i)}$$

$$\beta_{I\lambda-} = \beta_{I\lambda,\ i-1} + \left(\beta_{I\lambda,\ i} - \beta_{I\lambda,\ i-1}\right)\frac{\Delta x_{i-1}}{\Delta x_{i-1} + \Delta x_i}$$

$$\beta_{I\lambda+} = \beta_{I\lambda,\ i+1} + \left(\beta_{I\lambda,\ i+1} - \beta_{I\lambda,\ i}\right)\frac{\Delta x_{i+1}}{\Delta x_{i+1} + \Delta x_i}$$

The final discretized equation can be presented as

$$b_i\ G_{\lambda i} + a_i\ G_{\lambda,i-1} + c_i\ G_{\lambda,i+1} = d_i \qquad (3.11)$$

where

$$a_i = F_-$$

$$b_i = -12\ \kappa_\lambda\ I_{b\lambda}\ \Delta V$$

$$c_i = F_+$$

$$d_i = 3\kappa_{\lambda i}\ \Delta V_i - F_- + F_+$$

In 1D this set of linear equations can be solved using a tridiagonal matrix solver for the unknown incident radiation, G. Other radiative parameters can be solved for afterwards.

3.1.2 Finite volume method

A two-dimensional domain is used to describe the method. The extension to one- and three-dimensional domains is straight forward. The finite volume method subdivides the angular domain into control angles, and the spatial domain into control volumes as subsequently explained.

3.1.2.1 Control volumes

The spatial domain is subdivided as shown in Fig. 3.1.
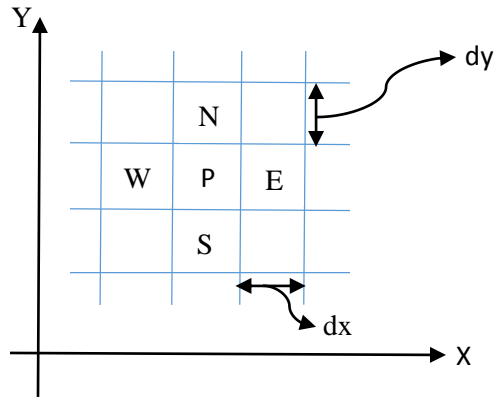
Figure 3.1 two dimensional spatial domain

This method works for both structured and unstructured meshes. However, only structured mesh will be used throughout this study.

The spatial domain is divided into $N_x \times N_y$ control volumes with equal spacing as shown in Fig 3.1.

$$\Delta X = \frac{L_x}{N_x}$$

and

$$\Delta Y = \frac{L_y}{N_y}$$

3.1.2.2 Control angles

Similar to the spatial domain, angular space is discretized by dividing the 4π solid angle into control angles. Structured and unstructured meshes can be used. However, only the structured mesh will be considered in this study as shown in Fig. 3.2.
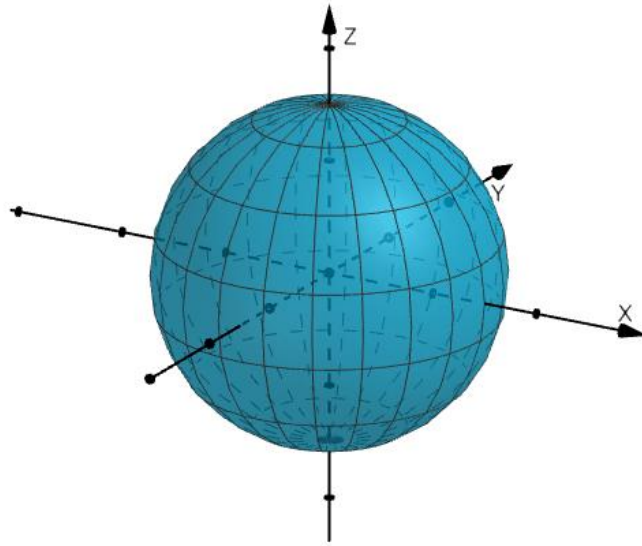
The angular domain is subdivided into $N_\theta \times N_\phi$ control angles, with equal spacing in

the polar and azimuthal angles more specifically

$$\Delta\theta = \frac{2\pi}{N_\theta}$$

$$\Delta\phi = \frac{4\pi}{N\phi}$$

3.1.2.3 Numerical algorithm

Reconsidering the radiative transfer equation

$$\frac{\partial I_\eta}{\partial s} = \kappa_\eta I_b - \beta\, I_\eta + \frac{\sigma}{4\pi} \int_{4\pi} I_\eta(s_i)\, \phi(\hat{s}_i.s)\, d\Omega$$

which can be rewritten as:

$$\frac{dI(r,s)}{ds} = -\beta(r)\, I(r,s) + S(r,s) \qquad (3.12)$$

where $\beta = \sigma + \kappa$ is the extinction coefficient, and $S(r,s)$ is a source term defined as follows

$$S(r,s) = \kappa \, I_b + \frac{\sigma}{4\pi} \int_{4\pi} I(r,\hat{s}) \, \Phi(\hat{s}',\hat{s}) \, d\Omega$$

Integrating the transfer equation over the control volume and control angle results in

$$\int_{\Delta\Omega} \int_{\Delta V} \frac{dI'}{ds} \, dV \, d\Omega \;=\; \int_{\Delta\Omega} \int_{\Delta V} (-\beta \, I' + s') \, dV \, d\Omega \qquad (3.13)$$

Using the divergence theorem, Eq. 3.13 can be presented as

$$\int_{\Delta\Omega} \int_{\Delta A} I(r,s) \, (\hat{s}.n) \, dA \, d\Omega = \int_{\Delta\Omega} \int_{\Delta V} (-\beta \, I' + s') \, dV \, d\Omega \qquad (3.14)$$

where $\hat{n}$ represents the normal unit vector to the boundary surface. The left-hand side of Eq. 3.14 represents the inflow and outflow of radiation energy across the control volume surface.

Equation 3.14 can be further simplified as follows:

$$\sum_{i=nb} I'_i A_i \int_{\Delta\Omega} \hat{s}'.n_i \, d\Omega \;=\; (-\beta \, I' + S') \, \Delta V \, \Delta\Omega' \qquad (3.15)$$

where

$$S' = \kappa \, I_b + \frac{\sigma}{4\pi} \sum_{l'=1} I' \, \Phi^{l'l} \, \Delta\Omega$$

In this equation, Φ is the scattering phase function from direction l' to direction l, which equals one for isotropic scattering.

Solving Eq. 3.15 for the angular grid shown in Fig. 3.2, the following equation is obtained

$$A_e D_{ce} I_e + A_w D_{cw} I_w + A_n D_{cn} I_w + A_s D_{cs} I_s = \left(-\beta I'_p + S'_p\right) \Delta V_p \, \Delta\Omega \qquad (3.16)$$

where

$$D'_{ce} = \int_{\Delta\Omega} \hat{s}.e_x \, d\Omega \qquad\qquad D'_{cn} = \int_{\Delta\Omega} \hat{s}.e_y \, d\Omega$$

$$D'_{cw} = -D'_{ce} \qquad\qquad D'_{cs} = -D'_{cn}$$

$$\Delta\Omega = \int_{\Delta\Omega} d\Omega$$

$$S'_p = \kappa_p I_b + \frac{\sigma}{4\pi} \sum_{l'=1} I_p^{l'} \phi^{l'l} \, \Delta\Omega$$

$$A_e = A_w = \Delta y$$

$$A_n = A_s = \Delta x$$

$$\Delta V = \Delta y \, \Delta x$$

The directional cosines D'_{ci} are evaluated analytically before proceeding with the numerical calculations. The evaluation of directional cosines requires the mathematical formulation of the direction vector, as well as the solid angle.

The direction vector $\hat{s}$ in Cartesian coordinates is defined as

$$s = s_x e_x + s_y e_y + s_z e_z \qquad (3.17)$$

Or, more specifically

$$s = \sin\theta \, \cos\phi \, e_x + \sin\theta \, \sin\phi \, e_y + \cos\theta \, e_z \qquad (3.18)$$

The solid angle is defined as

$$d\Omega = sin\theta \; d\theta \; d\phi \qquad (3.19)$$

The directional cosines in the x-direction for a two-dimensional domain are evaluated as

$$D'_{ce} = \int_{\Delta\Omega} \hat{s}.e_x \; d\Omega$$

$$D'_{ce} = \int_{\Delta\Omega} sin\theta \; cos\phi \; d\Omega$$

$$D'_{ce} = \int_{\Delta\phi} \int_{\Delta\theta} sin\theta \; cos\phi \; (sin\theta \; d\theta \; d\phi)$$

$$D'_{ce} = \int_{\Delta\phi} \int_{\Delta\theta} sin^2\theta \; cos\phi \; d\theta d\phi$$

$$D_{ce} = -\frac{1}{4}[2(\theta_+ - \theta_-) - (sin(2\theta_+) - sin(2\theta_-)) \times [sin(\phi_+) - \; sin(\phi_-)]$$

and in the y-direction as

$$D'_{cn} = \int_{\Delta\Omega} \hat{s}.e_y \; d\Omega$$

$$D'_{cn} = \int_{\Delta\Omega} sin\theta \; sin\phi \; d\Omega$$

$$D'_{cn} = \int_{\Delta\phi} \int_{\Delta\theta} sin\theta \; sin\phi \; (sin\theta \; d\theta \; d\phi)$$

$$D'_{cn} = \int_{\Delta\phi} \int_{\Delta\theta} sin^2\theta \; sin\phi \; d\theta d\phi$$

$$D_{cn} = -\frac{1}{4}[2(\theta_+ - \theta_-) - (sin(2\theta_+) - sin(2\theta_-)) \times [cos(\phi_+) - \; cos(\phi_-)]$$

44

The directional cosines should be evaluated for each solid angle bounded

between $\theta_+, \theta_-, \phi_+, and\ \phi_-$, as shown in Fig. 3.3.
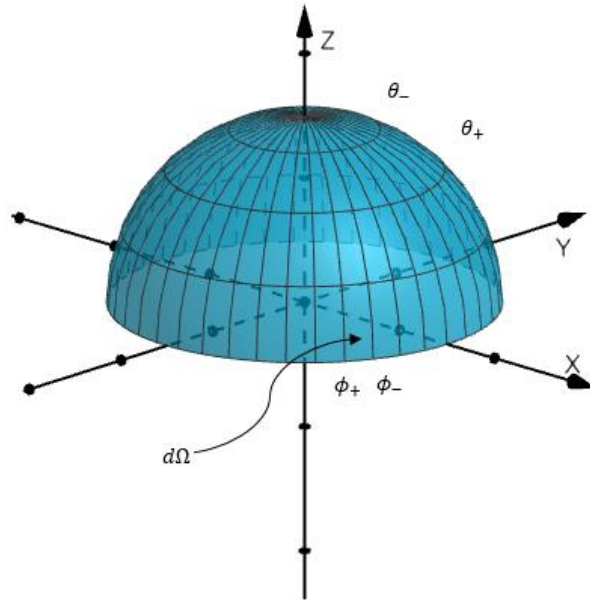
Figure 3.3 Control angle (generated using GeoGebra)

The left-hand side of Eq. 3.16 describes the intensities at the faces of control

volumes. Since the finite volume method is a cell centered method, where the solution

is obtained for the intensities at the cell centers, there must be a relation that relates

both intensities, to proceed with the calculation.

Most often, a linear relation is provided to relate the nodal and face intensities in the

form of:

$$I_{pi} = \gamma_y\ I_{Ni} + \left(1 - \gamma_y\right) I_{si} = \gamma_x\ I_{Ei} + (1 - \gamma_x)\ I_{wi} \qquad (3.20)$$

where γ is a constant number varying between $\frac{1}{2}$ and 1.

45

There are multiple schemes based on Eq. 3.20, such as the diamond scheme, the exponential scheme, and the step scheme.

The diamond scheme is one of the popular differencing schemes. The relation can be obtained easily by substituting a value of 0.5 for γ in Eq. 3.20. However, Carlson [27] showed that this scheme may lead to negative intensities. This is physically not possible. Fiveland [33] showed that if the dimensions are kept within a certain value, the error can be minimized.

The exponential scheme is considered more accurate, especially for one-dimensional problems. This scheme was used by Raithby et al [51], and it is possible to obtain the relation by substituting the value of γ with:

$$\gamma = \frac{1}{1 - e^{\tau_s}} - \frac{1}{\tau_s} \qquad \text{where s is the spatial direction (e. g. } x, y)$$

$$\tau = \beta \frac{\Delta s}{\zeta} \qquad \zeta \text{ is the directional cosine}$$

This scheme is the simplest scheme. It can be obtained by simply substituting $\gamma = 1$ in Eq. 3.20. This scheme is considered as the only scheme that does not produce negative intensities, and is the one used in the present work.

After applying the step scheme, Eq. 3.16 reduces to

$$a_p^l \, I_p^l = a_w^l I_w^l + a_s^l \, I_s^l + b^l \qquad (3.21)$$

where

$$a_w = A_w \, |D_{cw}| \qquad a_s^l = A_s |D_{cs}|$$

46

$$a^l p = A_e \, D^l_{ce} + \; A_n \, D_{cn} + \beta \, \Delta V \, \Delta \Omega$$

$$b^l = S^l_p \, \Delta V_p \, \Delta \Omega$$

The boundary condition is the only missing part needed to make the solution possible. The boundary condition used in this study describes the radiant intensity leaving an opaque diffuse reflecting surface, as presented in Eq. 3.22.

$$I(r,s) = \epsilon \, I_b + \frac{\rho}{\pi} \int_{s.n<0} I(r,\hat{s}) \; |s.n| \, d\Omega \qquad (3.22)$$

where ϵ is the emissivity, ρ is the reflectivity ($\rho = 1 - \epsilon$), and I_b is the blackbody emission.

The previous relation describes the intensity towards the medium as a function of the emitted wall radiation. It is a function of the wall temperature, as well as the reflected radiation.

3.1.2.4 Solution procedure

The solution procedure shown in Fig. 3.4 constitutes of four steps. When combined, the four steps form a one cycle "iteration".

Starting from the bottom left corner with the defined intensities at the bottom and left surfaces, the solution marches toward the top right corner, calculating the intensities in the directions associated with the quadrant, as shown in Fig. 3.4 A. This step calculates the incoming intensities toward the top and right surfaces. Aiming for the boundary condition, it is possible to calculate the intensity leaving those surfaces.

The second step starts from the bottom right corner, calculating the intensities associated with the quadrant, shown in Fig. 3.4 B. By doing so, the incoming intensities on the top and left surfaces are provided. Using the boundary condition, and after updating the values for the top surface intensities, it is possible to calculate the intensities leaving the top and left surfaces.

The third step starts from the top left corner, and marches toward the bottom right corner, providing the directional intensities associated with the quadrant shown in Fig. 3.4 C. After updating the incoming intensities on the bottom and right surfaces, and using boundary conditions, it is possible to calculate the intensities leaving those surfaces.

The last step is done to calculate the intensities in the directions shown in Fig. 3.4 D. This is done by starting at the top right corner and marching towards the bottom left corner. After updating the intensities on the bottom and left surfaces, it is possible to find the intensities leaving those surfaces by aiming for the boundary condition.

The four steps are required to find the directional intensities within the full solid angle range. The four steps are considered as one cycle, or iteration. The steps are repeated until convergence is achieved.
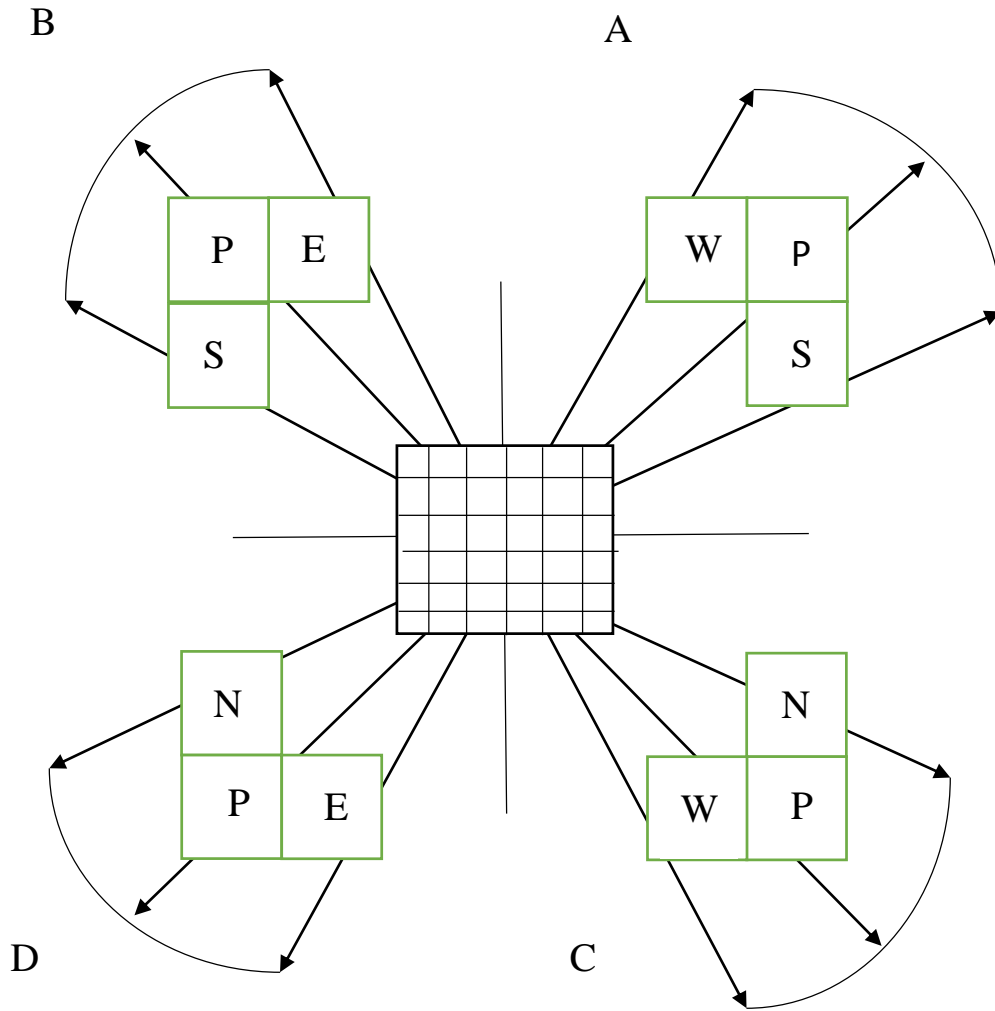
Figure 3.4 Solution procedure for the finite volume method

3.2 Energy equation

The radiation solver is coupled to an energy equation solver in a one dimensional space. The one dimensional energy equation can be presented as

$$\rho \, C_p \, \frac{\partial T}{\partial t} = \left[\frac{\partial}{\partial x} \, K \, \frac{\partial T}{\partial x} - S \, \right] \qquad (3.23)$$

where the source term S represents the divergence of the radiative heat flux, defined as

$$S = \frac{\partial q}{\partial x} = \kappa \, (4\pi I_b - G_\lambda) \qquad (3.24)$$

49

This equation can be solved using one of the radiative heat transfer equation (RTE) solvers. For this work both the FVM and the P1 approximation will be used.

A finite volume discretization is used to obtain the numerical solution for the energy equation, with cell centered nodes and explicit scheme, as follows:

$$\int_t \int_{\Delta V} \rho \, C_p \frac{\partial T}{\partial t} \, dt \, dv = \int_t \int_{\Delta V} \left[\frac{\partial}{\partial x} K \frac{\partial T}{\partial x} - S \right] dt \, dv \qquad (3.25)$$

Integrating the terms in Eq. 3.25 will result in the following:

$$\int_t \int_{\Delta V} \rho \, C_p \frac{\partial T}{\partial t} \, dt \, dv = \rho \, C_p \left(T^{i+1} - T^i \right) \Delta v \qquad (3.26)$$

$$\int_t \int_{\Delta V} \left[\frac{\partial}{\partial x} K \frac{\partial T}{\partial x} - S \right] dt \, dv$$

$$= \left[K_E \frac{T_{i+1} - T_i}{\Delta x} \right]_E \Delta A \, \Delta t - \left[K_W \frac{T_i - T_{i-1}}{\Delta x} \right]_W \Delta A \, \Delta t$$

$$- S \, \Delta t \, \Delta v \qquad (3.27)$$

The divergence theorem is applied to obtain the convective terms in Eq. 3.27 described as

$$\int_{\Delta v} \nabla . \, K \, \nabla T = \oiint_{\Delta A} K \, \nabla \mathrm{T} . \, \mathrm{n} \, \mathrm{ds} \qquad (3.28)$$

3.3 Verification

As stated previously, except for simplified cases, it is nearly impossible to obtain exact solutions for the radiative transfer equation. The aim of this section is to ensure that the different codes used in this work produce the exact analytical solutions for different simplified conduction and radiation cases.

3.3.1 Energy Equation
A- Transient conduction with Dirichlet boundary condition

This problem describes a 1D slab, with an imposed constant surface temperature boundary condition on one side, and with constant properties. The governing equation, as well as the boundary and initial conditions are

$$\rho \, C_p \frac{\partial T}{\partial t} = k \frac{\partial^2 T}{\partial x^2} \qquad (3.34)$$

$$T(x, t = 0) = T_0 \qquad (3.34)$$

$$T(x = l, t) = T_w \qquad (3.35)$$

$$-k \frac{\partial T}{\partial x}(x = 0, t) = 0 \qquad (3.36)$$

The analytical solution for this problem was published by Bird [52] and it is expressed as

$$\frac{T_w - T}{T_w - T_0} = 2 \sum_{n=0}^{\infty} \frac{(-1)^n}{\left(n + \frac{1}{2}\right)\pi} e^{-\left(n + \frac{1}{2}\right)^2 \pi^2 \frac{\alpha t}{l^2}} \cos\left(n + \frac{1}{2}\right)\frac{\pi x}{l}$$

The boundary conditions and the parameters for this problem are listed in Table 1.

Table 1: Conduction with direchlet boundary conditions case parameters

Parameter	Value
T_0	300 K
T_w	500 K
l	0.01 m
ρ	8000 kg/m³
C_p	500 J/Kg.K
K	10 w/m.K

Analytical and numerical solutions were compared for times 4, and 40 s as shown in Fig. 3.5. The relative error was calculated and shown in Fig. 3.6.

Figure 3.5 Conduction with Direchlet boundary conditions case results

Figure 3.6 Conduction with Direchlet boundary conditions relative error

As clear from Fig. 3.5 and Fig. 3.6, the predicted numerical solution matches well with the analytical solution, and produced an error less than 0.37% for time 40 s and less than 0.004 for time 4 s.

B- Transient conduction with Neumann boundary condition

This problem describes the transient conductive heat transfer in a 1-dimensional slab, with a specified constant heat flux on one side. The governing equation, as well as the initial and boundary conditions, are described as follows:

$$\rho \, C_p \frac{\partial T}{\partial t} = k \frac{\partial^2 T}{\partial x^2} \qquad (3.37)$$

$$T(x, t = 0) = T_0 \qquad (3.38)$$

$$-k \frac{\partial T}{\partial x}(x = l, t) = 0 \qquad (3.39)$$

53

$$-k\frac{\partial T}{\partial x}(x = 0, t) = q'' \qquad (3.40)$$

The analytical solution for this problem was published by Bird [52], and is expressed

as

$$\frac{T - T_0}{q''l/K} = \frac{\alpha t}{l^2} + \frac{1}{3} - \frac{x}{l} + \frac{1}{2}\left(\frac{x}{l}\right)^2 - \frac{2}{\pi^2}\sum_{n=1}^{\infty}\frac{1}{n^2}\,e^{-\frac{n^2\pi^2\alpha t}{l^2}}\cos\left(\frac{n\pi x}{l}\right)$$

The boundary conditions and the parameters for this case are listed in Table 2.

Table 2: Conduction with Neumann boundary conditions case parameters

Parameter	Value
T_0	300 K
q''	7.5×10^5 K
l	0.01 m
α	2.5×10^{-6} m²/s

Analytical and numerical solutions are compared for times 4, and 40 s as shown in

Fig. 3.7. The relative error is shown in Fig. 3.8.
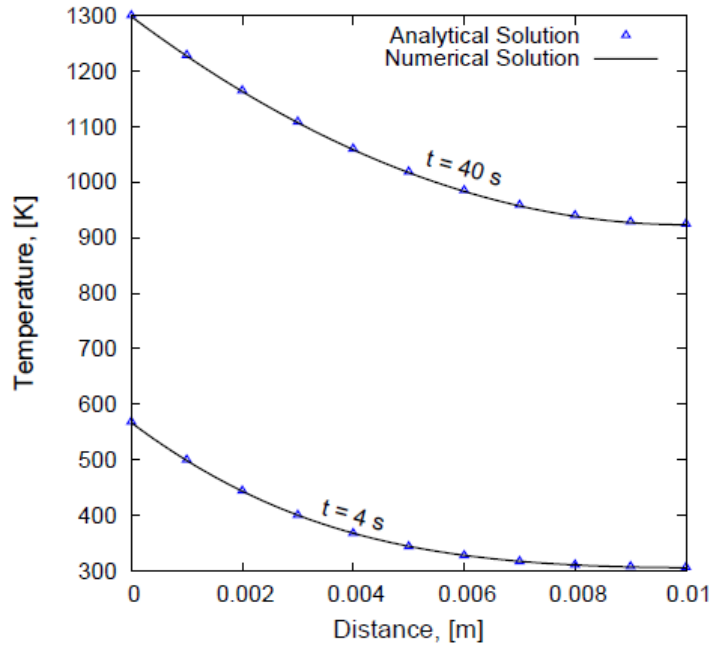
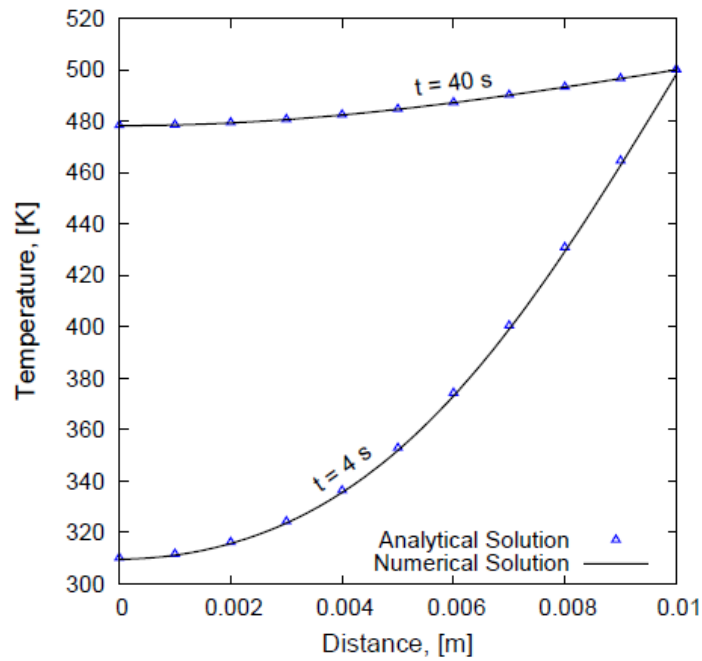*Figure 3.7 Conduction with Nuemann boundary conditions case results*

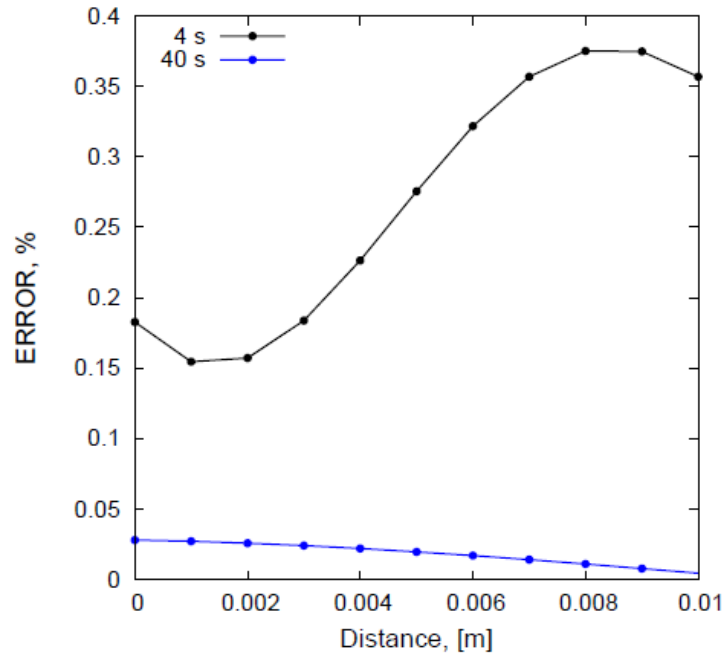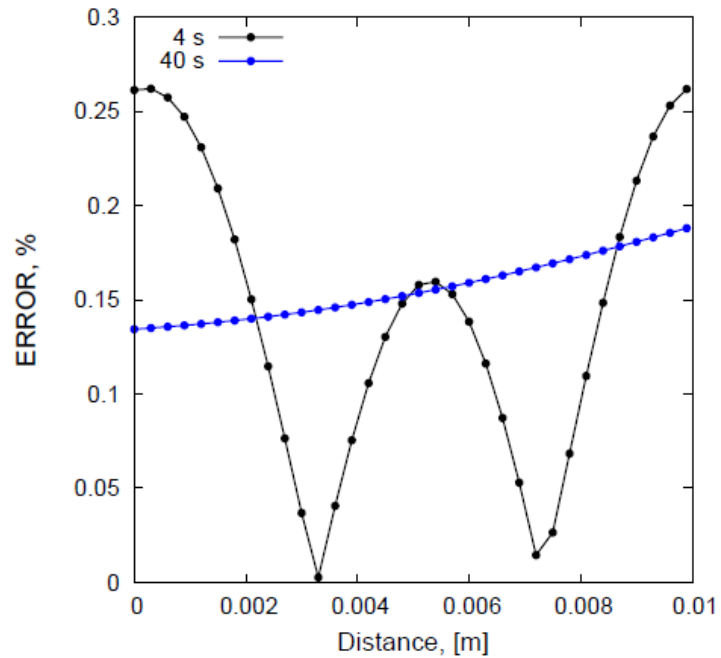*Figure 3.8 Conduction with Neumann boundary conditions relative error*

As clear from Fig. 3.7 and Fig. 3.8, there was a negligible error between the analytical and numerical solutions where the error did not exceed 0.25% for 4s and 0.2 % for 40s.

C- Transient conduction with periodic heat flux boundary condition

This problem is similar to the previous one, except that the applied heat flux is periodic, in the way it varies with time. The heat flux is expressed as:

$$q'' = q_0'' \cos(\omega\, t) \qquad\qquad (3.41)$$

The governing equation, initial condition, and boundary conditions are expressed as follows:

$$\rho\, C_p \frac{\partial T}{\partial t} = k \frac{\partial^2 T}{\partial x^2} \qquad\qquad (3.42)$$

$$T(x, t = 0) = T_0 \qquad\qquad (3.43)$$

$$-k \frac{\partial T}{\partial x}(x = l, t) = 0 \qquad\qquad (3.44)$$

$$-k \frac{\partial T}{\partial x}(x = 0, t) = q'' \qquad\qquad (3.45)$$

The analytical solution for this problem was published by Bird [52], and it is expressed as

$$T - T_0 = \frac{q_0}{k} \sqrt{\frac{\alpha}{\omega}}\; e^{-x\sqrt{\frac{\omega}{2\alpha}}} \cos\left(\omega\, t - \sqrt{\frac{\omega}{2\alpha}}\, x - \frac{\pi}{4}\right)$$

The boundary and the parameters for this case are listed in Table 3.

Table 3: Conduction with periodic heat flux test parameters

Parameter	Value
T_0	300 K
q_0''	7.5×10^5 K
l	0.01 m
ρ	8000 kg/m³
C_p	500 J/Kg.K
K	10 W/m.K

Results are compared against pblished analytical soultions as shown in Fig. 3.9 and the relative error is shown in Fig. 3.10.
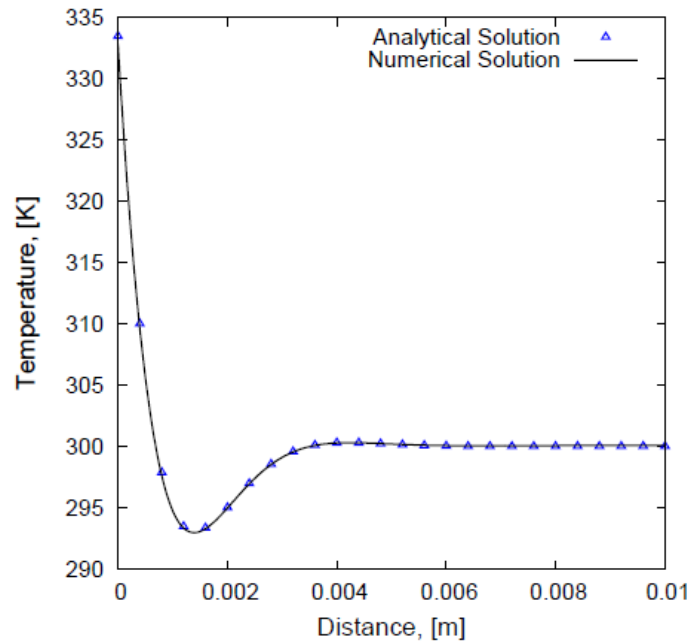
Figure 3.9 Conduction with time varying heat flux case results
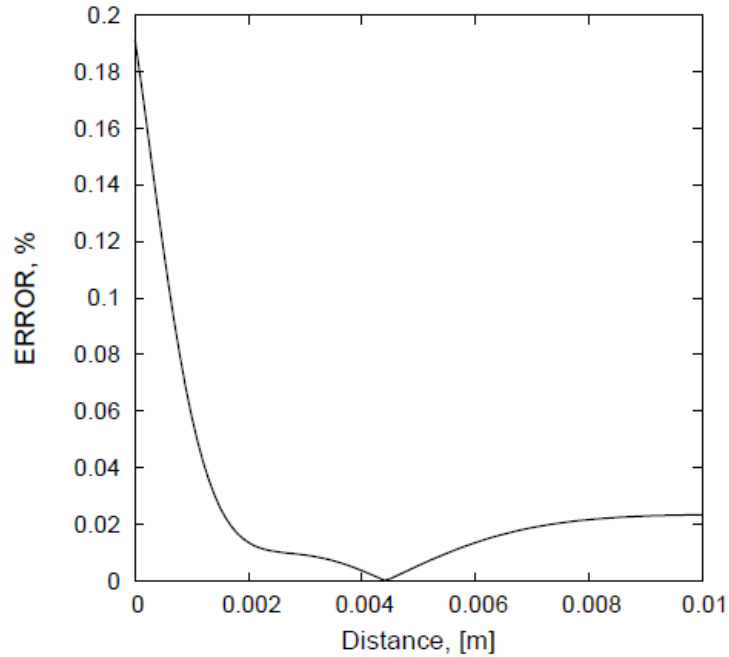
Figure 3.10 conduction with time varying heat flux boundary condition relative error

Figures 3.9 and 3.10 shows that the analytical and numerical solutions agree with a relative error less than 0.2%.

3.3.2 Radiation

For a one-dimensional space, both, the finite volume and P1 approximation solvers, will be verified against analytical solutions.

The dimensionless parameters used in the different cases are defined as follows:

- Non-dimensional distance:

$$x^* = X/L_x \qquad \text{and} \qquad y^* = Y/L_y$$

- Non-dimensional heat transfer flux: $q^* = \dfrac{q}{\sigma(T_h^4 - T_c^4)}$

- Optical thickness: $\kappa^* = \beta\, L_y$

A- One dimensional purely isotropically scattering medium

The first case describes the radiative heat flux in a purely scattering medium, enclosed between two black surfaces, with isotropic scattering for a range of optical thicknesses.

Test parameters for this problem are provided in Table 4.

Table 4: Purely isotropically scattering medium case parameters

Parameter	Value
T_{top}	0 K
T_{medium}	0 K
T_{bottom}	100 K
σ	1 m^{-1}
κ	0 m^{-1}
Ω	1
κ^*	σL

Problem schematic for this test case is provided in Fig. 3.11.

$$T_{top} = 0 \, , \epsilon = 1$$

$$T_{medium} = 0 \text{ K}$$
$$\Omega = 1$$

$$T_{bottom} = 100, \epsilon = 1$$
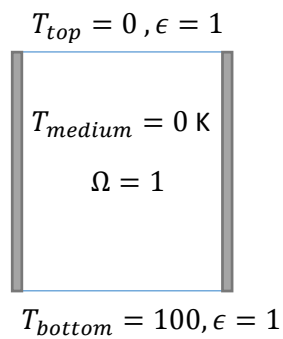
Figure 3.11 Purely isotropically scattering medium case schematic
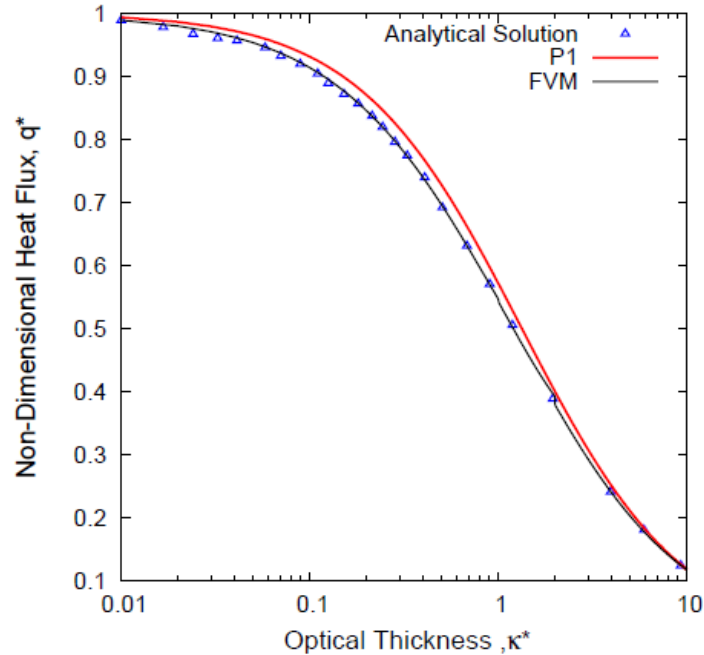
Figure 3.12 Non dimensional heat flux on a hot bottom surface for purely isotropically medium

Figure 3.12 compares the results obtained using the P1 approximation and the FVM, against the analytical solutions published by Heaslet [54] for a wide range of optical thicknesses. It was noted that for the optical thickness shown in Fig. 3.12, the relative error for the FVM did not exceed 1%, while the P1 approximation did reach 4.5%. These results are consistant with the behaviour of both methods since the FVM performs better in the optically thin medium, unlike the P1 approximation which performs better within an optically thick medium.

For optically thick medium, the finite volume solution consumed a lot of time, and the solver did not converge to a solution. On the contrary, the P1 approximation was able to perform the calculation without consuming too much time.

Figure 3.13 shows the obtained results for the P1 approximation within the optical

thick region for the same case described earlier.
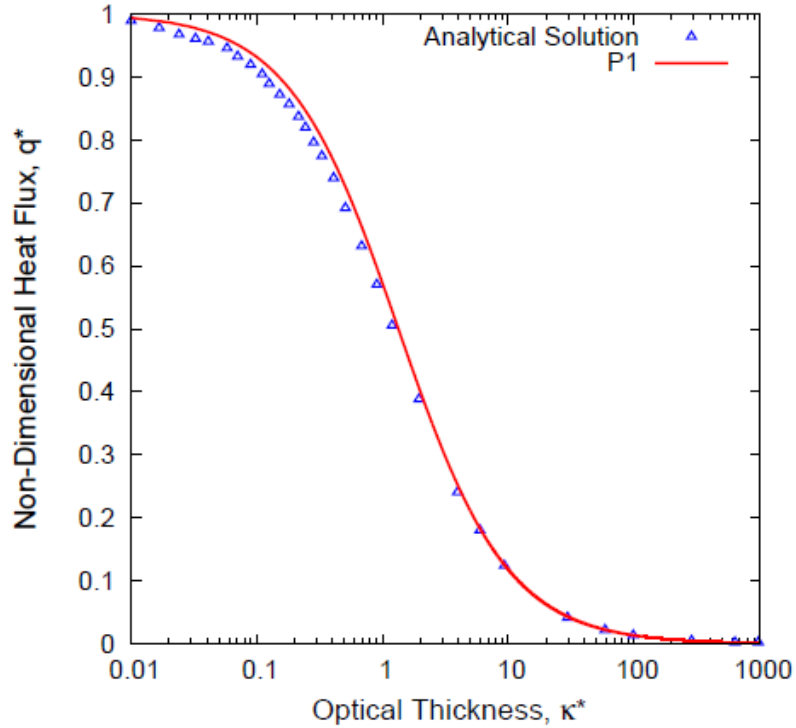
Figure 3.13 Non dimensional heat flux on the bottom hot surface using the P1 approximation

It is clear from Fig. 3.13 that the P1 approximation as discussed above performs

better within the optical thick range. As the optical thickness increases the predicted

solution agrees better with the analytical solution.

B- One dimensional purely absorbing medium
This case describes the radiative heat flux in an emitting-absorbing medium

contained between black surfaces.

The test parameters for this test case are listed in Table 5.

Table 5: Purely absorbing medium case parameters

Parameter	Value
T_{top}	100 K
T_{medium}	50 K
T_{bottom}	100 K
σ	0 m^{-1}
κ	1 m^{-1}
Ω	0

The schematic for this test case is provided in Fig. 3.14.

$$T_{top} = 100 \, , \epsilon = 1$$

$$T_{medium} = 50 \text{ K}$$

$$\Omega = 1$$

$$T_{bottom} = 100, \epsilon = 1$$
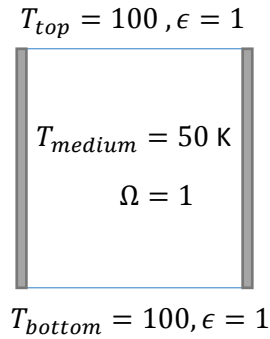
Figure 3.14 Purely absorbing medium case schematic

Figure 3.15 compares both results, obtained using the finite volume method and the P1 approximation, against the analytical solution published by Modest [15]. Figure 3.15 describes the radiative heat flux on the hot bottom surface for a range of optical thicknesses.

It is clear from Fig. 3.15 that the finite volume method provides a better approximation to the analytical solution since the P1 approximation over predicts the solution within the shown optical thickness range.
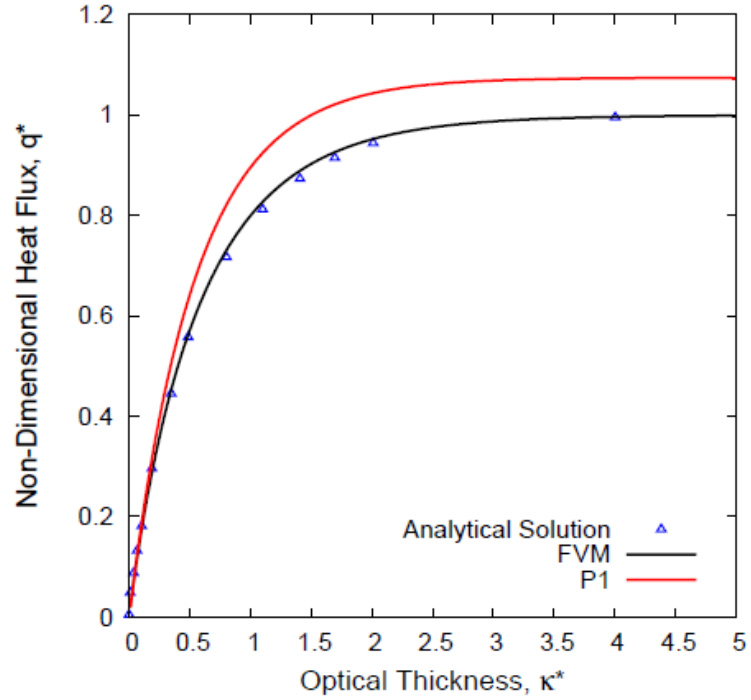
Figure 3.15 Non dimensional heat flux on the bottom hot surface

C- Two dimensional purely isotropically scattering square enclosure

This case describes the radiative heat flux in a square enclosure with black surfaces

and isotropic scattering.

The parameters for this test case are provided in Table 6.

Table 6: Purely isotropically scattering 2D medium case parameters

Parameter	Value
$T_{top} = T_{left} = T_{right}$	0 K
T_{medium}	0 K
T_{bottom}	100 K
σ	1 m^{-1}
κ	0 m^{-1}
Ω	1
$L_x = L_y$	1

The schematic for this test case is provided in Fig. 3.16.

$$T_{top} = 0, \epsilon = 1$$

$T_{left} = 0, \epsilon$

$\Omega = 1$

$\Phi = 1$

$T_{right} = 0, \epsilon$

$$T_{bottom} = 100, \epsilon = 1$$
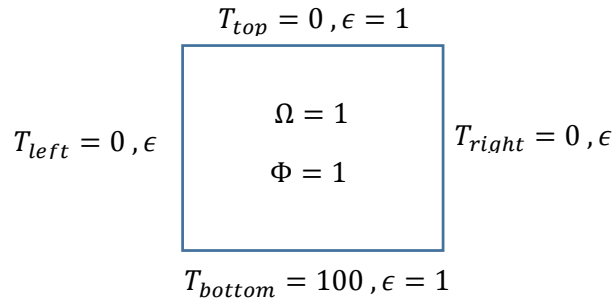
Figure 3.16 Purely isotropically scattering 2D medium schematic
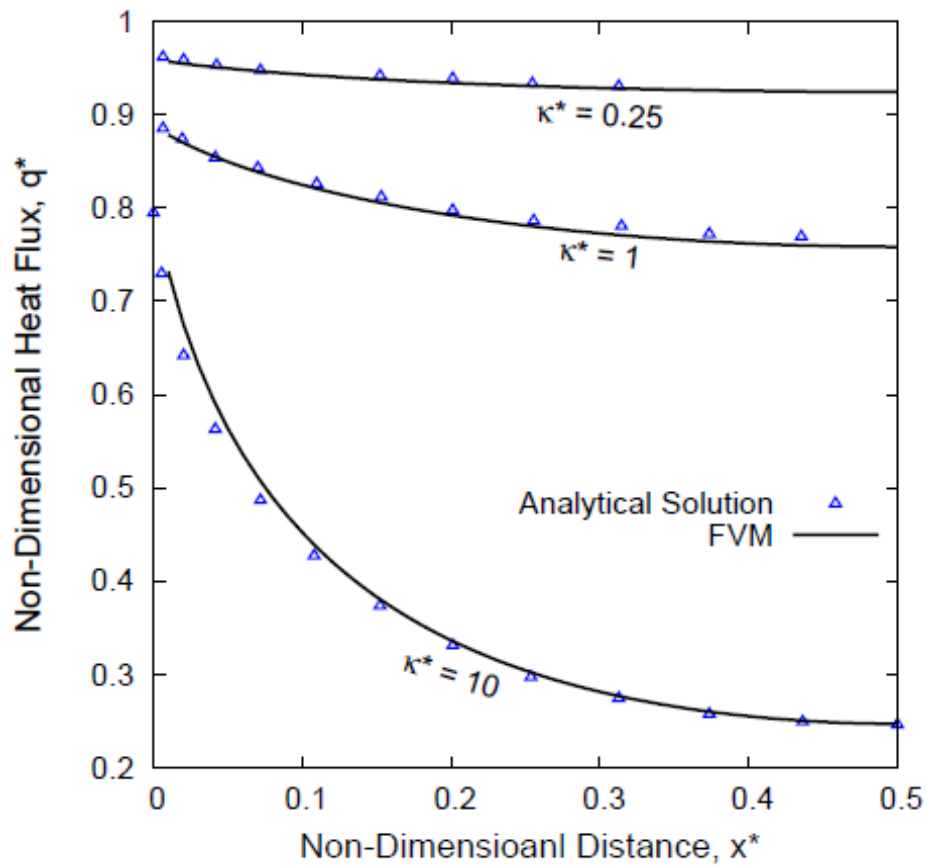
Figure 3.17 Non dimensional heat flux on a bottom hot surface of a 2D isotropically scattering medium for multiple optical thicknesses

Figure 3.17 present the radiative heat flux on a hot surface for a two dimensional

isotropically scattering enclosure for three optical thicknesses (0.25, 1, and 10) on the

bottom hot surface along half of the domain. The results are compared to the analytical

solutions obtained by Crosbie [55].

Figure 3.17 shows that the finite volume method approximates the analytical solution

of the problem with accuracy, for multiple optical thicknesses. It was noted that as the

optical thickness increase, the convergence rate decreases.

D- Two dimensional purely scattering medium in a rectangular enclosure

This case describes the radiative heat flux in a rectangular enclosure with black

surfaces and isotropic scattering. This case aims to describe the effect of the aspect ratio

on the results.

The test parameters are listed in Table 7.

Table 7: purely scattering 2D rectangular enclosure test parameters

Parameter	Value
$T_{top} = T_{left} = T_{right}$	0 K
T_{medium}	0 K
T_{bottom}	100 K
κ	0 m^{-1}
Ω	1
κ^*	$\sigma L_y = 1$

The schematic for this test case is shown in Fig. 3.18.
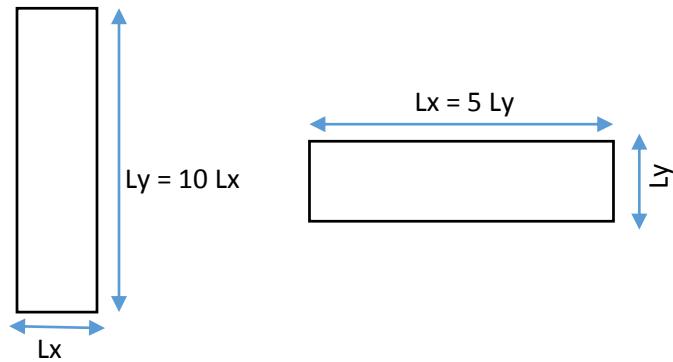
Figure 3.18: purely scattering 2D rectangular enclosure case schematic; Aspect ratio = 10 (left), Aspect ratio = 0.2 (Right)
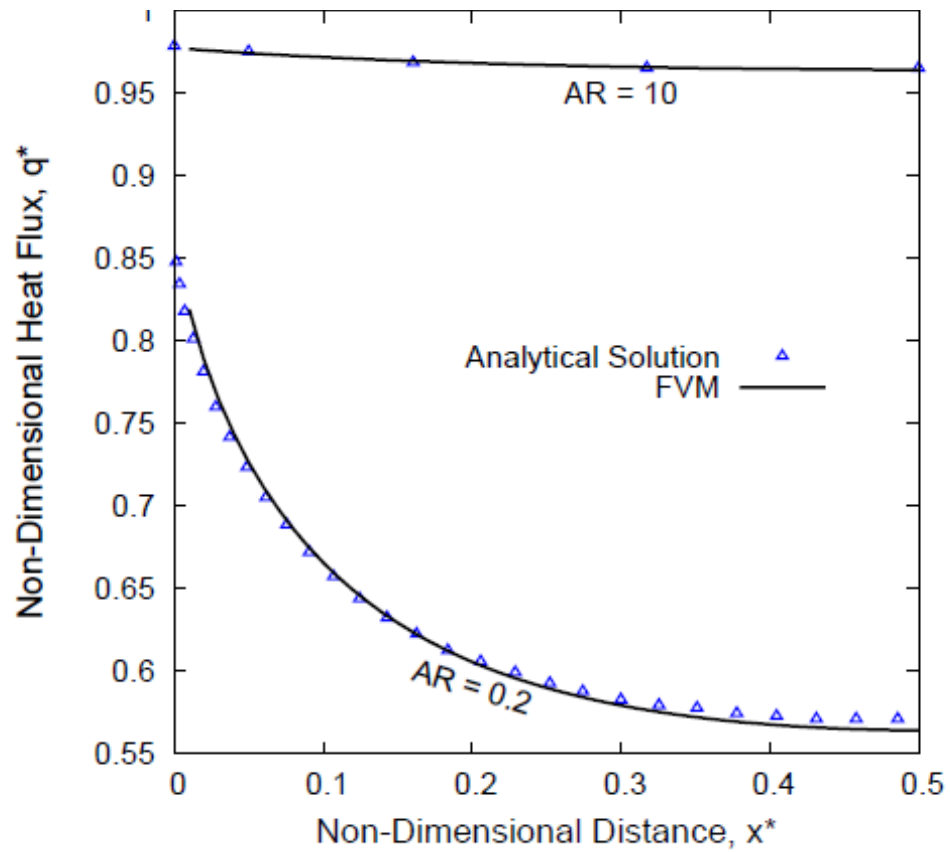
Figure 3.19 non dimensional heat flux along a hot surface of an isotropically scattering rectangular enclosure for two aspet ratios

As shown in Fig. 3.19, the finite volume method performs well for non-square

geometries, where the approximated the analytical solutions for different aspect ratios.

The exact solutions for this problem were published by Crosbie et al [55].

E- Two dimensional absorbing-scattering medium

Previous cases dealt with each one of the properties independently. On the contrary,

this case studies the radiative heat flux in an absorbing-scattering medium enclosed

between black surfaces, with isotropic scattering for two scattering albedos.

The Test parameters for this case are listed in Table 8.

Table 8: Absorbing-isotropically scattering 2D enclosure case parameters

Parameter	Value
$T_{top} = T_{left} = T_{right}$	0 K
T_{medium}	0 K
T_{bottom}	100 K
$L_x = L_y$	1
κ^*	$\beta\, L$

The problem schematic for this test case is shown in Fig. 3.20.

$$T_c = 0\,,\epsilon = 1$$

$$T_c = 0\,,\epsilon = 1 \qquad \Phi = 1 \qquad T_c = 0\,,\epsilon = 1$$

$$T_H = 100\,,\epsilon = 1$$
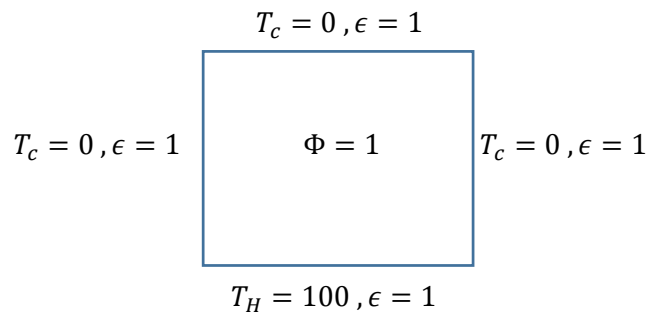
Figure 3.20 Absorbing-isotropically scattering 2D enclosure case schematic

67
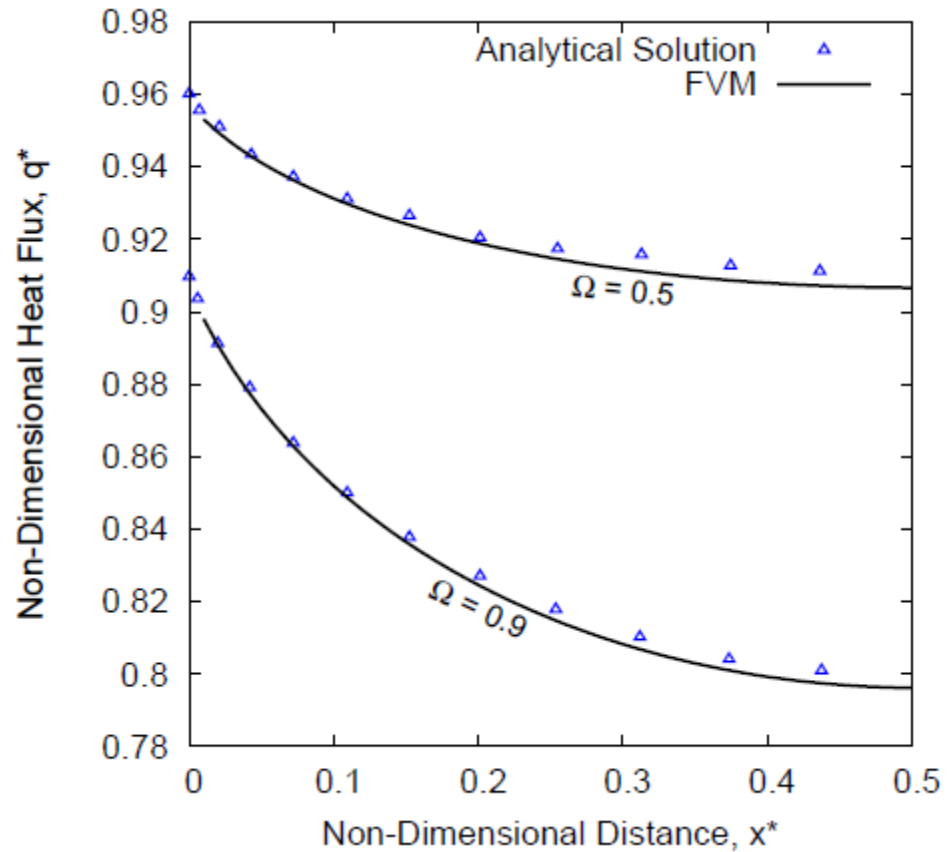
Figure 3.21 Non dimensional heat flux on a bottom surface of an absorbing-scattering 2D enclosure for different scattering albedos

Different scattering albedos were studied to show the effect of varying the radiative properties on the solution. As presented in Fig. 3.21, the FVM approximates the analytical solutions published by Crosbie [55].

F- Two dimensional isothermal absorbing emitting medium

This case studies the radiative heat flux in an absorbing emitting medium enclosed by cold surfaces.

The test parameters are listed in Table 9.

Table 9: isothermal absorbing-emitting 2D enclosure case parameters

Parameter	Value
$T_{top} = T_{left} = T_{right} = T_{bottom}$	0 K
T_{medium}	100 K
σ	0 m^{-1}
Ω	0
$L_x = L_y$	1
$\kappa^* = \kappa\, L$	1

The schematic for this test case is shown in Fig. 3.22.

$$T_{top} = 0\,,\epsilon = 1$$

$T_{left} = 0\,,\epsilon$ $\Phi = 1$ $T_{right} = 0\,,\epsilon$

$$T_{medium} = 100\ \text{K}$$
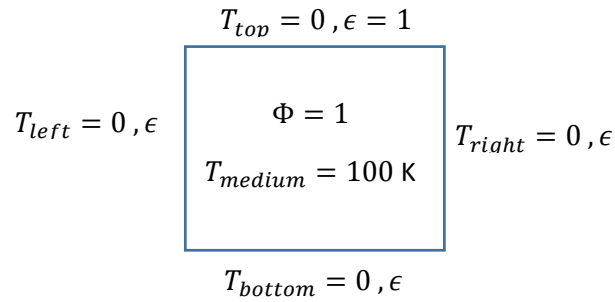
$$T_{bottom} = 0\,,\epsilon$$

Figure 3.22 isothermal absorbing-emitting 2D enclosure case schematic

Figure 3.23 describes the non-dimensional radiative heat flux along a bottom surface of an absorbing-emitting 2D hot medium enclosed by cold surfaces. Two optical thicknesses were used and the obtained results agrees with the analytical solutions published by Pedram [49].
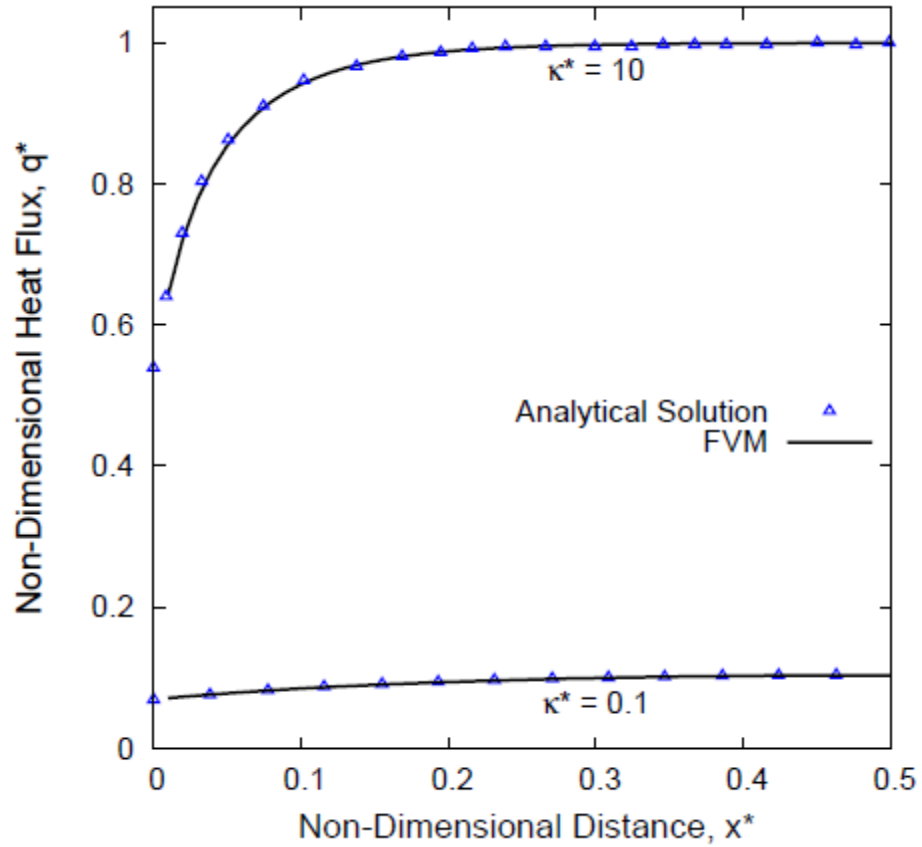
Figure 3.23 Non dimensional heat flux on a bottom surface of an absorbing-emitting 2D enclosure for different optical thicknesses

In general, the Finite Volume code did perform well for multiple test cases in one and two dimensional domains. It was noted that the optical thickness had a huge impact on the convergence rate. As the optical thickness increased, the convergence rate decreased. The P1 approximation did not consume a lot of time in comparison with the FVM. However, in most cases the FVM predicted closer solutions to the analytical solution.

Chapter 4
4.0 Decoupled analysis

There are multiple factors that could contribute to the analysis of radiative heat

transfer, such as the radiative properties, and the method of solution adopted to solve

the radiative heat transfer equation. The following sections will discuss the effect of

both on the analysis.

4.1 Effect of properties on the radiative parameters

To study the effect of changing the absorption coefficient on the radiative flux as well

as the divergence of radiative heat flux, a one-dimensional case as shown in Fig. 4.1

schematically is used. For this test case, both the finite volume method and the P1

approximation, are used.

The test case can be described as a purely absorbing one dimensional geometry with

a relatively cold medium enclosed between two hot surfaces. The boundaries are gray,

and diffusively scattering surfaces.

$$T_{top} = 100 , \epsilon = 1$$

$$T_{medium} = 50 \text{ K}$$

$$T_{bottom} = 100, \epsilon = 1$$
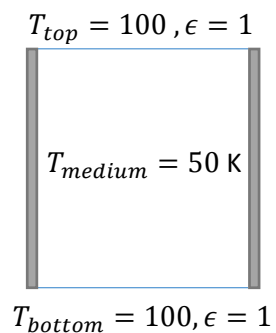
Figure 4.1 One dimensional absorbing-scattering one dimensional enclosure
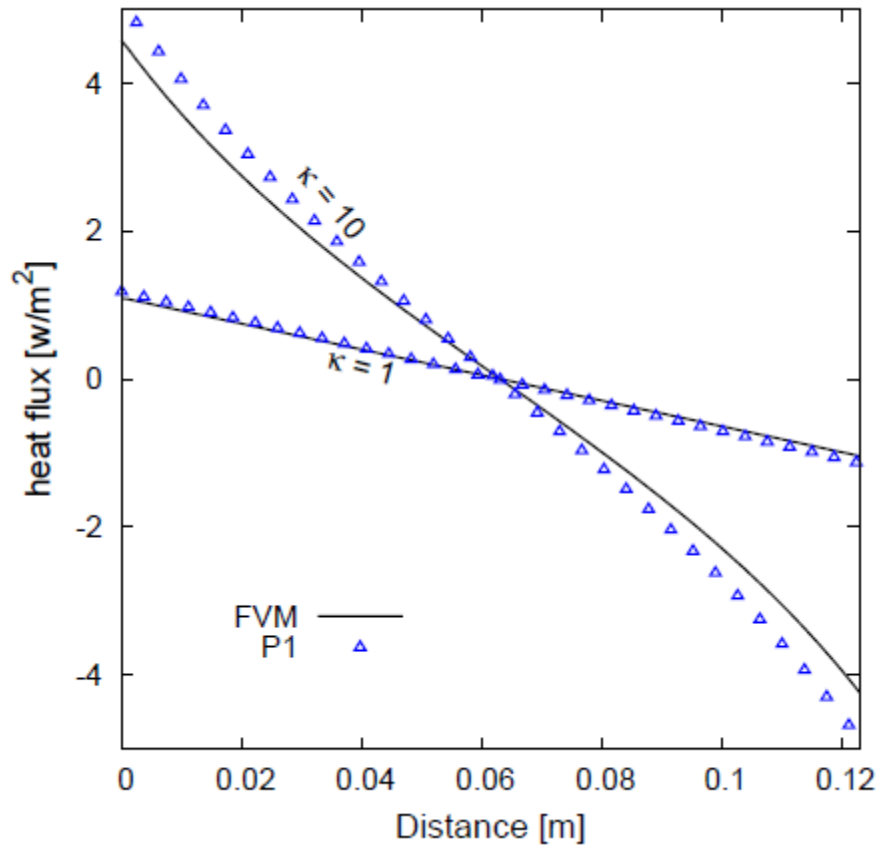
Figure 4.2 radiative heat flux in an absorbing-scattering one dimensional enclosure for multiple absorption coefficients

As evident from Fig. 4.2, the radiative heat flux value changes dramatically as the absorption coefficient is altered. Since each wavelength is associated with a different property, this provides evidence on how wavelength could change the analysis. Both methods provides comparable results except at the boundaries were a slight difference was noted especially with a higher absorption coefficient.

The divergence of radiative heat flux is an important parameter used in the coupled conduction-radiation analysis. The effect of changing the properties has on the divergence of radiative heat flux, is presented in Fig. 4.3.

72
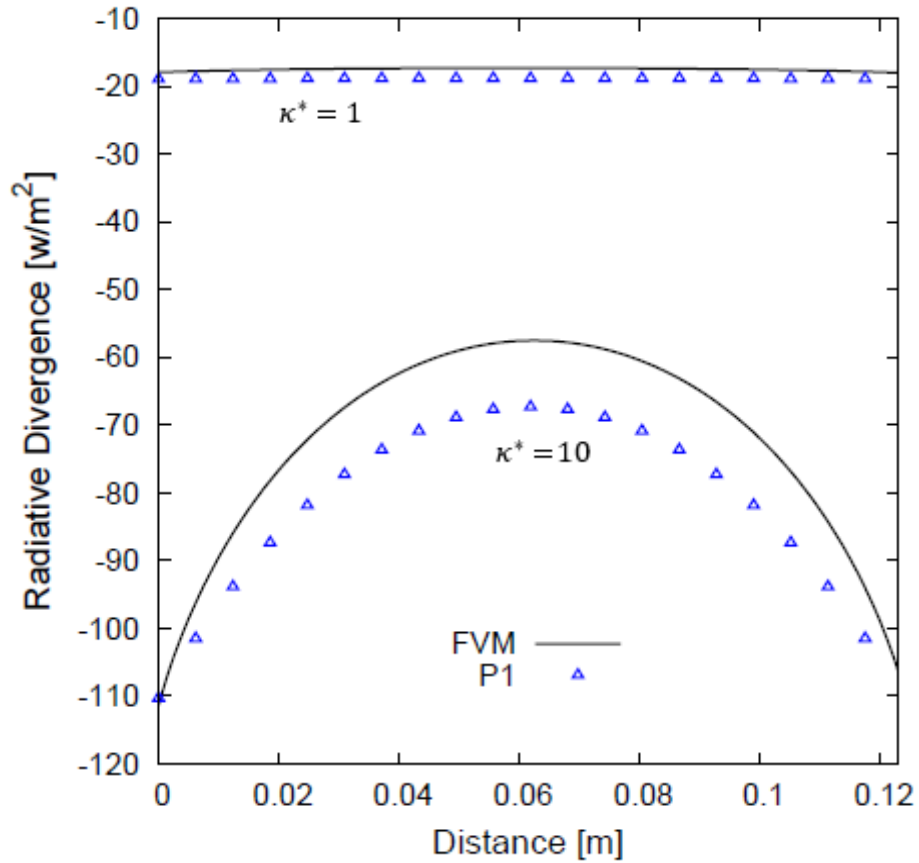
Figure 4.3 the divergence of radiative heat flux using the P1 approximation

As can be seen, the divergence of the radiative heat flux is extremely affected by the radiative properties. Consequently, the temperature response will be affected. It is also noted that as the absorption coefficient increases, the difference between both methods increase as well.

4.1.2 Comparison between P1, P3, and FVM

As evident in the previous section, there was a difference between results obtained

using the P1 approximation, and results obtained using the finite volume method. This

section discusses the results obtained using the finite volume code, against published

two-dimensional Monte Carlo results by Yang [56] and Modest [57], as well as P3 and P1

approximations results by Ravishankar et al. [58].

The non-dimensional parameters used subsequently are defined as:

- Non-dimensional heat flux $q^* = q/\sigma T^4$

- Non-dimensional length in the x-direction: $x^* = x/L_x$

- Non-dimensional length in the y-direction: $y^* = y/L_y$

Case A

The first test case represents a participating medium surrounded by four walls, in

which one of the walls is hot, and the rest of the walls are cold, as shown in Fig. 4.4. All

the walls are assumed to be black and only isotropic scattering is considered.
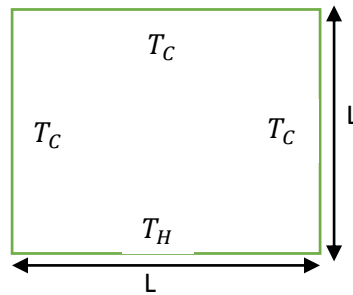
Figure 4.4 cold medium surrounded by three cold surfaces and one hot surface

Figure 4.5 non dimensional heat flux and relative error for the bottom surface (Top), Right surface (Middle), and top surface (Bottom) for optical thickness 0.1

Figure 4.6 non dimensional heat flux and relative error for the bottom surface (Top), Right surface (Middle), and top surface (Bottom) for optical thickness 1
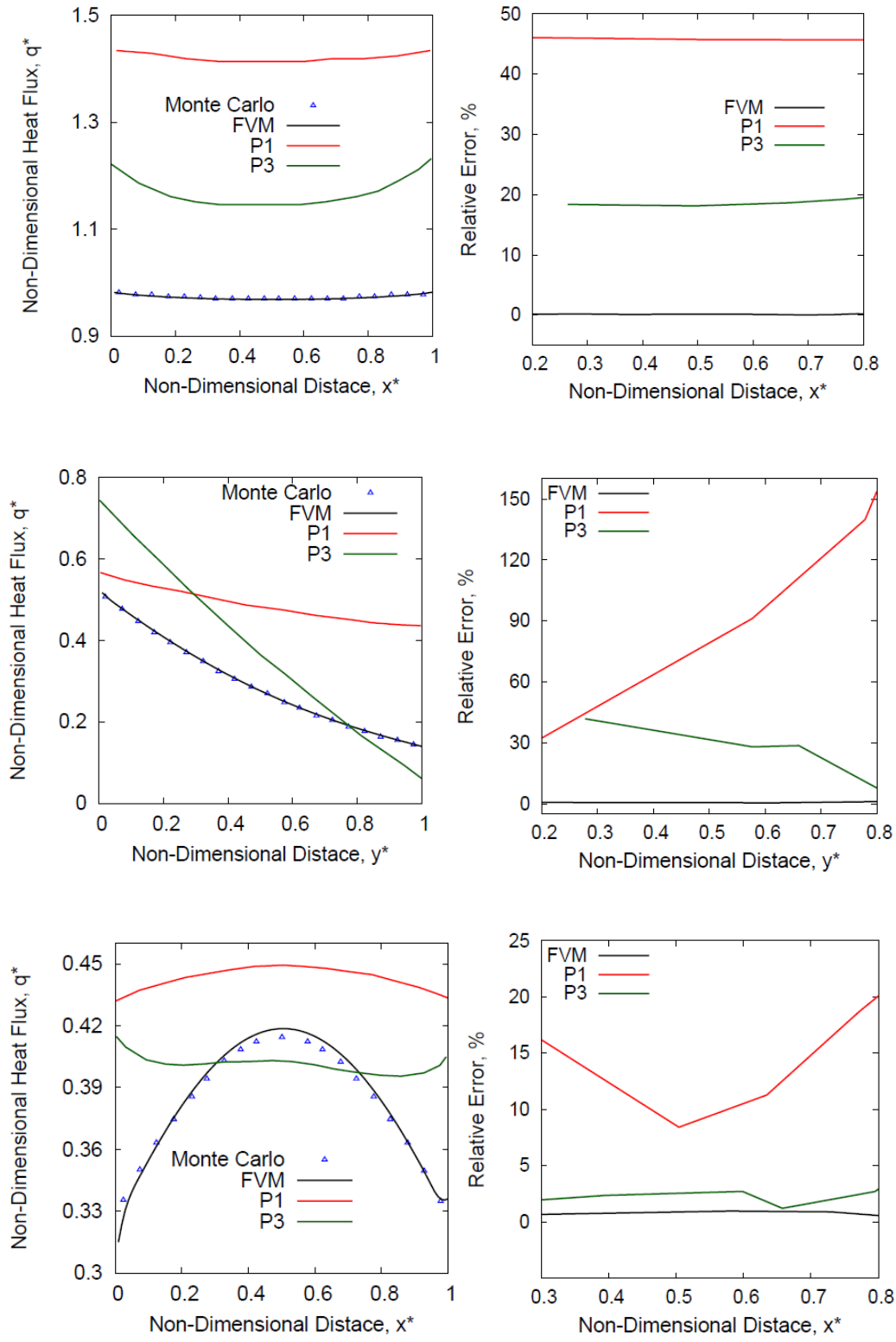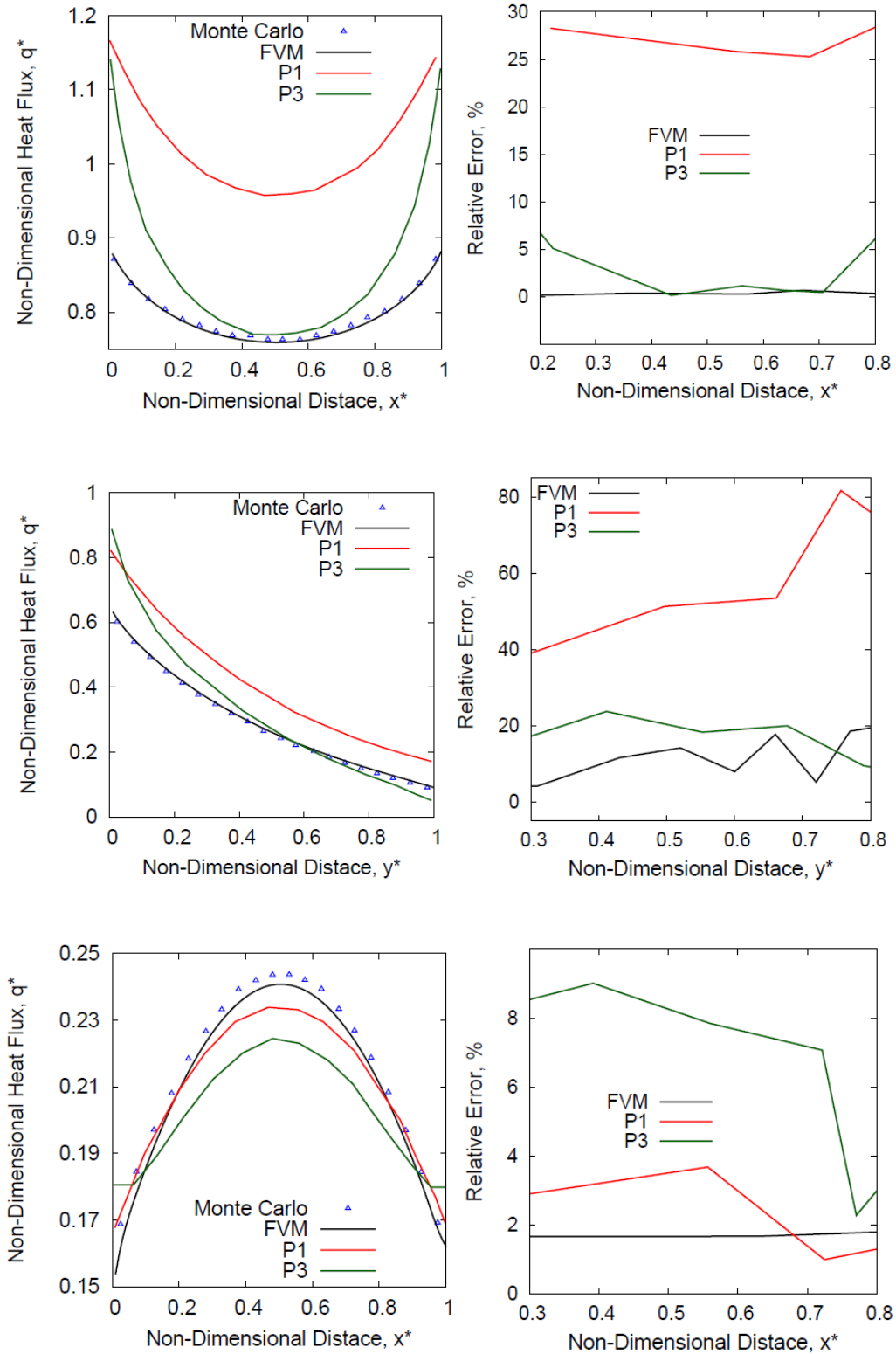
Figure 4.7 non dimensional heat flux and relative error for the bottom surface (Top), Right surface (Middle), and top surface (Bottom) for optical thickness 5

Figures 4.5-4.7 presents the non-dimensional radiative heat flux on different surfaces for three optical thicknesses. The obtained results using the FVM were compared with published spherical harmonics as well as Monte Carlo results.

It is clear from the previous figures that as the optical thickness increases the FVM produces more error this is the opposite of the spherical harmonics methods which produces lower error as the optical thickness increases. This is consistent with the behavior of both methods since the FVM performs better with optical thin material unlike the spherical harmonics methods which performs better with optical thick materials.

Figure 4.5 provides the results obtained for optical thickness equal to 0.1. As clear from Fig. 4.5, the P1 approximation provides larger error compared with the other two methods. The P1 approximation did produce an error that exceeds 150% for the right surface compared with a negligible error produced by the FVM. It is noted that the right surface produces larger error than the other surfaces.

Figure 4.6 compares the results obtained for optical thickness equal to 1. The error produced by the P1 approximation was reduced and the FVM error did increase. For the right surface, the P1 approximation did produce a maximum error of 82% compared with a maximum error of 20% produced by the FVM. The P3 approximation did not produce results as bad as the P1 approximation nor as good as the FVM. In general, the error produced using the P3 approximation is in between the other two methods.

Figure 4.7 presents the results obtained for optical thickness equal to 5. The error

produced using the P1 approximation was reduced dramatically where it did not exceed

16%. The error associated with the FVM increased. However, it did not exceed the error

produced by the P1 approximation except for the top surface where it produced a

slightly higher error.

CASE B

The second case represents a partially heated surface, surrounded by three cold walls,

as shown in Fig. 4.8
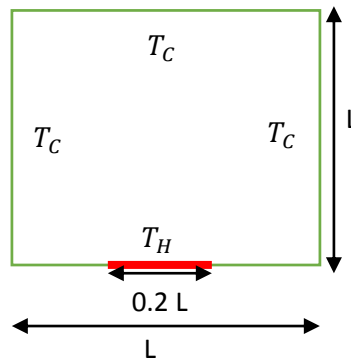
Figure 4.8 Partially heated surface surrounded by three cold surfaces schematic
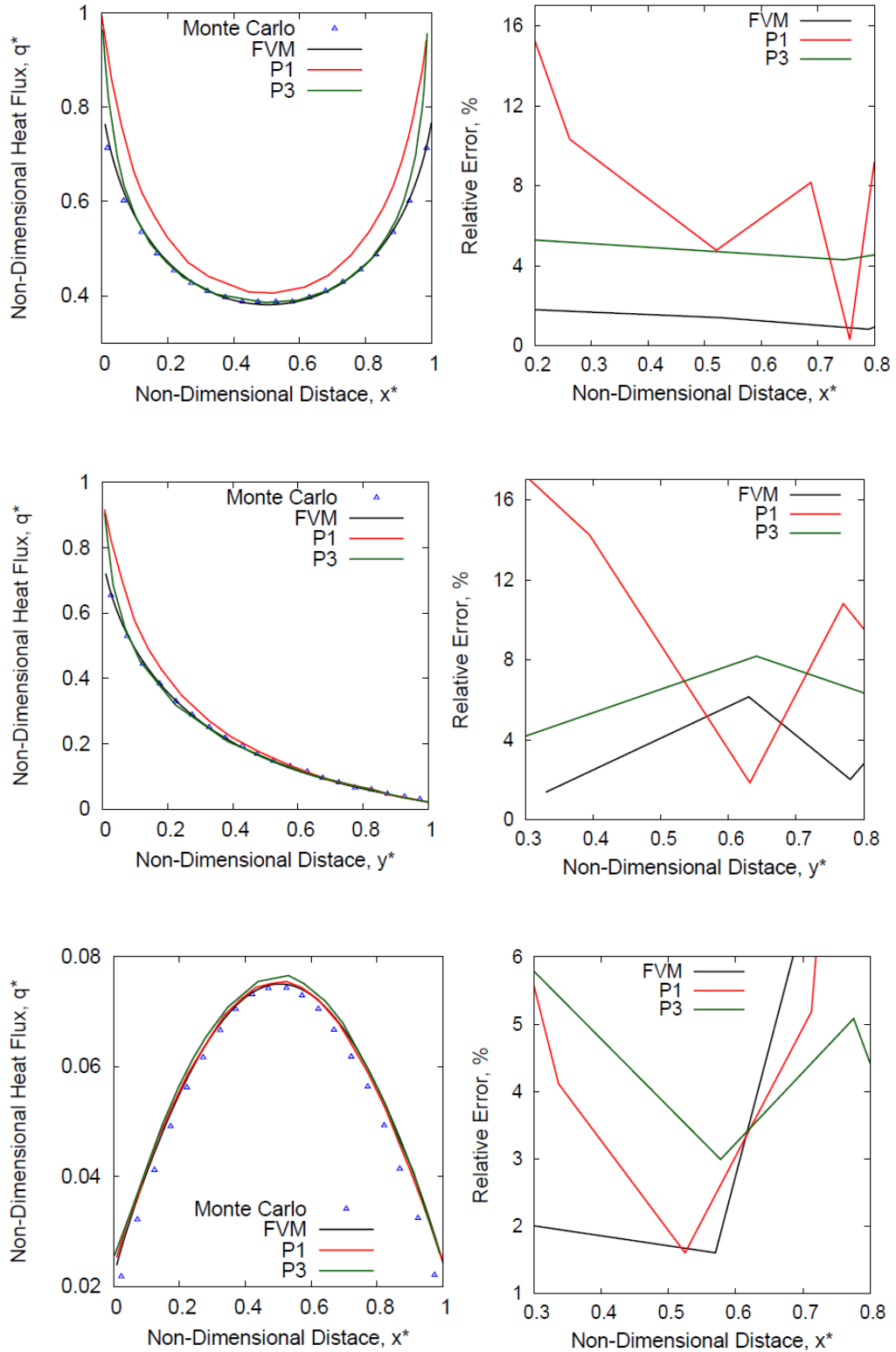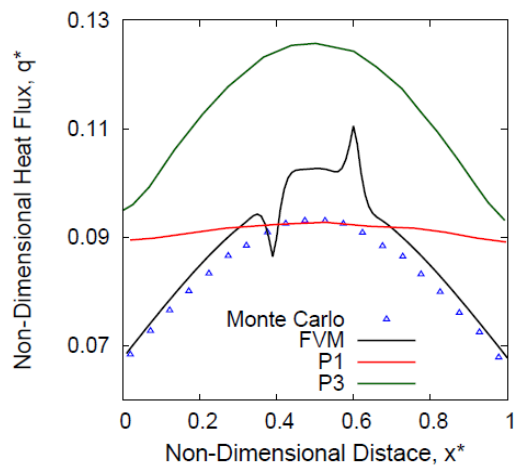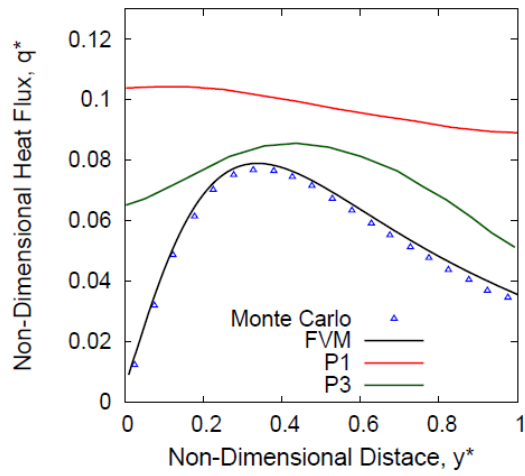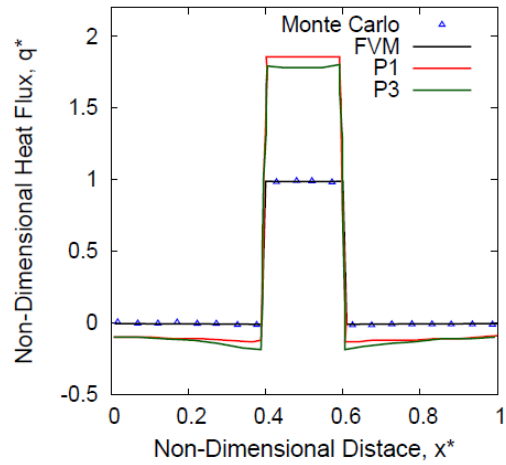
Figure 4.9 non dimensional heat flux and relative error for the bottom surface (Top), Right surface (Middle), and top surface (Bottom) for optical thickness 0.1
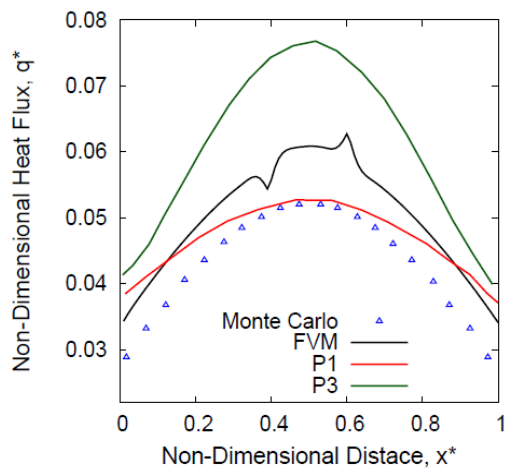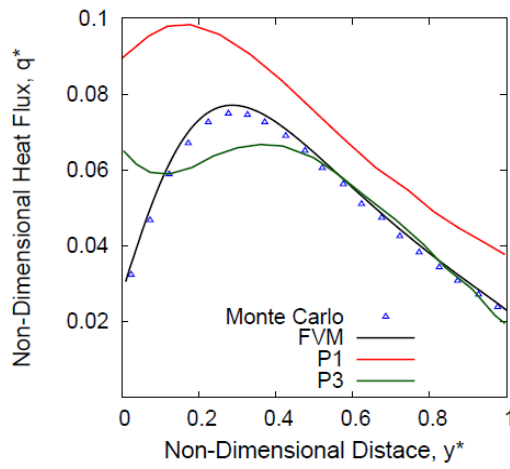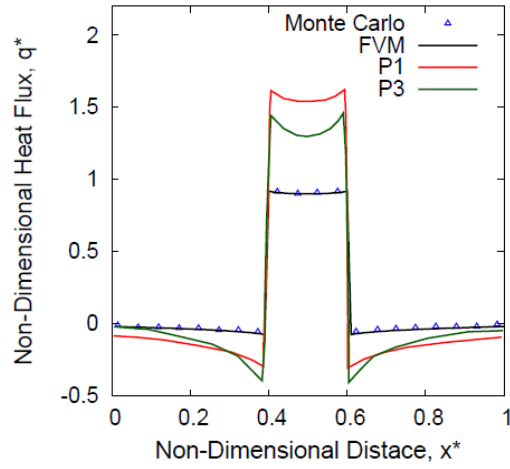
Figure 4.10 non dimensional heat flux and relative error for the bottom surface (Top), Right surface (Middle), and top surface (Bottom) for optical thickness 1
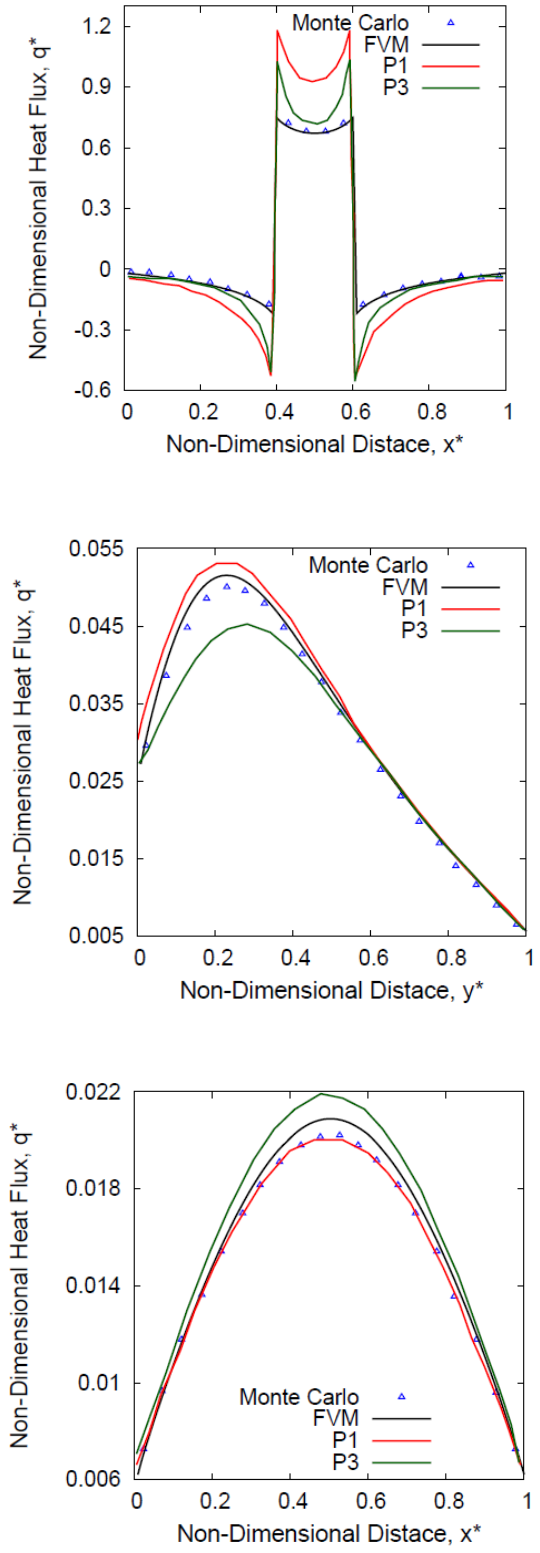
Figure 4.11 non dimensional heat flux and relative error for the bottom surface (Top), Right surface (Middle), and top surface (Bottom) for optical thickness 5

Figures 4.9-4.11 presents the non-dimensional radiative heat flux on different

surfaces for three optical thicknesses. The obtained results using the FVM were

compared with published spherical harmonics as well as Monte Carlo results.

This test case results agrees with the findings obtained from the previous case; as the

optical thickness increases, the error associated with the spherical harmonics decrease,

which can be noted by comparing the bottom surfaces. For optical thickness 0.1 the P1

approximation over predicts the solution with 100% error compared with 20% error for

optical thickness 5, as shown in Fig. 4.11.

The FVM did perform better than the other two methods in general, except for the

top surface. It is clear that the method produces a large error on the top surface

opposite to the hot segment which could be as a consequence of using the step scheme.

The error reduces as the optical thickness increases which is observed by comparing Figs

4.9, 4.10, and 4.11.

Chapter 5

Heat transfer through fibrous materials involve heat conduction through the solid matrix as well as the filling gas, and internal radiation through the pore structure. In the past, an effective thermal conductivity was used to account for both heat transfer mechanisms. However, this model fails to capture internal radiative heat transfer effects as was shown by Marcshall [59]. Moreover, it does not permit detailed radiative studies such as shock layer radiation which is dominated by line emission.

In order to perform coupled conduction-radiation analysis, the thermal conductivity should account for the conduction through the solid and gas phases without taking radiation into account therefore, the effect of internal radiation should be subtracted from the effective thermal conductivity (otherwise radiation will be added twice).

This chapter is dedicated to provide a method to extract the solid/gas thermal conductivity based on internal temperature measurements as well as heat fluxes. Retrieving thermal conductivity from internal temperature measurements is one form of inverse heat conduction problems (IHCP) which are considered ill posed problems [61,62].

Many methods has been proposed to estimate the unknown thermal conductivity based on minimization techniques which require iterative methods [63]. In this work a novel approach that does not require iterative procedures, and does not assume any functional form for the thermal conductivity is proposed.

A silica fiber LI-900 was used to perform validation of the proposed method using effective thermal conductivities published by NASA [64]. The results are compared against previously published results based on iterative methods.

5.1 method description

The proposed method to obtain the temperature dependent solid/gas thermal conductivity consists of two main problems: the direct problem, and the inverse problem.

5.1.1 Direct problem

The direct problem is used to obtain the internal temperature measurements using the temperature dependent effective thermal conductivities by solving the one dimensional energy equation.

The mathematical formulation as well as the boundary conditions are described as following

$$\rho \, c_p \frac{\partial T}{\partial t} = \frac{\partial}{\partial x}\left[k_{eff} \frac{\partial T}{\partial x}\right] \qquad (5.1)$$

$$q_{x=0} = \left[k_{eff} \frac{\partial T}{\partial x}\right]_{x=0}$$

$$q_{x=L} = \left[k_{eff} \frac{\partial T}{\partial x}\right]_{x=L}$$

where ρ is density, c_p is specific heat, t is time, T is temperature, and k_{eff} is the effective thermal conductivity.

5.1.2 Inverse problem

The inverse problem is used to estimate one of the unknown parameters in the energy equation. Here, this parameter is the temperature dependent solid/gas thermal conductivity, since the internal temperature measurements, radiative heat fluxes, and conductive heat fluxes are all known quantities.

The mathematical formulation for the inverse problem is described as

$$\rho\, c_p \frac{\partial T}{\partial t} = \frac{\partial}{\partial x}\left[k_{solid} \frac{\partial T}{\partial x}\right] + q_{rad} \quad (5.2)$$

where ρ is density, c_p is specific heat, t is time, T is temperature, k_{solid} is the solid/gas thermal conductivity, and q_{rad} is the radiative heat source term.

The numerical formulation for the inverse analysis is described using the finite volume discretization over a control volume as shown in Fig. 5.1. The gradients appearing in Eq. 5.2 are approximated using a forward first order differencing scheme.
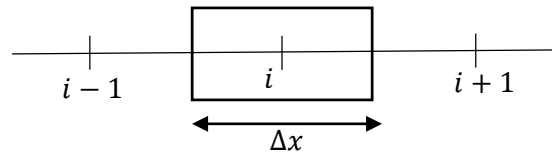
Figure 5.1 one dimensional control volume

$$\rho\, c_p \frac{\Delta T}{\Delta t}\, \Delta V = \left[k_{solid} \frac{\Delta T}{\Delta x}\right]_{i+1/2} - \left[k_{solid} \frac{\Delta T}{\Delta x}\right]_{i-\frac{1}{2}} + q_{rad}\, \Delta V \qquad (5.3)$$

$$\rho\, c_p \frac{\Delta T}{\Delta t}\, \Delta V + \left[k_{solid} \frac{\Delta T}{\Delta x}\right]_{i-1/2} - q_{rad}\, \Delta V = \left[k_{solid} \frac{\Delta T}{\Delta x}\right]_{i+1/2} \qquad (5.4)$$

$$k_{solid_{i+1/2}} = \left[\frac{\Delta x}{\Delta T}\right]_{i+1/2} \times \left[\rho\, c_p \frac{\Delta T}{\Delta t} \Delta V + \left[k_{solid} \frac{\Delta T}{\Delta x}\right]_{i-\frac{1}{2}} - q_{rad}\, \Delta V\right] \quad (5.5)$$

Solving Eq. 5.5 for each grid point results in a system of equations for the unknown solid/gas thermal conductivity at each surface of the control volume. In Eq. 5.5 both solid thermal conductivities $k_{i-1/2}$, and $k_{i+1/2}$ are unknowns, making the number of unknowns larger than the number of equations. To close the set of equations boundary conditions are needed.

Thermal conductivities at the boundaries are obtained by extracting the radiative heat flux from the effective heat flux

The direct problem provides the effective heat flux, as well as the internal temperature measurements required for the radiative heat transfer solver to obtain the radiative heat flux. With the known quantities it is possible to obtain the solid conductivity at the boundary using the following relations

$$q_{eff} = q_{solid} + q_{rad} \quad (5.6)$$

$$k_{eff} \frac{\Delta T}{\Delta x} = k_{solid} \frac{\Delta T}{\Delta x} + q_{rad} \quad (5.7)$$

$$k_{solid} = \frac{\Delta x}{\Delta T}\left[k_{eff} \frac{\Delta T}{\Delta x} - q_{rad}\right] \quad (5.8)$$

After obtaining the solid thermal conductivity at the boundary it is possible to substitute its value in Eq. 5.5 and solve for the unknown thermal conductivities.

5.2 Results

Temperature dependent solid/gas thermal conductivities were obtained using the P1

approximation as well as the Finite Volume method for an LI-900 ceramic tile material.

The radiative properties used are the ones published by Marschall [59]. Shown in Fig.

5.2.
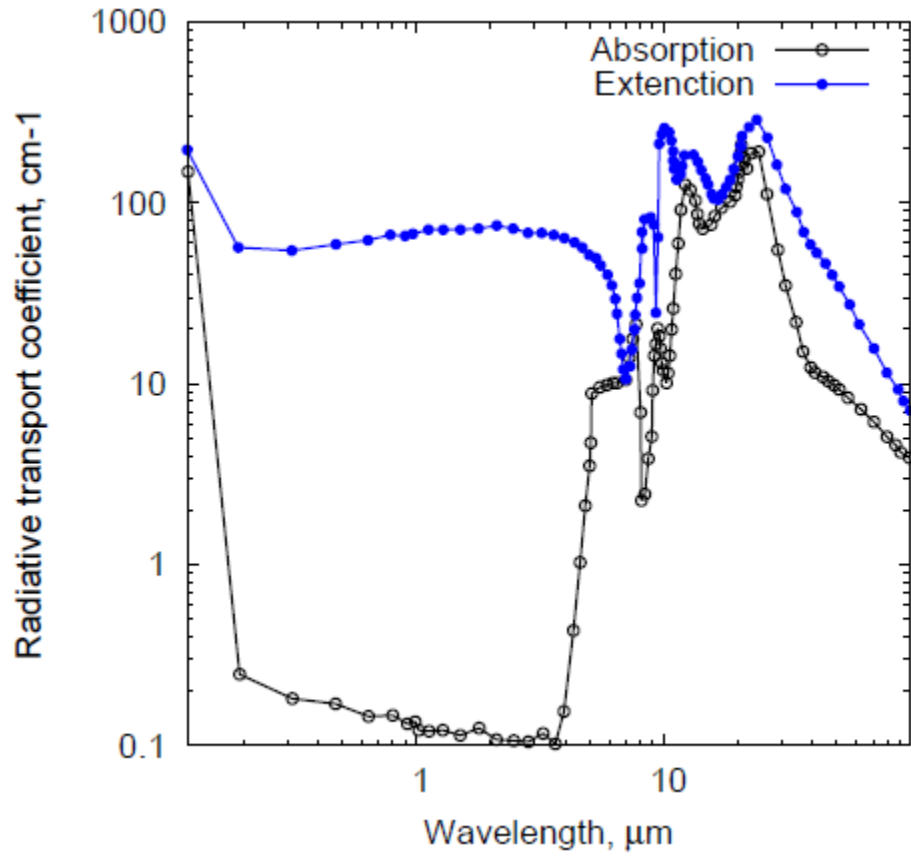
Figure 5.2 Spectral radiative properties for LI-900
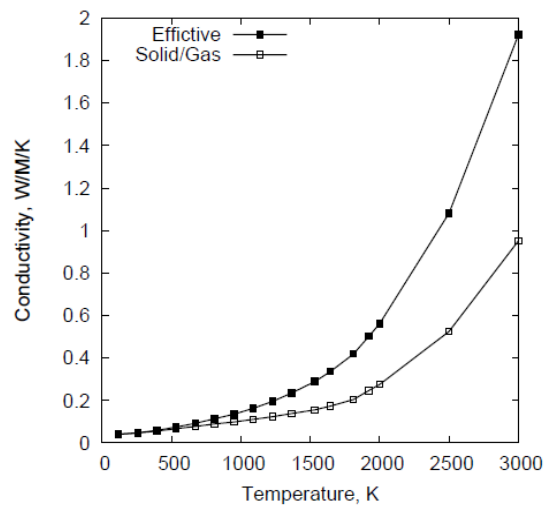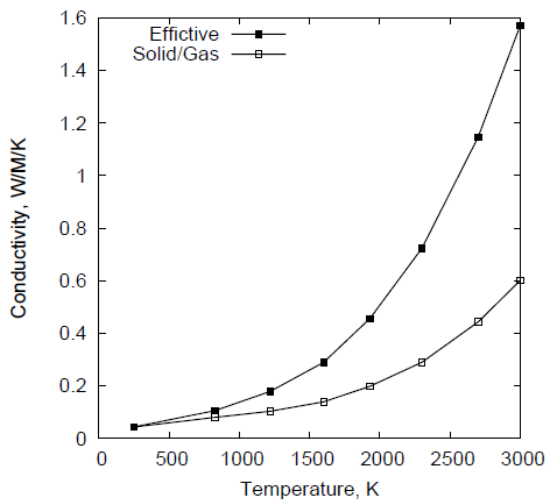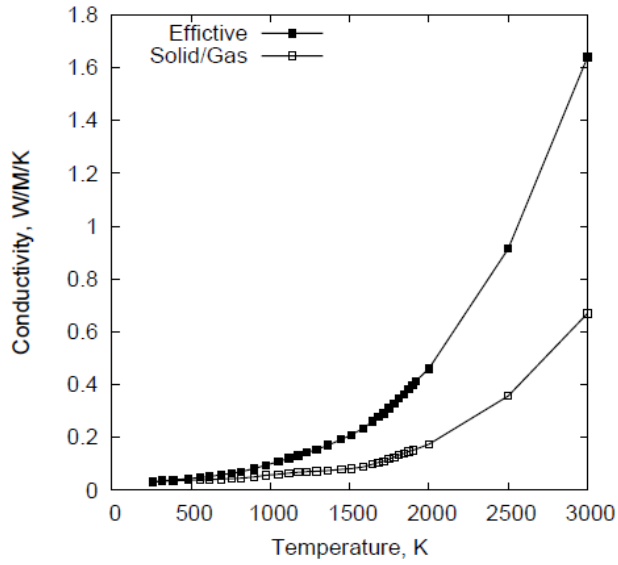
Figure 5.3 Effective and solid/gas Temperature dependent thermal conductivity for pressure 0.01 atm (top), 0.1 atm (bottom-left), and 1 atm (bottom-right)

Figure 5.3 shows the obtained solid/gas thermal conductivity using the P1

approximation for a wide range of temperatures against the effective thermal

conductivities published by NASA [64] for pressures 0.01, 0.1, and 1 atm.

The procedure was repeated using the Finite volume and the results are shown in Fig.

5.4 in comparison with the results obtained using the P1 approximation.
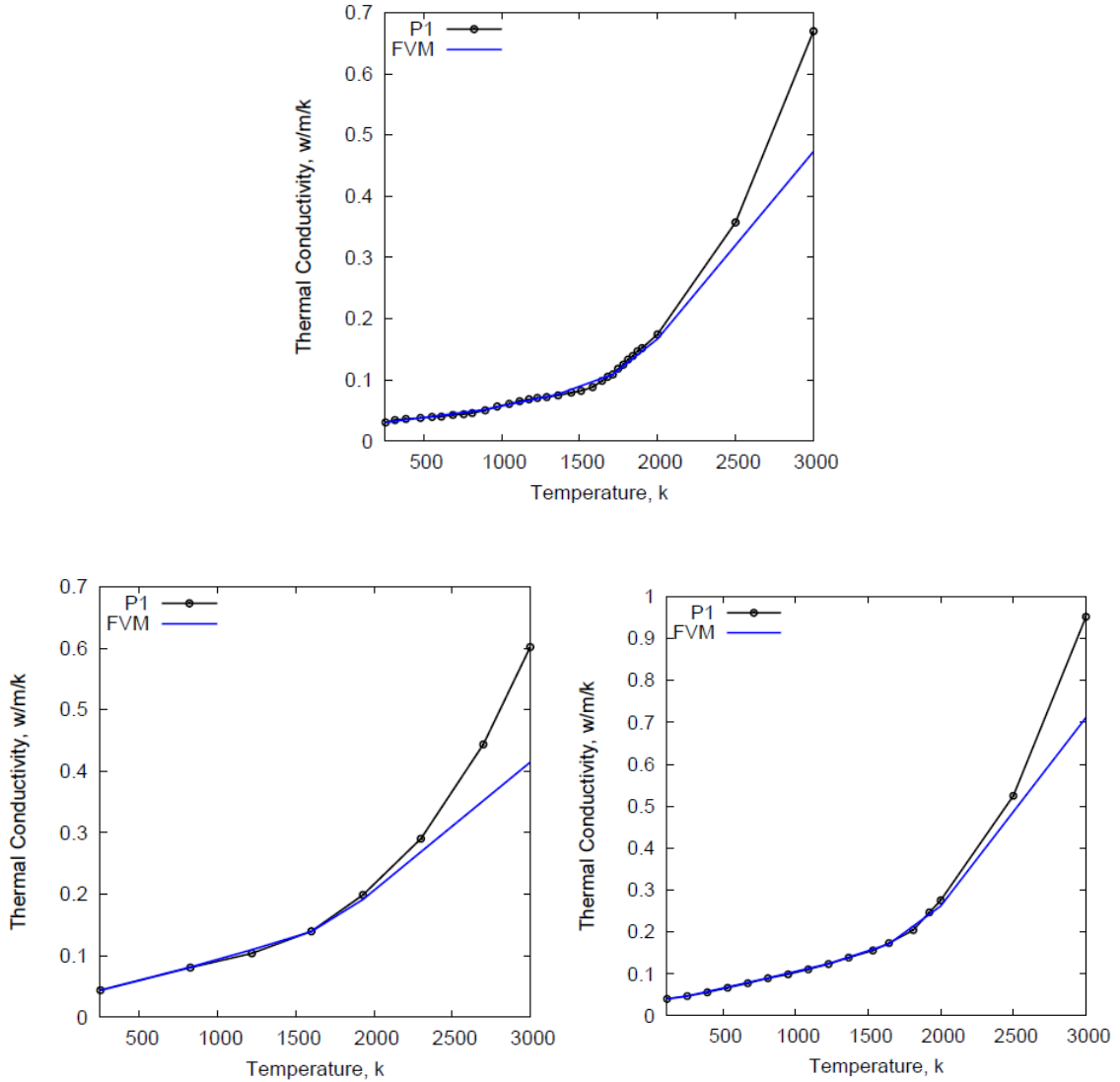
Figure 5.4 Solid/gas Temperature dependent thermal conductivity for pressure 0.01 atm (top), 0.1 atm (bottom-left), and 1 atm (bottom-right)

As clear from Fig. 5.4, both methods provides similar predictions for the solid/gas

thermal conductivity up to around 2000 K, afterwards the finite volume method

provides lower values. The finite volume method consumed larger amount of time

compared with the P1 approximation for the given spectral radiative properties which

prevented the possiblty to run spectral studies using the FVM. The P1 approximation is

adopted for the rest of this work and is used to validate the values obtained for the

solid/gas thermal conductivity.

5.3 Validation

The three test cases were proposed by Marschall [59] are reproduced in this section,

using the new thermal conductivity values. A Li-900 sample was used to compare the

results obtained using the effective thermal conductivity model (pure conduction) and

the coupled approach using the solid/gas thermal conductivity with the P1

approximation model.

The first test case is a radiant heating test case with a 1.25 cm sample at 1 atm

pressure. A 60 s heating profile was imposed on one side of the sample as shown in Fig.

5.5, while keeping the other side at 256 K. Figure 5.5, shows the surfaces temperature

as well as the internal temperature measurements for 0.1, 0.3, and 0.5 cm for both

models as well as the temperature difference between them.

Figure 5.5 Radiant heating simulation; Left: internal temperature profile, Right:
Temperature difference between pure conduction and the coupled approach.

It is clear from Fig 5.5, that larger differences were obtained near the hot surface, where large temperature gradients are present.

   The second test case represents an arc-jet simulation test case with a 4 cm sample at 0.01 atmospheric pressure. The front surface temperature rise to 1700 k within 5 seconds, as shown in Fig 5.6, followed by a cool down period. The back surface remains adiabatic. Temperature measurements were obtained for 0.5, 1, 2, 3, and 4 cm depths.

Figure 5.6 Arc-jet simulation; Left: internal temperature profile, Right: Temperature difference between pure conduction and the coupled approach.

   Major temperature differences were obtained near the hot surface as well as during the cool down period.

   The third test case represents the conditions of a space shuttle entry simulation on a 5 cm specimen at 0.1 atm pressure. The front surface was subject to the temperature profile shown in Fig. 5.7, while the back surface was kept adiabatic. Temperature measurements were taken at 1, 2, 3, 4, and 5 cm depths.

Figure 5.7 Space Shuttle heating simulation; Left: internal temperature profile, Right: Temperature difference between pure conduction and the coupled approach.

Lower temperature differences were obtained for this case due to the relatively

lower temperature gradients present. It is noted from Fig. 5.7, that the major

temperature differences were obtained during the cool-down period.

5.4 Comparison

In this section multiple cases will be used to compare the results obtained using the

solid/gas thermal conductivities published by Marschall [59], and the results obtained

using the solid/gas thermal conductivities proposed in this work as described earlier

with similar domain parameters.

The RMS error presented in the following tables is calculated using the following

relation

$$e = \sqrt{\frac{\sum_{i=1}^{n} \left(\frac{T_{cond} - T_{coupled}}{T_{cond}} \right)^2}{n}}$$

where n represents the number of time steps

5.4.1 Radiant heating simulation

The first validation case described in the previous section will be replicated with the solid/gas thermal conductivities published by Marschall [59]. Figure 5.8 represents the internal temperature measurements as well as the temperature difference between the coupled approach and the effective thermal conductivity approach.
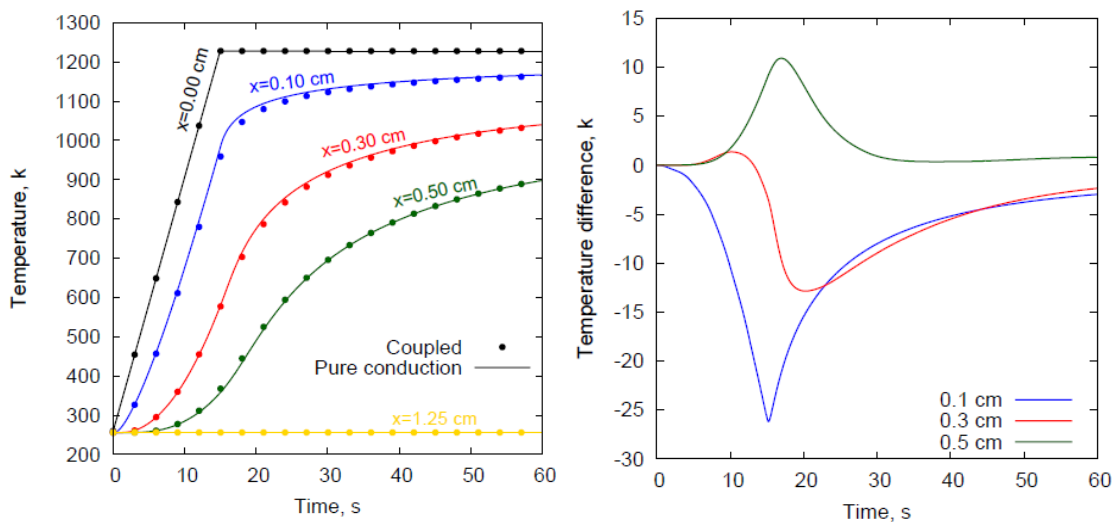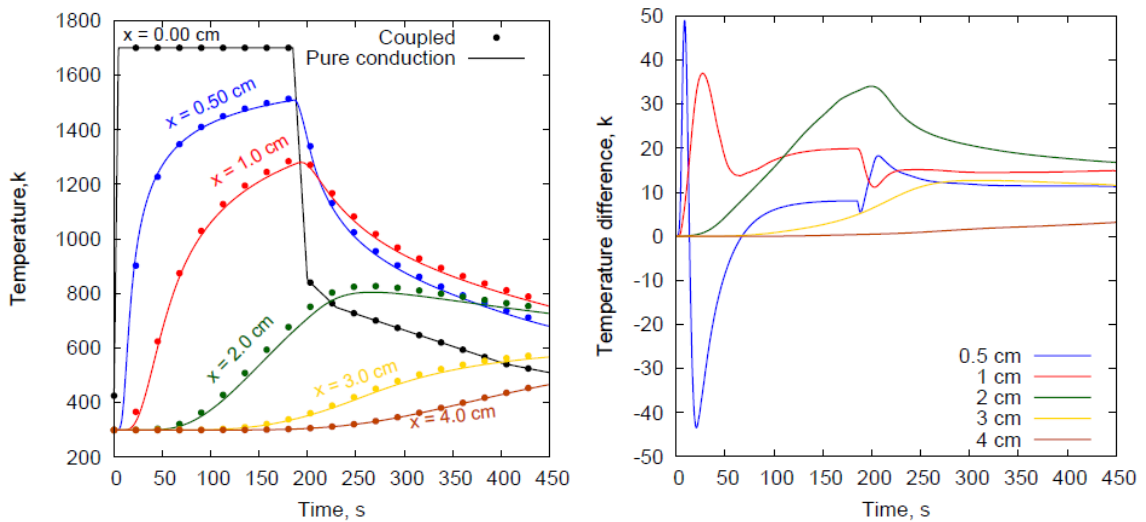

Figure 5.8 Radiant heating simulation; Left: internal temperature profile, Right: Temperature difference between pure conduction and the coupled approach using Marschall et al. [59] thermal conductivities.

It is clear from Fig 5.8 that greater differences were obtained using the solid/gas thermal conductivities published by Marshall et al. [59], especially within the shallow region near the hot surface.

Table 10 shows the maximum absolute temperature difference between the coupled and the effective thermal conductivity models, and compares the results obtained using the current and previously published solid/gas thermal conductivities.

Table 11 shows the RMS error for each thermo-couple and compares between the error obtained using the current and previous solid/gas thermal conductivities. The temperature difference and the associated error were reduced by using the current thermal conductivities.

Table 10: Maximum temperature difference (K).

TC	Previous	Current
0.1 (cm)	35.84	26.18
0.3 (cm)	24.91	12.85
0.5 (cm)	12.30	10.92

Table 11: RMS error comparison between current and previous work.

TC	Previous work error (%)	Current work error (%)
0.1 (cm)	1.50×10^{-2}	1.03×10^{-2}
0.3 (cm)	1.76×10^{-2}	7.84×10^{-3}
0.5 (cm)	1.31×10^{-2}	8.94×10^{-3}

5.4.2 Arc-Jet simulation

The second test case described in section 5.3 is replicated with the thermal conductivities published by Marschall et al. [59] and the results are presented in Fig. 5.10.

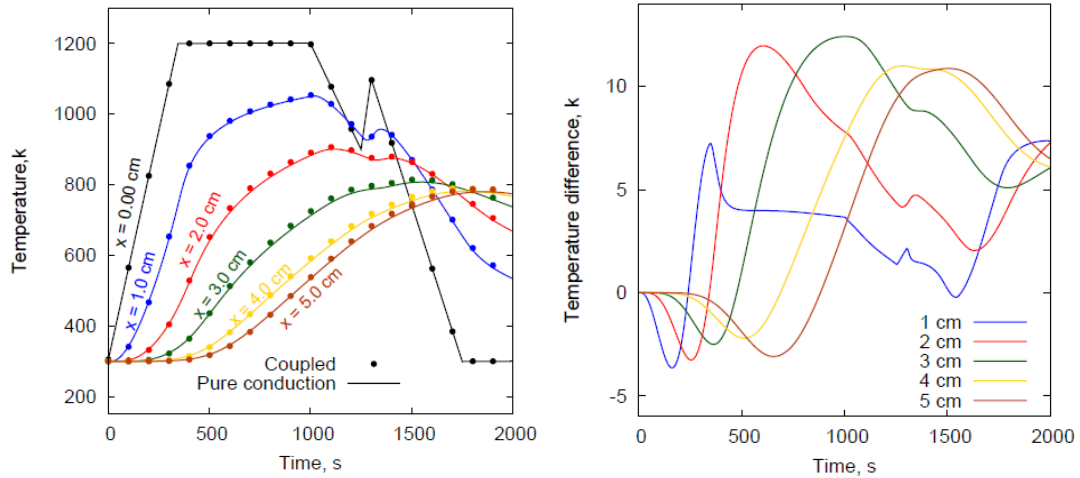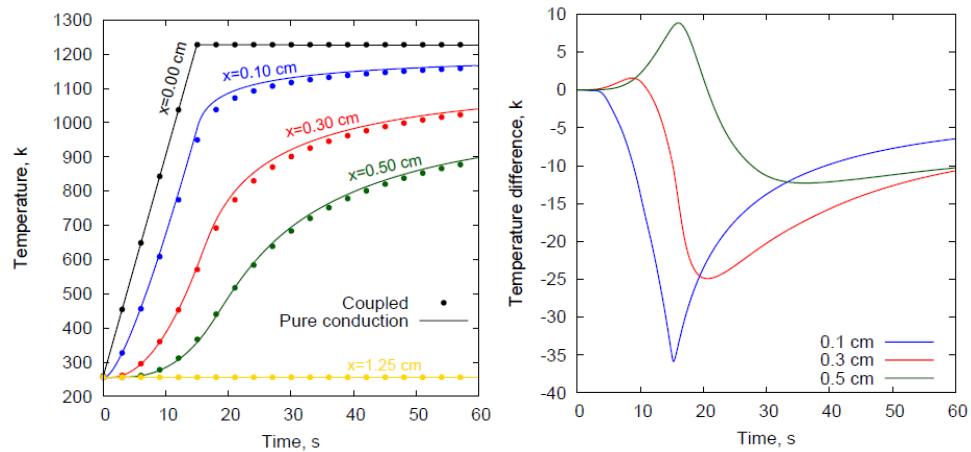*Figure 5.9 Arc-jet simulation; Left: internal temperature profile, Right: Temperature difference between pure conduction and the coupled approach using Marschall et al [59] thermal conductivities.*

Similar results were obtained for the second case where higher differences were obtained near the hot surface as shown in Fig. 5.9.

Table 12 shows the maximum temperature difference between the coupled and effective thermal conductivity models and compares between the error obtained using current and previous solid/gas thermal conductivities.

Table 13 shows the RMS error for each thermo-couple and compares it with the error obtained using current and previous solid/gas thermal conductivities.

Both tables shows that the maximum temperature difference and the error were reduced by using the current solid/gas thermal conductivities.

Table 12 Maximum temperature difference (K)

TC	Previous work	Current work
0.5 (cm)	118.75	49.03
1 (cm)	61.28	36.97
2 (cm)	40.29	34.06
3 (cm)	36.07	12.69
4 (cm)	44.47	3.16

Table 13 RMS error comparison between current and previous work.

TC	Previous work error (%)	Current work error (%)
0.5 (cm)	3.53×10^{-2}	1.98×10^{-2}
1 (cm)	3.14×10^{-2}	2.71×10^{-2}
2 (cm)	3.49×10^{-2}	3.31×10^{-2}
3 (cm)	4.95×10^{-2}	1.87×10^{-2}
4 (cm)	4.96×10^{-2}	3.65×10^{-2}

5.4.3 KRUPS

The available thermal conductivities published by Marschall et al. [59], do not cover a wide range of temperatures. Because most heat shield average surface temperature far larger than 1900 K the maximum temperature covered by Marschall et al. [59]. To illustrate that example, the heat flux projected for the Kentucky Re-Entry Universal Payload System (KRUPS) is used.

A temperature profile was imposed on one side of a 5 cm LI-900 sample, as shown in Fig. 5.10. An adiabatic wall is applied on the other side, with a 0.1 atm pressure. Internal measurements were taken at 1, 2, 3, 4, and 5 cm depths.

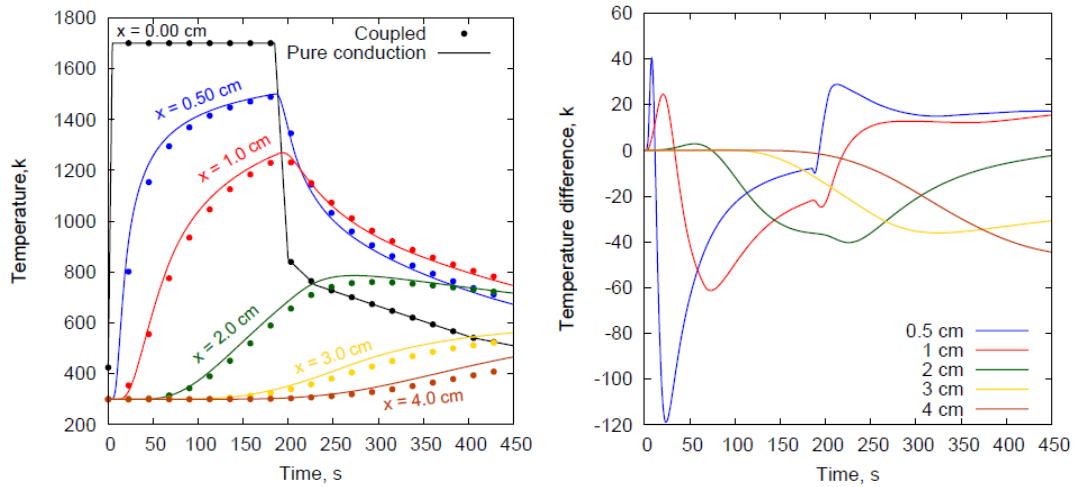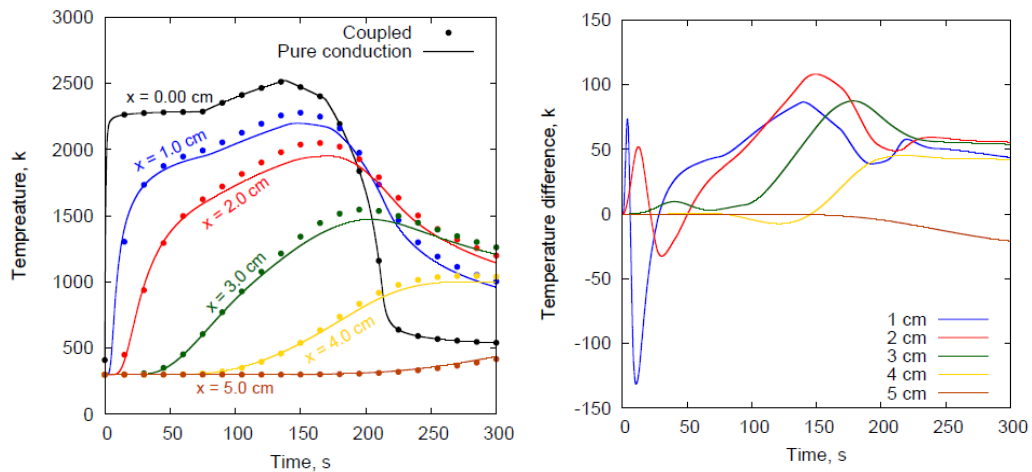*Figure 5.10 KRUPS heating simulation, Left: internal temperature profile, Right: Temperature difference between pure conduction and the coupled approach using Marschall et al [59] thermal conductivities.*
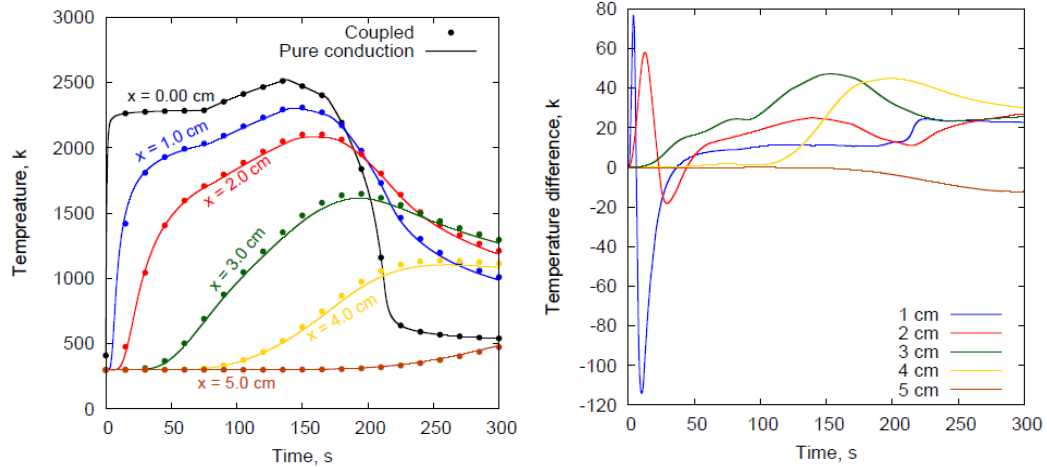
Figure 5.11 KRUPS heating simulation, Left: internal temperature profile, Right: Temperature difference between pure conduction and the coupled approach using current solid/gas thermal conductivities.

Figures 5.10 and 5.11 presents the internal temperature measurements as well as the temperature difference between the coupled and effective thermal conductivities model using the thermal conductivities published by Marschall et al. [59] and the thermal conductivities obtained in this work respectively.

Table 14 represents the maximum temperature difference between the coupled and effective thermal conductivity models and compares between the maximum difference obtained using current and previous solid/gas thermal conductivities. Table 15 represents the RMS error for each thermo-couple using current and previous solid/gas thermal conductivities.

It is clear from the figures as well as the tables provided that both of the error and the maximum temperature difference were reduced for similar domain parameters.

Table 14 Maximum temperature difference (K)

TC	Previous work	Current Work
1 (cm)	131.32	113.93
2 (cm)	108.14	57.97
3 (cm)	87.47	47.20
4 (cm)	45.34	44.89
5 (cm)	20.84	12.22

Table 15 RMS error comparison between current and previous work.

TC	Previous work error (%)	Current Work error (%)
1 (cm)	4.12×10^{-2}	2.68×10^{-2}
2 (cm)	4.48×10^{-2}	2.98×10^{-2}
3 (cm)	3.80×10^{-2}	2.69×10^{-2}
4 (cm)	3.12×10^{-2}	3.03×10^{-2}
5 (cm)	2.12×10^{-2}	1.37×10^{-2}

5.4.4 IsoQ

    Arc jet facilities are used to produce extreme environments suitable for thermal

protection systems (TPS) material testing [50]. Test samples are shaped into an IsoQ

shape to achieve a constant heat flux on the front surface. An IsoQ sample subject to a

hypersonic flow is presented in Fig. 5.12.
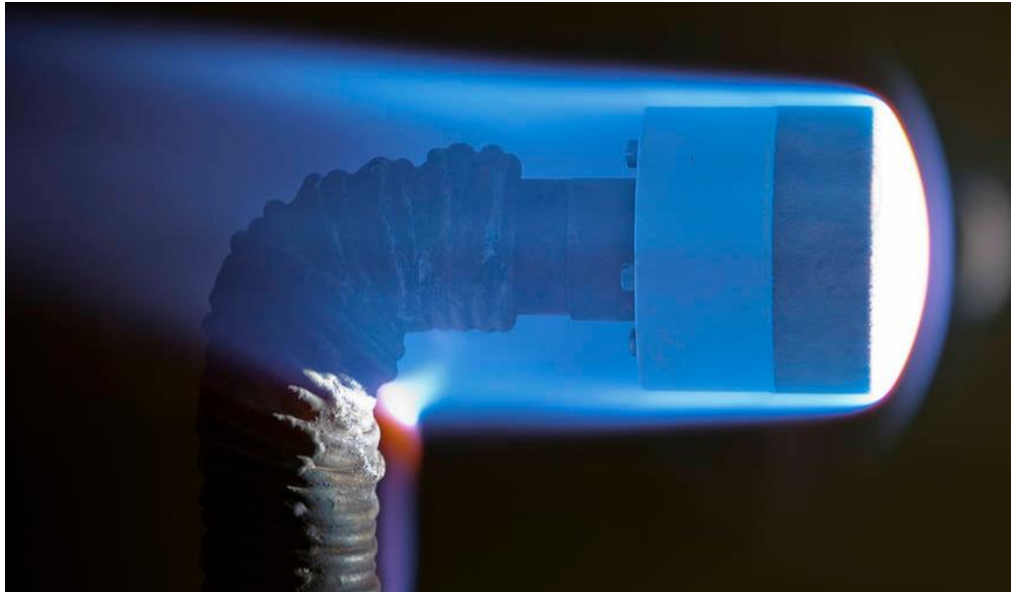
Figure 5.12 IsoQ sample in an arc-jet test (Courtesy of NASA [23])

    A 2D *IsoQ sample* was heated from 300 K to a non-uniform temperature profile in 5

seconds and remains constant for the heating time, at 1 atm. This calculation was

performed using the KATS-MR code (courtesy of Raghava S.C. Davuluri), more details

about the case can be found in ref. [65,53].

    Figure 5.13 represents the mesh and the imposed temperature profile at the surface

of the sample.
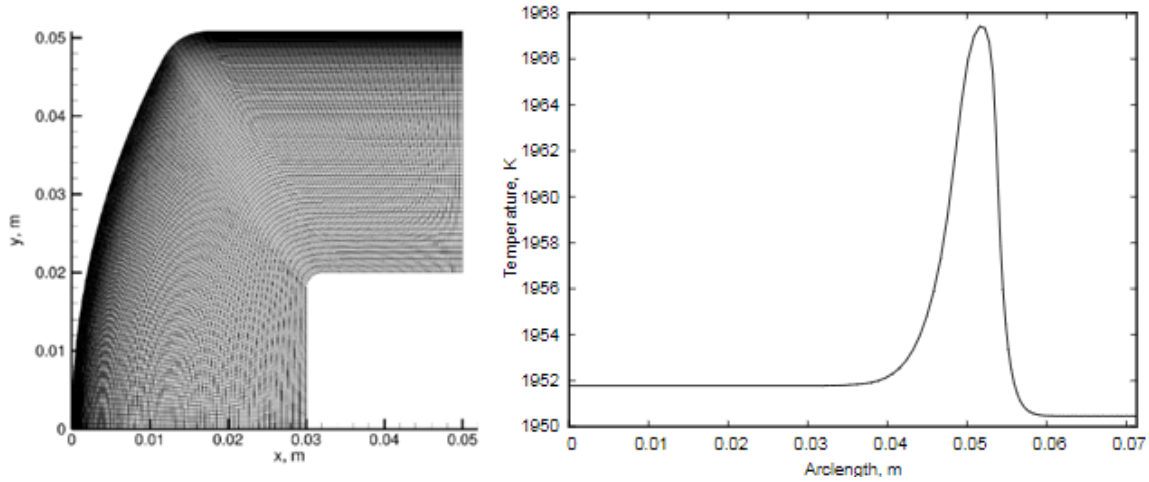
*Figure 5.13 2D Mesh of IsoQ sample (*left*), Non-uniform temperature profile at the surface of an IsoQ sample (*right*) courtesy of Raghava [65].*

Figure 5.14 represents the internal temperature measurements at different

thermocouple locations, shown in Table 16. The results were obtained using previously

published solid/gas thermal conductivities by Marschall et al. [59] as well as the current

conductivities in comparison with the effective thermal conductivity model.

It is noted that the difference between the effective thermal conductivity model and

the coupled model was reduced specially for high temperature locations, which agrees

with the previously discussed results for one dimensional geometries.

Table 16 Thermo-couple locations

Thermo Couple (TC)	Coordinate (m)	Thermo Couple (TC)	Coordinate (m)
1	(0.0 , 0.0)	6	(0.02286, 0.02540)
2	(0.00381, 0.0)	7	(0.02286,0.03810)
3	(0.00762, 0.0)	8	(0.02286,0.04445)
4	(0.01143, 0.0)	9	(0.03048,0.04445)
5	(0.01542,0.0)		
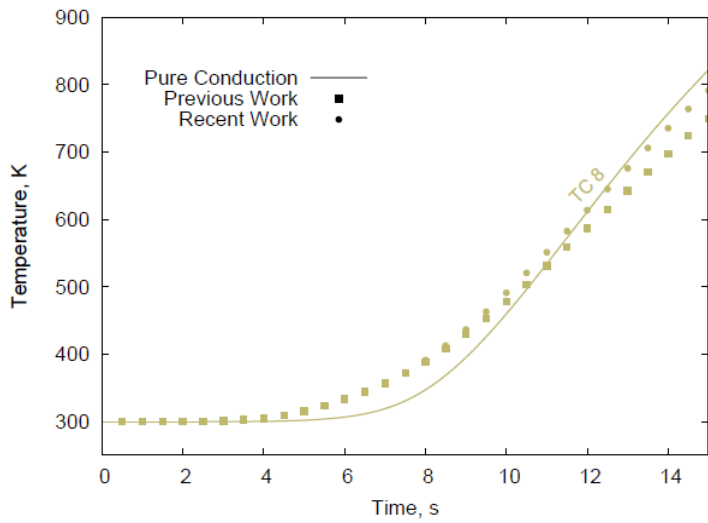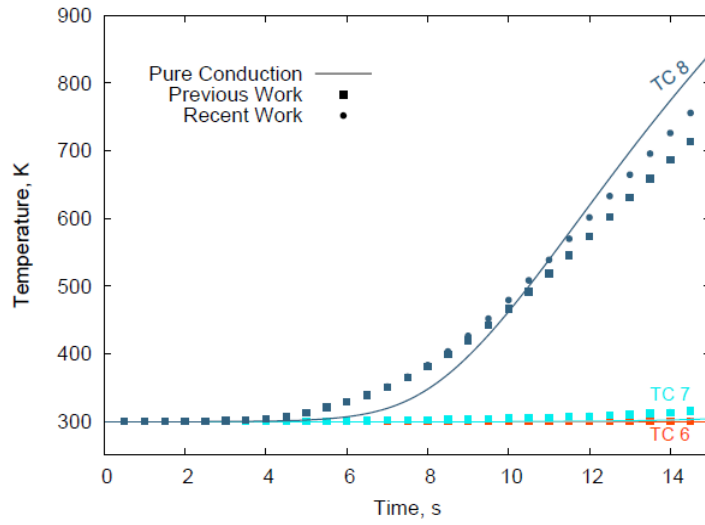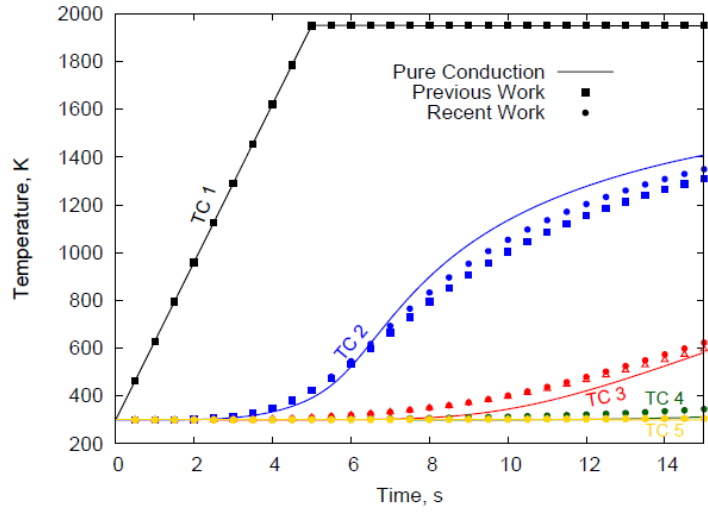
Figure 5.14 IsoQ simulation, internal temperature measurements.

Figure 5.15 shows the tempreature difference between the effictive thermal conductivity model and the coupled model using current conductivities and previous conductivities for the IsoQ case.

It is noted that the tempreature difference was reduced in general with the current thermal conductivities, espicially for the first thermocouples where the tempreature is high.
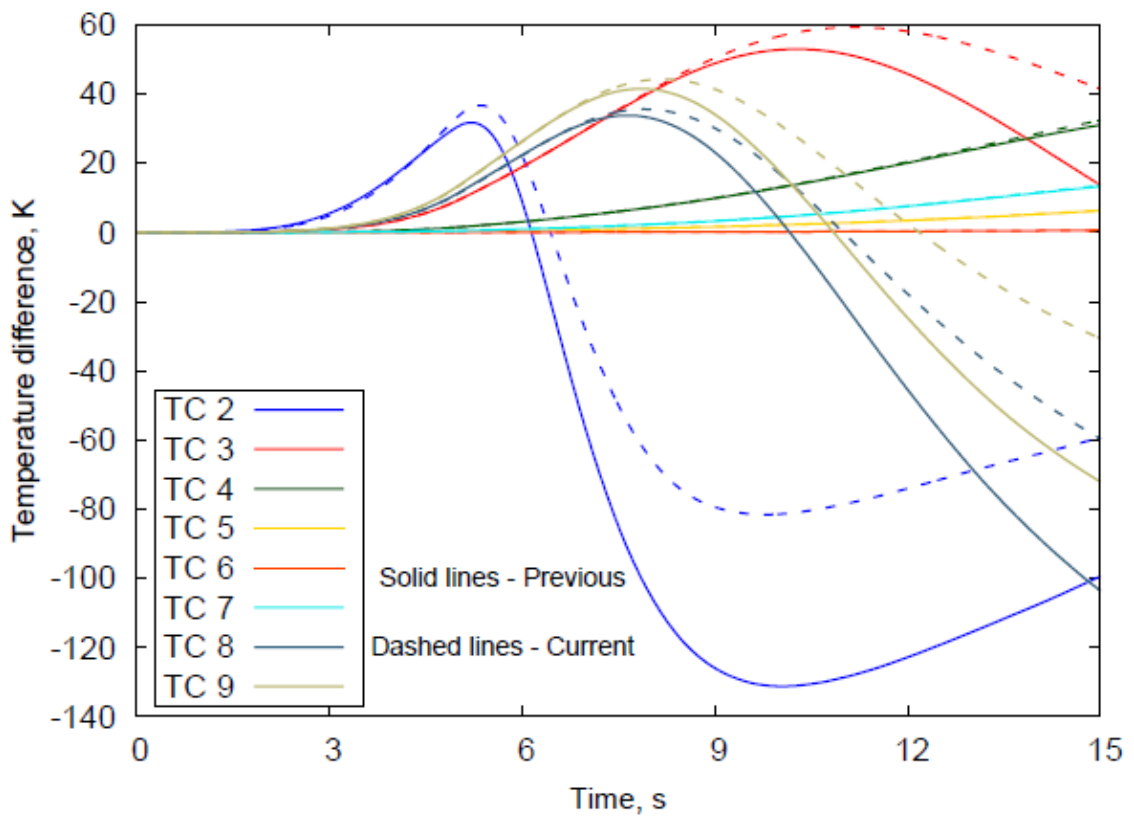
Figure 5.15 IsoQ simulation, Temperature difference between pure conduction and the coupled approach using current conductivities, and Marschall et al. [59] previously published conductivities.

Chapter 6

6.1 summary

Heat transfer through fibrous materials involves conduction as well as internal radiation. Previously, the effect of internal radiation was accounted by using an effective thermal conductivity model. However, this model does not permit detailed radiative studies which are required for shock layer radiation.

A coupled model based on the radiative transfer equation was proposed and compared with the previous model. There are two main requirements for the coupled conduction-radiation model: a proper thermal conductivity, and a radiative transfer equation solver.

There are multiple methods that approximate the radiative transfer equation. However, only two of them were considered in this work and compared against analytical and Monte Carlo solutions. Both solvers were verified and tested for multiple cases, and it was concluded that the P1 approximation serves the purpose of this research better for one dimensional geometries. It does not consume too much computational time and provides comparable results to the finite volume method.

To run coupled analysis a proper solid/gas thermal conductivity should be used, to avoid accounting for radiation multiple times.

A novel approach was proposed in this work that does not require iterative procedures nor does it assume any functional form for the temperature dependent thermal conductivity. A wide range of temperature dependent thermal conductivities were obtained using the P1 approximation as well as the FVM method.

The obtained values were verified using multiple test cases and compared against previously published results. It was noted that the new thermal conductivities produced better results and smaller differences when a similar domain was used.

The proposed method gives the capability to obtain the solid/gas thermal conductivities for different materials, and for any required temperature range. Which enables as a consequence, the analysis of spectral radiative studies needed to optimize thermal protection systems (TPS) materials.

6.2 Future studies

This work provided coupled analysis for a one dimensional domain. However, it is of interest to check the fidelity of the proposed method for multidimensional domains since many materials exhibit anisotropic behavior. It is important to study the behavior of the solver for multidimensional domains since optical thickness as well as radiative properties do affect the solution.

 Only isotropic scattering was considered for this work, however; fibrous materials exhibit anisotropic scattering behavior. It is important to study the effect of scattering on the results as well as the time required to obtain the solution.

Only LI-900 fibrous material was used for this work. Different materials exhibit different behaviors and it is important to test the proposed method for a variety of materials.

It was noted from the comparison cases against the Monte Carlo results that the spherical harmonics method produced larger error compared to one dimensional cases. It is important to test the applicability of the radiative heat transfer solver for multidimensional geometries.

Bibliography

[1] Siegel, R., Howell, J., "Thermal Radiation Heat Transfer", NASA Lewis Research Center, Clevland, OH, Volume 3.

[2] HOTTEL, H. C.: Radiant-Heat Transmission. Heat Transmission. Third ed., William H.McAdams, McGraw-Hill Book Co., Inc., 1954.

[3] John Balboni. URL https://www.nasa.gov/centers/ames/research/2007/faq-shuttlereentry.html

[4] Uyanna, O., and Najafi, H., "Thermal protection systems for space vehicles: A review on technology development, current challenges and future prospects", Acta Astronautica ,Volume 176, 2020, Pages 341-356.

https://doi.org/10.1016/j.actaastro.2020.06.047

[5] Niehaus, W., "heat shield concepts and materials for reentry", Defense Documentation Center for Scientific and Technical Documentation, Alexandria, Virginia., July, 1963

[6] Paul, D., Clay, C., Harber, B., Croop, H., Glass, D., and Scotti, D., "Extreme environment structures", Structures Technology for Future Aerospace Systems, AIAA., 2000.

https://doi.org/10.2514/5.9781600866593.0145.0199

[7] Rivers, H., and Glass, D., "Advances in hot structures development", Thermal Protection Systems and Hot Structures Proceedings of the 5th European Workshop, Europeans Space Agency, 2006.

[8] Launius, R., and Jenkins, D., "Coming Home: Reentry and Recovery from Space", NASA, Washington DC, 2012.

[9] CARY JR., A., and HEFNER, J., "Film-Cooling Effectiveness and Skin Friction in Hypersonic Turbulent Flow", AIAA., Volume 10, 1971.

https://doi.org/10.2514/3.50348

[10] Dellimore, K., Marshall, A., and Cadou, C., "Influence of Compressibility on Film-Cooling Performance", AIAA., Volume 24, 2010.

https://doi.org/10.2514/1.45092

[11] Gerdroodbary, M., "Numerical analysis on cooling performance of counterflowing jet over aerodisked blunt body", shock waves, 2014.

DOI: 10.1007/s00193-014-0517-4

[12] Sriram, R., and Jagadeesh, G., "Film cooling at hypersonic Mach numbers using forward facing array of micro-jets", International Journal of Heat and Mass Transfer, Volume 52, 2009, Pages 3654-3664.

https://doi.org/10.1016/j.ijheatmasstransfer.2009.02.035

[13] Warren, C., "An experimental investigation of the effect of ejecting a coolant gas at the nose of a bluff body", Journal of Fluid Mechanics , Volume 8 , Issue 3 , July 1960 , pp. 400 – 417.

DOI: https://doi.org/10.1017/S0022112060000694

[14] Amar, A., "Modeling of One-Dimensional Ablation with Porous Flow Using Finite Control Volume Procedure", Masters theses, North Carolina state university, 2016.

URL http://www.lib.ncsu.edu/resolver/1840.16/2847

[15] Modest, M. F., "Radiative Heat Transfer", Third Edition, 2013

https://doi.org/10.1016/C2010-0-65874-3

[16] Johnston, C., Brandis, A., "Features of Afterbody Radiative Heating for Earth Entry", Journal of Spacecraft and Rockets, 2014.

doi: 10.2514/1.A33084

[17] Wright, M., Milos, F., and Tran, P., "Afterbody Aeroheating Flight Data for Planetary Probe Thermal Protection System Design," Journal of Spacecraft and Rockets, Vol. 43, No. 5, 2006, pp. 929–943. doi:10.2514/1.17703

[18] Savajano, R., Joshi, O., and Leyland, P., "Aerothermal Analysis of the Phoebus Capsule with Radiative Heating on the Back Body," AIAA Paper 2012-1281, 2012.

[19] Shang, J. S., and Surzhikov, S. T., "Simulating Stardust Earth Reentry with Radiation Heat Transfer," Journal of Spacecraft and Rockets, Vol. 48, No. 3, 2011, pp. 385–396.

doi:10.2514/1.52029

[20] Otsu, H., Suzuki, K., Fujita, K., and Abe, T., "Assessment of Forebody and Backbody Radiative Heating Rate of Hypervelocity Reentry Capsule," Inst. of Space and Astronautical Science, Rept. SP-17, 2003.

[21] Liu,Y., Prabhu, D., Sounders, D.,Vinokur, M., and Dateo, C., "Comparison of Tangent Slab Approximation and Full Angular Integration in Computing Radiative Heating for the CEV Heatshield,"NASA TN/EGCAP- 06-124, 2006.

[22] Hartung, L., and Hassan, H., "Radiation transport around axisymmetric blunt body vehicles using a modified differential approximation" journal of Thermophysics and Heat Transfer, Volume 7, 1993.

https://doi.org/10.2514/3.410

[23] "Arc Test of IsoQ Model,"NASA Photograph, 2014,

https://www.nasa.gov/centers/amesthermophysics-facilities/arc-test-of-isoq-model.

[24] Chandrasekhar, S., "Radiative Transfer", Dover Publications, 1960, ISBN 9780486605906.

[25] Lee, E.,"The discrete *Sn* approximation to transport theory," Technical Information Series Report LA2595,Lawrence Livermore Laboratory, 1962.

[26] Lathrop, D.: "Use of discrete-ordinate methods for solution of photon transport problems," *Nuclear Science and Engineering,* vol. 24, pp. 381-388, 1966.

[27] Carlson, B., and Lathrop, K., "Transport theory, the method of discrete ordinates " , Computing Methods in Reactor Physics, eds. H. Greenspan, C. N. Kelber, and D. Okrent, Gordon «& Breach, New York, 1968.

[28] Love, T. J,, and R. J. Grosh: "Radiative heat transfer in absorbing, emitting, and scattering media," *ASME Journal of Heat Transfer,* vol. 87, pp. 161-166,1965.

[29] Hsia, H. M., and T. J. Love: "Radiative heat transfer between parallel plates separated by a non-isothermal medium with anisotropic scattering" ASME Journal of Heat Transfer, vol. 89, pp. 197-204, 1967.

[30] Hottel, H. C, A. F. Sarofim, L. B. Evans, and I. A. Vasalos: "Radiative transfer in anisotropically scattering media: Allowance for Fresnel reflection at the *houndmQs"* *ASME Journal of Heat Transfer,* vol. 90, pp. 56-62,1968.

[31] Fiveland, W. A.: "A discrete ordinates method for predicting radiative heat transfer in axisymmetric enclosures," ASME Paper 82-HT-20, 1982.

[32] Fiveland, W. A.: "Discrete ordinates solutions of the radiative transport equation for rectangular enclosures," ASME Journal of Heat Transfer, vol. 106, pp. 699-706, 1984.

[33] Fiveland, W. A.: "Discrete ordinate methods for radiative heat transfer in isotropically and anisotropically scattering media," ASME Journal of Heat Transfer, vol. 109, pp. 809-812,1987.

[34] Fiveland, W. A.: "Three-dimensional radiative heat-transfer solutions by the discrete-ordinates method," Journal of Thermophysics and Heat Transfer, vol. 2, no. 4, pp. 309-316, Oct 1988.

[35] Hyde, D. J., and J. S. Truelove: "The discrete ordinates approximation for multidimensional radiant heat transfer in furnaces," Technical Report VKAEA Report No. AERE-R 8502, Thermodynamics Division, AERE Harwell, Oxfordshire, February 1977.

[36] Truelove, J. S.: "Discrete-ordinate solutions of the radiation transport equation", ASME Journal of Heat Transfer, vol. 109, no. 4, pp. 1048-1051, 1987.

[37] Truelove, J. S.: "Three-dimensional radiation in absorbing-emitting-scattering media using the discrete-ordinates approximation," Journal of Quantitative Spectroscopy and Radiative Transfer, vol. 39, no. l,pp. 27-31, 1988.

[38] Schuster, A., "Radiation Through a Foggy Atmosphere", Astrophysical Journal, Vol. 21, pp. 1-22, 1905.

[39] Schwarzschild, K., "Uber das Gleichgewicht der Sonnenatmospharen", Akademie der Wissenschajten in Goettingen, Nachrichten. MathematischPhysikalische Klasse, Vol. 1, pp. 41-53, 1906

[40] Jeans, H., "The equations of radiative transfer of energy," Monthly Notices of the Royal Astronomical Society, Volume 78, Issue 1, November 1917, Pages 28–36. https://doi.org/10.1093/mnras/78.1.28

[41] Kourganoff, V., "Basic Methods in Transfer Problems" Dover Publications, New York, 1963.

[42] Davison, B., "Neutron Transport Theory", Oxford University Press, London, 1958.

[43] Murray, R. L.: Nuclear Reactor Physics, Prentice Hall, Englewood Cliffs, NJ, 1957.

[44] MacRobert, T. M.: Spherical Harmonics, 3rd ed., Pergamon Press, New York, 1967.

[45] White, "Effects of laser wavelength on ablator testing", 38th Annual Conference on Composites, Materials and Structures, 2014.
 doi:2060/20140011553

[46] Chai, J. C., Patankar, S. V., "Finite volume method for radiation heat transfer", Advances In Numerical Heat Transfer, Volume 2, Chapter 4, 2018.

[47] Bergman, T., DeWitt, D., Lavine, A., and Incropera, F., "Fundamentals of Heat and Mass Transfer" , 8th edition.

[48] Çengel, Y., Ghajar, A., "Heat and mass transfer fundamentals and applications", 8th edition.

[49] Hassanzadeh, P., "An Efficient Computational Method for Thermal Radiation in Participating Media", Masters Theses, University of Waterloo, 2007.

[50] Düzel, Ü., Schroeder, O. M., Zhang, H., and Martin, A., "Numerical Simulation of an Arc Jet Test Section",Journal of Thermophysics andHeat Transfer, 2019.

[51] Raithby, G. D., and Chui, E. H., "A Finite-Volume Method for Predicting a Radiant Heat Transfer in Enclosures With Participating Media" journal of heat transfer, May 1990, 112(2): 415-423 (9 pages).

https://doi.org/10.1115/1.2910394

[52] Bird, R. B., Stewart, W. E., and Lightfoot, E. N., "Transport Phenomena", Second Edition, Wiley, 2014

[53] Davuluri, R. S. C., Fu, R., Tagavi, K. A., and Martin, A., "Numerical investigation on the effect of the spectral radiative heat transfer within an ablative material," 2022 AIAA Scitech Forum, AIAA Paper 2022-1283, San Diego, California, January 2022. DOI: 10.2514/6.2022-1283

[54] Heaslet, M. A., and Warming, R. F., "Radiative Transport and Wall Temperature Slip in Absorbing Planar Medium", International Journal of Heat and Mass Transfer, Vol. 8, 1965, pp.979−994.

https://doi.org/10.1016/0017-9310(65)90083-9

[55] Crosbie, A. L., and Schrenker, R. G., "Radiative Transfer in a Two-Dimensional Rectangular Medium Exposed to Diffuse Radiation", Journal of Quantitative Spectroscopy and Radiative Transfer, Vol. 31, No. 4, 1984, pp.339−372

[56] Yang, J., and Modest, M. F., "Elliptic PDE Formulation of General Three-Dimensional High-Order PN-Approximations for Radiative Transfer", Journal of Quantitative Spectroscopy and Radiative Transfer,1042, pp. 217–227.

[57] - Modest, M. F., and Yang, J., "Elliptic PDE Formulation and Boundary Conditions of the Spherical Harmonics Method of Arbitrary Order for General Three Dimensional Geometries", Journal of Quantitative Spectroscopy and Radiative Transfer, 109, pp.1641–1666.

[58] Ravishankar, M., Mazumder, S., Kumar, A., "Finite Volume Formulation and Solution of the P3 Equations of Radiative Transfer on Unstructured Meshes", *Journal of Heat Transfer*. Feb 2010, 132(2): 023402 (14 pages)

https://doi.org/10.1115/1.4000184

[59] Marschall, J., Maddren, J., and Parks, J., "Internal Radiation Transport and Effective Thermal Conductivity of Fibrous Ceramic Insulation,"35th AIAA Thermophysics Conference, AIAA Paper 2001-2822, Anaheim, California, June 2001.

doi:10.2514/6.2001-2822

[60] https://www.nasa.gov/feature/orion-spacecraft-to-test-new-entry-technique-on-artemis-i-mission

[61] 0zisik, M., and Orlande, H. "Inverse Heat Transfer Fundamentals And Applications", Tayor And Francis, New York, 2000, pp 3-16.

[62] Özişik, M. Huang, C. H.," DIRECT INTEGRATION APPROACH FOR SIMULTANEOUSLY ESTIMATING TEMPERATURE DEPENDENT THERMAL CONDUCTIVITY AND HEAT CAPACITY", Numerical Heat Transfer, Part A: Applications, Volume 20, 1991 - Issue 1

doi:10.1080/10407789108944811

[63] Kim, S., Kim C. M., and Kim Y. K., "Non-iterative estimation of temperature-dependent thermal conductivity without internal measurements", International Journal of Heat and Mass Transfer, Volume 46, Issue 10, 2003,PP 1801-1810,

doi:10.1016/S0017-9310(02)00486-6

[64] Williams, S. D., and Curry, D. M., "Thermal Protection Materials: Thermophysical Property Data", NASA Reference Publication 1289, December 1992.

[65] Davuluri, R. S. C., Fu, R., Tagavi, K. A., and Martin, A., "Fully coupled internal radiative heat transfer for the 3D material response of heat shield,"2021 AIAA Aviation Forum and Exposition, AIAA Paper 2021-3131, Virtual Event, August 2021. DOI: 10.2514/6.2021-3131

Vita

Mohammad Khaleel

https://orcid.org/0000-0003-0375-7298

Education:

- Qatar University, Doha, Qatar   2011-2016
  Bachelor of Science in Mechanical Engineering

Positions held:

- Graduate Research Assistant for Dr. Alexandre Martin, University of Kentucky, Department of Mechanical Engineering   Jan 2021 – Present
- Teaching Assistant, Heat Transfer, University of Kentucky, Department of Mechanical Engineering   Aug 2019 – May 2020

Publications:

- Khaleel, M., Martin, A., "Radiative conductivity estimation using direct approach for fibrous materials" AIAA AVIATION 2022 Forum, June 2022.

Presentations:

- AIAA Dayton Cincinnati Aerospace Science Symposium   March 2020
   Topic: Radiation/Conduction analysis within charring ablators